NASA/CR—2002-211910

Efficient Reformulation of HOTFGM: Heat Conduction With Variable Thermal Conductivity

Yi Zhong and Marek-Jerzy Pindera
University of Virginia, Charlottesville, Virginia

November 2002

The NASA STI Program Office . . . in Profile

Since its founding, NASA has been dedicated to the advancement of aeronautics and space science. The NASA Scientific and Technical Information (STI) Program Office plays a key part in helping NASA maintain this important role.

The NASA STI Program Office is operated by Langley Research Center, the Lead Center for NASA's scientific and technical information. The NASA STI Program Office provides access to the NASA STI Database, the largest collection of aeronautical and space science STI in the world. The Program Office is also NASA's institutional mechanism for disseminating the results of its research and development activities. These results are published by NASA in the NASA STI Report Series, which includes the following report types:

- TECHNICAL PUBLICATION. Reports of completed research or a major significant phase of research that present the results of NASA programs and include extensive data or theoretical analysis. Includes compilations of significant scientific and technical data and information deemed to be of continuing reference value. NASA's counterpart of peer-reviewed formal professional papers but has less stringent limitations on manuscript length and extent of graphic presentations.

- TECHNICAL MEMORANDUM. Scientific and technical findings that are preliminary or of specialized interest, e.g., quick release reports, working papers, and bibliographies that contain minimal annotation. Does not contain extensive analysis.

- CONTRACTOR REPORT. Scientific and technical findings by NASA-sponsored contractors and grantees.

- CONFERENCE PUBLICATION. Collected papers from scientific and technical conferences, symposia, seminars, or other meetings sponsored or cosponsored by NASA.

- SPECIAL PUBLICATION. Scientific, technical, or historical information from NASA programs, projects, and missions, often concerned with subjects having substantial public interest.

- TECHNICAL TRANSLATION. English-language translations of foreign scientific and technical material pertinent to NASA's mission.

Specialized services that complement the STI Program Office's diverse offerings include creating custom thesauri, building customized databases, organizing and publishing research results . . . even providing videos.

For more information about the NASA STI Program Office, see the following:

- Access the NASA STI Program Home Page at ***http://www.sti.nasa.gov***

- E-mail your question via the Internet to help@sti.nasa.gov

- Fax your question to the NASA Access Help Desk at 301–621–0134

- Telephone the NASA Access Help Desk at 301–621–0390

- Write to:
  NASA Access Help Desk
  NASA Center for AeroSpace Information
  7121 Standard Drive
  Hanover, MD 21076

NASA/CR—2002-211910

Efficient Reformulation of HOTFGM: Heat Conduction With Variable Thermal Conductivity

Yi Zhong and Marek-Jerzy Pindera
University of Virginia, Charlottesville, Virginia

Prepared under Grant NAG3–2524

National Aeronautics and
Space Administration

Glenn Research Center

November 2002

Acknowledgments

This research was conducted under funding through the NASA Glenn Grant NAG3–2524. The NASA technical monitor for this project was Dr. Steven M. Arnold whose support and encouragement for the undertaken investigation, the authors gratefully acknowledge.

Available from

NASA Center for Aerospace Information
7121 Standard Drive
Hanover, MD 21076

National Technical Information Service
5285 Port Royal Road
Springfield, VA 22100

Available electronically at http://gltrs.grc.nasa.gov

Efficient Reformulation of HOTFGM: Heat Conduction With Variable Thermal Conductivity

Yi Zhong and Marek-Jerzy Pindera
University of Virginia
Charlottesville, Virginia 22903

Abstract

Functionally graded materials (FGMs) have become one of the major research topics in the mechanics of materials community during the past fifteen years. FGMs are heterogeneous materials, characterized by spatially variable microstructures, and thus spatially variable macroscopic properties, introduced to enhance material or structural performance. The spatially variable material properties make FGMs challenging to analyze. The review of the various techniques employed to analyze the thermomechanical response of FGMs reveals two distinct and fundamentally different computational strategies, called uncoupled macromechanical and coupled micro-macromechanical approaches by some investigators. The uncoupled macromechanical approaches ignore the effect of microstructural gradation by employing specific spatial variations of material properties, which are either assumed or obtained by local homogenization, thereby resulting in erroneous results under certain circumstances. In contrast, the coupled approaches explicitly account for the micro-macrostructural interaction, albeit at a significantly higher computational cost. The higher-order theory for functionally graded materials (HOTFGM) developed by Aboudi et al. (1999) is representative of the coupled approach. However, despite its demonstrated utility in applications where micro-macrostructural coupling effects are important, the theory's full potential is yet to be realized because the original formulation of HOTFGM is computationally intensive. This, in turn, limits the size of problems that can be solved due to the large number of equations required to mimic realistic material microstructures. Therefore, a basis for an efficient reformulation of HOTFGM, referred to as user-friendly formulation, is developed herein, and subsequently employed in the construction of the efficient reformulation using the local/global conductivity matrix approach. In order to extend HOTFGM's range of applicability, spatially variable thermal conductivity capability at the local level is incorporated into the efficient reformulation. Analytical solutions to validate both the user-friendly and efficient reformulations are also developed. Volume discretization sensitivity and validation studies, as well as a practical application of the developed efficient reformulation, are subsequently carried out. The presented results illustrate the accuracy and implementability of both the user-friendly formulation and the efficient reformulation of HOTFGM .

1 Introduction

Functionally graded materials (FGMs) have become one of the major research topics in the mechanics and materials communities during the past fifteen years. FGMs are heterogeneous materials which are composed of two or more phases with different properties, and therefore they belong to

the broad class of materials known as composites. Unlike traditional composites, however, the spatial distribution of phases in FGMs is not statistically homogeneous. As the name suggests, FGMs are materials with macroscopic properties characterized by spatial gradients. This is accomplished by using variable spacings between individual inclusions or by using inclusions with different properties, sizes and shapes. Research results obtained thus far have demonstrated that FGMs have great potential for improving material/structural performance in many engineering applications precisely because of their spatially graded heterogeneous microstructure. In particular, grading or tailoring the internal microstructure of a composite material or structural component enables the designer to integrate both the material and structural aspects into the final design and product. This offers a number of advantages over traditional methods of tailoring composite materials and structural components through the elimination of sharp material discontinuities which often lead to undesirable stress concentrations, thereby degrading the structural component's strength and durability.

The concept of modern man-made FGMs was first proposed in 1984 by material scientists in the Sendai area of Japan as a means of developing thermal protection materials. In particular, this concept was originally conceived for thermal protection of fuselage exterior and engine materials intended for use in high-speed civil transport aircraft under development in the mid 1980's through mid 1990's, and then rapidly spread to other fields including physics, chemistry, agriculture, biology and medicine. After almost twenty years of development, the term FGM is now widely used in various fields to describe this class of materials. Strictly speaking, however, graded materials are not new. They can be found in nature, and they also have been utilized extensively by human beings for many years without being explicitly called FGMs. The examples include graded materials developed long ago, such as case-hardened steel, which are still in common use today, Kaysser and IIschner (1995). Other naturally occurring biological FGMs include bamboo, which has been used for a long time for structural components, corn, barley, etc., Figure 1. Nevertheless, the new and exciting thing about modern FGMs is the realization that the property gradient can be designed at the microstructural level to tailor the material's specific function and performance required by engineering needs.

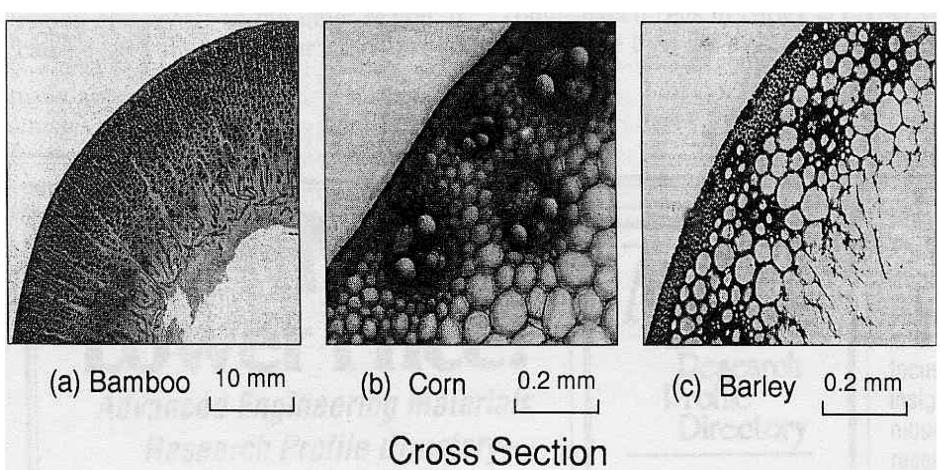

Figure 1. Selected FGMs found in nature. (Source: Amada, 1995).

As stated in the foregoing, FGMs are excellent candidates for applications involving severe thermal gradient environments. Some practical examples of the successful application of the FGM

concept include zirconia coatings deposited on a nickel-chromium alloy substrate by plasma spraying, where the composition profiles of the graded interlayers are carefully optimized to minimize thermally-induced stresses under service loading conditions. By appropriately adjusting the microstructural transition, that is by placing the ceramic-rich part of a functionally graded material in the high temperature environment and the metallic-rich part in the low temperature environment, with a gradual microstructural transition in the direction of the temperature gradient, it is possible to achieve optimum temperature, deformation and stress distributions. An example of a graded thermal barrier coating is given in Figure 2. In this case, the requirements for heat-resistant and oxidation-resistant properties are fulfilled, as well as those for adequate mechanical toughness. In another successful application, Honda Engineering Co. Ltd. developed a functionally graded cemented carbide with improved wear resistance and tool life, owing to a coarse grain size and smaller cobalt content in the surface region than in the core region with a graded interlayer, Ichikawa (2001). Thus the highest hardness was achieved in the surface layer while the toughness increased towards the core region.

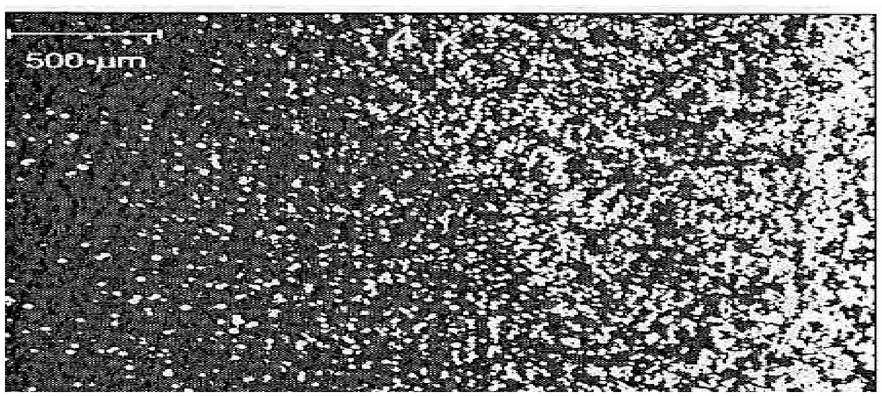

Figure 2. Graded ceramic-metal thermal barrier coating (Source: Dollmeier et al. 1995).

There is no doubt that FGMs offer substantial advantages over traditional composites in the design of structural components which require different types of materials to simultaneously satisfy various requirements such as load bearing capability, surface protection, and perhaps decorative function. In particular, it has been demonstrated that microstructural gradients not only can overcome problems associated with traditional composites by smoothing out property discontinuities, but can also produce unique and desirable functions, such as focusing light in fibers, channeling heat in computer chips, and providing biocompatible implant-tissue transitions in biomedical engineering applications, for instance.

However, there are many challenges that must be overcome in order to make full use of the FGM potential, Ilschner (1997). Materials researchers agree that the FGM manufacturing capabilities and material development are not in a dynamic growth phase comparable to that which occurred during the 1960-1980 period for the then-emerging materials such as plastics. The reason is that with the present state of knowledge, it is very difficult and expensive to fabricate graded materials with various designed functions in large quantities for industrial use. Moreover, at the present time, mature design standards and test methods for FGMs are insufficient or unavailable. Just as importantly, the multiscale approach required in the analysis, design and optimization of FGMs is still not well developed. The present investigation, therefore, was undertaken to address this last point, as will be discussed in more detail later. The literature review of the following section provides the motivation for the undertaken study.

1.1 Literature Review

In this section, a brief overview of the FGM development is given for completeness, followed by a discussion of theoretical modeling methods used to analyze FGMs. The emphasis is put on the latter in view of the focus of this investigation which addresses one aspect of multiscale modeling of FGMs, as discussed in the next section.

With the realization of the important role that FGMs will play in many fields, many researchers have devoted a substantial amount of time and energy in recent years to the broad area of FGMs, ranging from the different fabrication techniques and characterization methods to the development of theoretical models for the response of these materials. The development and exploration of FGMs was initiated in Japan under a national project during the period 1987-1991. The aim of this government-sponsored project was to develop FGMs for future aerospace applications. Following this, similar projects and forums for FGM research and development were initiated in other countries, in particular in Germany, Finland, China, the United States and Russia. Research on functionally graded materials around the world increased rapidly after the First International Symposium devoted solely to these materials, which was held in Sendai, Japan in 1990. The second International Symposium on FGMs was held in San Francisco in 1992, followed by the Third International Symposium held in Lausanne, Switzerland in 1994. These symposia, which were organized by the International Forum on FGMs, are now held every two years on a regular basis with the next one scheduled for the fall of 2002 in Beijing, China.

As a result of the above activities, the overall research and development of FGMs has expanded to many areas. Consequently, many papers on different aspects of FGMs have been published in standard journals, special issues of journals devoted solely to FGMs, conference proceedings, and monographs, cf. Pindera et al. (1994a, 1995a, 1997), Needleman and Suresh (1996), Yamanouchi et al. (1990), Ilschner and Cherradi (1994), Shiota and Miyamoto (1997), and Suresh and Mortensen (1998). Therefore, a comprehensive review of the different research activities is outside the scope of this report. Therefore, in keeping with the investigation's focus, an overview is provided below of the different approaches employed by researchers to model the thermomechanical response of FGMs.

The review of the various techniques employed to analyze the response of FGMs under thermal and mechanical loading reveals two distinct and fundamentally different computational strategies. These have been termed uncoupled and coupled micro-macromechanical approaches by Aboudi et al. (1993). The uncoupled approaches do not explicitly couple the material's heterogeneous microstructure with the structural global analysis. Local effective or macroscopic properties at a given point within the FGM are first obtained through homogenization based on a chosen micromechanics scheme, and subsequently used in a global thermomechanical analysis, Figure 3. The response of an FGM under specified loading at a homogenized material point with equivalent properties is obtained by solving the governing differential equations (partial or ordinary) with variable coefficients which represent the spatially macroscopic material property variation obtained from homogenization. Sometimes, the spatial property variation is represented as piece-wise uniform which is accomplished by discretizing the microstructure into layers or strips with uniform properties that change gradually from layer to layer. Clearly, by employing only effective or homogenized properties in the global FGM analysis, the microstructural details can only affect the FGM in an effective or average way. It is in this sense that the approach is uncoupled.

The key assumption made in the uncoupled approach is that the heterogeneous microstructure of an FGM can be replaced by an equivalent continuum with a set of macroscopic properties that vary with spatial coordinates in a manner commensurate with the material's heterogeneity. The various micromechanical approaches that may be used to calculate homogenized material properties

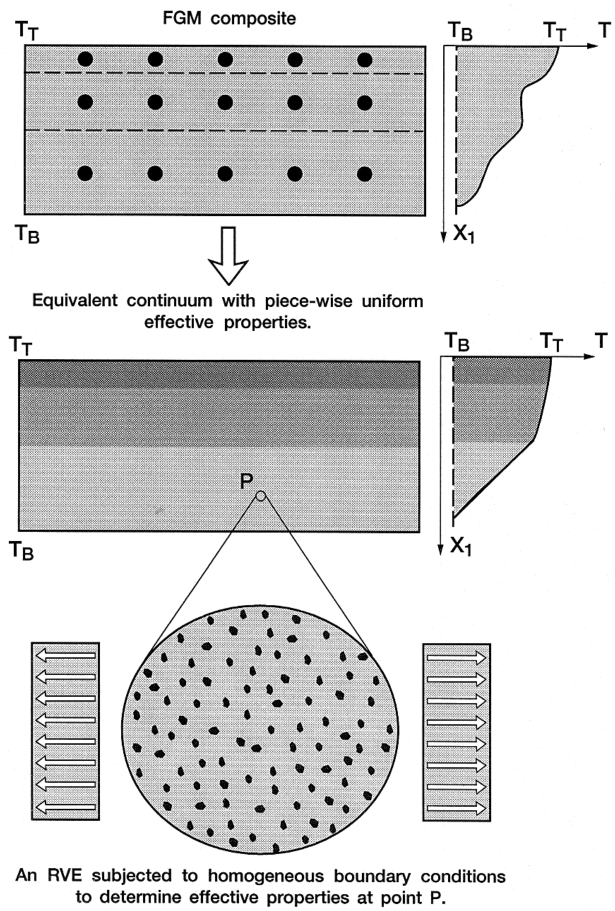

Figure 3. Homogenization-based analysis of FGMs.

include Reuss and Voigt hypotheses, self-consistent schemes, Mori-Tanaka method, concentric cylinder models, and the Generalized Method of Cells, as discussed by Aboudi (1991). Therefore, the use of the uncoupled micro-macromechanical approach in analyzing the response of FGMs is implicitly based on the assumption of the applicability of the representative volume element (RVE) concept. However, the definition of an RVE remains to be established theoretically for materials with spatially variable heterogeneous microstructures. In addition, ignoring the possibility of coupling between local and global effects itself may result in potentially erroneous predictions. This is especially relevant when the thermal and mechanical field variable gradients are relatively large compared with the characteristic dimension of the inclusion phase or the number of inclusions is small, or the dimension of the inclusion phase is large relative to the global dimension of the composite, Aboudi et al. (1993, 1994). Therefore, this type of approach should be used in limited circumstances such as when the size of the inclusion is relatively small compared with the overall size of composite or the number of the inclusions is large, Pindera et al. (1995b).

The alternative to the uncoupled approach is the coupled approach wherein the micro-macrostructural interaction is explicitly taken into account. This implies that the local micromechanics analysis must be combined with the global or structural analysis in a way that connects the two scales directly. One way to do this is to solve the entire problem directly by accounting for the presence of every local heterogeneity. In the presence of many inclusions, the solution of the given boundary-value problem in an exact sense is prohibitive and often impossible, necessitating development of approximate computational strategies.

1.1.1 The uncoupled macrostructural approach

The uncoupled approach is the simpler of the two approaches in the analytical sense since it treats the micro and macrostructural problems separately. As a result, many particular types of problems involving FGM applications have been solved using this approach. One of the most important applications involves thermal barrier coating (TBC) problems. As discussed in the preceding section, internal stresses can be reduced and fracture toughness can be enhanced by appropriate choice of microstructural gradation. For instance, Fukumoto et al. (1994) addressed the influence of coating configuration on cyclic thermal shock fracture behavior of plasma sprayed coatings. An extensive review of the different approaches employed to evaluate temperature and stress fields in TBCs has been recently provided by Noda (1999). In the presence of inelastic effects, the approaches range from one-dimensional finite-difference analyses, Kokini and Choules (1995), to two-dimensional finite-element analyses based on layer-wise discretization of the coating microstructure with piece-wise uniform properties calculated using simple rule-of-mixtures or Mori-Tanaka estimates, such as those by Jian et al. (1995) or Delfosse et al. (1997). Elastic analyses often use continuously varying properties of particular functional form, thereby facilitating either closed-form analytical solutions, or numerical solutions based on the Green's function approach, such as those presented by Nomura and Sheahen (1997) and Sutradhar et al. (2002).

Another important application of FGMs involves joining structural components made of dissimilar materials using graded transition regions to reduce the large interlaminar stresses that arise at the free edge due to the material property mismatch. Analyses of these problems have been conducted by Drake et al. (1993) and Williamson et al. (1993) using the finite-element approach to study the effect of material gradation on the free-edge peel stresses in layered cylinders with gradual material variation achieved by using slightly different material properties in each cylindrical layer. Plasticity was demonstrated to be an important factor in influencing the free-edge stress fields. Suresh et al. (1994) demonstrated similar effects in analyzing the response of elastoplastic biomaterial strips subjected to cyclic thermal loading.

Fracture analysis is also an important area of FGMs. In a sequence of papers, Erdogen and coworkers extended the elasticity techniques for crack-analysis problems of inhomogeneous materials to functionally graded materials, Delale and Erdogan (1983), Erdogan (1985), Erdogan et al. (1991). The focus of these studies were the different failure modes that occur in graded TBCs which are initiated by free-edge cracks, and cracks parallel or perpendicular to the coating surface, as discussed by Kokini et al. (1996) or Kawasaki and Watanabe (1997). These were subsequently analyzed by Erdogan (1995), Erdogan and Wu (1996), Lee and Erdogan (1998), and most recently by Jin and Paulino (2001).

Other applications of FGMs include the important problem of identifying optimum microstructural designs which produce the best temperature and stress distributions under given loading conditions. Various analytical solutions have been developed for specific boundary-value problems (typically involving axisymmetric fields and out-of-plane shearing) which can be incorporated into optimization algorithms for design purposes. These analytical solutions are also useful as benchmark solutions for the validation of finite-element, finite-difference or boundary-element techniques. For instance, Horgan and Chan (1999) developed elastic solutions for problems involving pressurized hollow cylinders, rotating disks, and bars under torsion with continuously graded isotropic constituents. In order to enable fiber-matrix interface/interphase design and optimization in metal matrix composites, Pindera et al. (1994b) extended the previously-developed thermoplastic solution to the problem of an arbitrary layered concentric cylinder under combined thermomechanical axisymmetric loading, Pindera et al. (1993), by incorporating the capability to treat the interfacial layers as two-phase composite materials. The results provided insight into designing/engineering

homogenized and functionally graded interfaces in advanced metal-matrix composites with the objective of generating preferred fabrication-induced residual stress distributions. Salzar and Barton (1994) subsequently incorporated this solution strategy into a commercial optimization code and demonstrated the efficiency with which optimum interfacial architectures could be identified.

1.1.2 The coupled micro-macrostructural approach

The coupled micro-macromechanical approach circumvents the limitations of the standard uncoupled approach in FGM applications by explicitly coupling the local (microstructural) and global (macrostructural) effects. The coupled analysis can be carried out using the finite-element technique. However, this can be prohibitively expensive due to the refined volume discretization required for convergence when dealing with even simple FGM microstructures. For this reason, alternative approximate computational techniques are needed which are sufficiently accurate to compute the micro-macrostructural interaction without requiring excessively large storge.

The representative of such a coupled micro-macromechanical approach is the higher-order theory for functionally graded materials (HOTFGM) developed by Aboudi and co-workers in a sequence of papers and reports originating in 1993, Aboudi et al. (1993). Summaries of the different stages of the higher-order theory have been provided by Pindera et al. (1995c, 1998), and most recently by Aboudi et al. (1999). The theoretical framework is based on volumetric averaging of the various field quantities, satisfaction of the field equations in a volumetric sense, and imposition in an average sense of boundary and interfacial conditions between the subvolumes used to characterize the composite's functionally graded microstructure. The theory has been validated through comparison with the results obtained from finite-element analysis, Pindera and Dunn (1997), and subsequently applied to the following technologically important problems:

- Investigation of the effect of microstructure on thermal and stress fields in MMC plates and cylinders
- Investigation of the use of functionally graded architectures in reducing edge effects in MMC plates
- Optimization of functionally graded microstructures in MMC plates and cylinders
- Development of guidelines for the design of special coatings in exhaust nozzle applications
- Investigation of the microstructural effects in functionally graded TBCs

The results obtained so far have demonstrated that this theory is an accurate and easily implementable tool in the analysis and design of FGMs. Furthermore, comparison of the results obtained from the standard micromechanics approach with those of HOTFGM has demonstrated the need for a theory like HOTFGM, which explicitly couples the micro (local) and macro (global) effects within a unified analysis.

The recent developments of HOTFGM include extension to cylindrical coordinates to enable analysis, design, and optimization of structural components found in aircraft engine applications, Pindera and Aboudi (2000).

1.2 Objectives of the Investigation and Outline of the Report

Despite the demonstrated utility of the higher-order theory in applications where the micro-macrostructural coupling effects are important, the theory's full potential has not yet been attained.

This is because the theory as originally formulated is computationally intensive. This, in turn, limits the types of problems that can be solved due to the large number of equations required to mimic realistic material microstructures. Therefore, the objective of this investigation was to construct a basis for an efficient reformulation of the higher-order theory, and subsequently implement it in order to reduce the number of equations required in the solution of a given thermal boundary-value problem. The basis for the efficient reformulation is the demonstration that the same results are obtained when the volume discretization used in the original version is simplified by eliminating the need to differentiate between generic cells and subcells. This is called a user-friendly formulation which, in turn, provides the basis for an efficient reformulation based on the local/global conductivity matrix approach. The efficient reformulation admits spatially variable thermal conductivity within individual subcells, thereby making it possible to treat microstructures with two fundamentally different length scales.

The theoretical framework of the original two-dimensional formulation of HOTFGM, limited to thermal boundary-value problems, is briefly described in the first part of Section 2, with the second part devoted to the development of the user-friendly formulation. Based on the demonstrated feasibility of the simplified user-friendly formulation, an efficient reformulation of HOTFGM with variable thermal conductivity is developed in Section 3 using the local/global conductivity matrix approach, which is an extension of the local/global stiffness matrix approach described by Pindera (1991) in the context of purely mechanical boundary-value problems. Analytical solutions used to validate both the user-friendly and efficient reformulations are developed in Section 4. Volume discretization sensitivity and validation studies, as well as a practical application of the developed efficient reformulation, are provided in Section 5. Section 6 summarizes the present accomplishments and discusses future desirable extensions of the developed computational capability.

2 Higher-Order Theory: Thermal Problem

2.1 Outline of the Original Formulation

The original formulation of the two-directional higher-order theory for functionally graded materials (HOTFGM–2D) was outlined by Aboudi et al. (1996). The basic idea was to develop a two-dimensional framework for the response of composites which are functionally graded in two directions, accounting for micro-macrostructural coupling effects. As indicated in Figure 4, the heterogeneous composite model has finite length L and width H in the $x_2 - x_3$ plane and extends to infinity in the x_1 direction. The thermal loading applied on the boundary can be specified in terms of temperature or heat flux distribution. The microstructure of the heterogeneous composite is discretized into N_q and N_r generic cells (q, r) in the intervals $0 \leqq x_2 \leqq H$, $0 \leqq x_3 \leqq L$ in the $x_2 - x_3$ plane. The indices q and r represent the location of the generic cell in the $x_2 - x_3$ plane and they can vary from $q = 1, 2...$ to N_q and $r = 1, 2, ...$ to N_r. Each generic cell is further discretized into four subcells denoted by the indices $(\beta\gamma)$, Figure 4, where the range of each index β, γ is from 1 to 2. These indices indicate the relative position of a given subcell within the generic cell. The dimension of the generic cell along the x_1 direction is infinite whereas the dimensions along the x_2 and x_3 axes, $h_1^{(q)}, h_2^{(q)}$ and $l_1^{(r)}, l_2^{(r)}$, respectively, can vary from cell to cell such that

$$H = \sum_{q=1}^{N_q}(h_1^{(q)} + h_2^{(q)}) \ , \ L = \sum_{r=1}^{N_r}(l_1^{(r)} + l_2^{(r)})$$

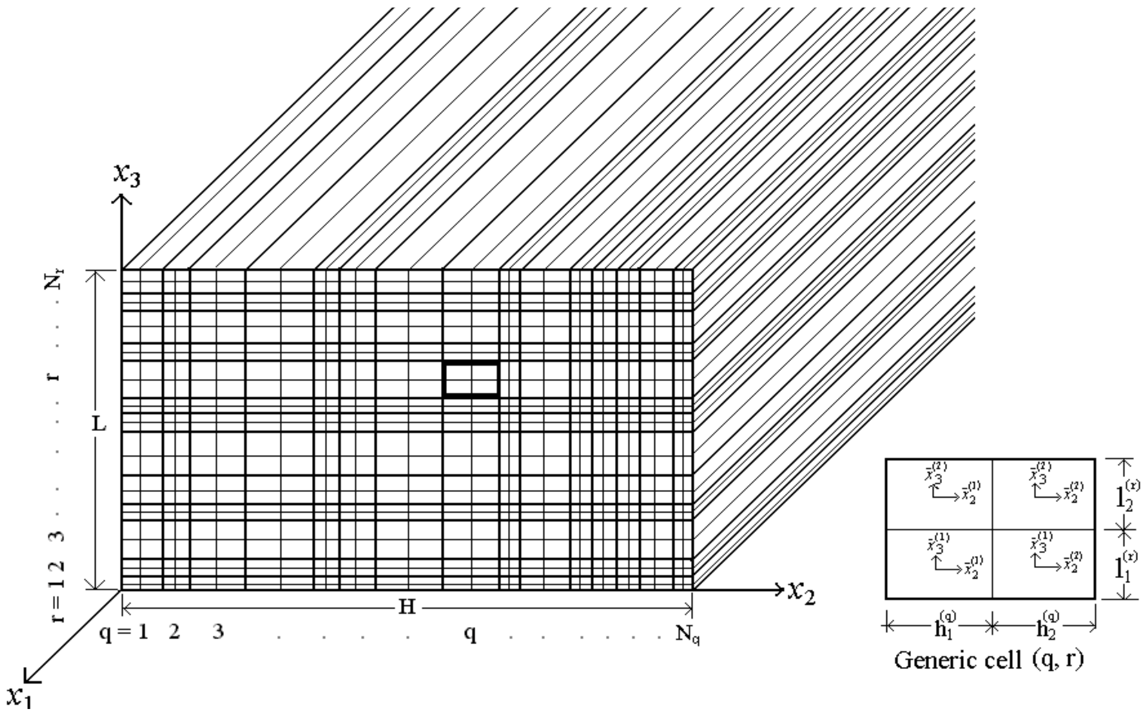

Figure 4. Schematic of the HOTFGM analysis geometry.

An approximate solution for the temperature field under steady-state thermal loading is constructed on the basis of volumetric averaging of the heat conduction equation, together with the imposition of boundary and continuity conditions in an average sense between the subvolumes used to characterize the material's microstructure. The solution to the heat equation is accomplished by approximating the temperature field in each subcell of a generic cell using a quadratic expansion in the local coordinates $\bar{x}_2^{(\beta)}, \bar{x}_3^{(\gamma)}$ centered at subcell's midpoint. The higher-order terms in the temperature field expansion account for the local effects caused by the thermal field gradients, the microstructure of the composite and the finite dimensions in the functionally graded directions, in contrast with the linear expansion used in constructing the micromechanics model for periodic multiphase materials called the Generalized Method of Cells (Paley and Aboudi, 1992). The higher-order theory is an extension of this micromechanics model to materials without periodic microstructures, and employs similar volume discretization and related notation.

The unknown coefficients associated with each term in the temperature field expansion are obtained by constructing a system of equations that satisfies the requirements of a standard boundary-value problem for the given field variable approximations. That is, the zeroth, first, and second moments of the heat conduction equation are satisfied in a volumetric sense. The thermal and heat flux interfacial continuity conditions within a given cell, as well as between a given cell and adjacent cells, are imposed in an average sense together with the applied boundary conditions.

The following two subsections outline the thermal problem formulation and its solution based on the volume discretization employed in the original higher-order theory in order to prepare the stage for a generic cell-free, user-friendly formulation outlined in the second part of this section. A detailed exposition was provided by Aboudi et al. (1999).

2.1.1 Thermal analysis

Heat conduction equation Assume that the functionally graded material model is subjected to steady-state temperature or heat flux distribution on its bounding surfaces in the $x_2 - x_3$ plane.

Under steady-state heat conduction, the heat flux field in the material occupying subcell $(\beta\gamma)$ of the (q,r)th generic cell, in the region $\left|\bar{x}_2^{(\beta)}\right| \leq \frac{1}{2}h_\beta^{(q)}, \left|\bar{x}_3^{(\gamma)}\right| \leq \frac{1}{2}l_\gamma^{(r)}$, must satisfy:

$$\frac{\partial q_2^{(\beta\gamma)}}{\partial \bar{x}_2^{(\beta)}} + \frac{\partial q_3^{(\beta\gamma)}}{\partial \bar{x}_3^{(\gamma)}} = 0 \tag{1}$$

The components $q_i^{(\beta\gamma)}$ of the heat flux vector in this subcell are obtained from the Fourier's heat conduction law for anisotropic materials,

$$q_i^{(\beta\gamma)} = -k_{ij}^{(\beta\gamma)} \frac{\partial T^{(\beta\gamma)}}{\partial \bar{x}_i^{(\cdot)}}, \qquad (i,j = 2,3; \text{no sum}) \tag{2}$$

where $T^{(\beta\gamma)}$ is the temperature distribution in the subcell $(\beta\gamma)$ of the (q,r)th generic cell measured with respect to a reference temperature, and $k_{ij}^{(\beta\gamma)}$ are the coefficients of thermal conductivity of the material in the subcell $(\beta\gamma)$, with $k_{ij}^{(\beta\gamma)} = k_i^{(\beta\gamma)}\delta_{ij}$ (no sum on i) for orthotropic materials. No sum is implied by the repeated Greek letters in the above and henceforth.

The solution to the heat conduction equation in each subcell of every generic cell is obtained in conjuction with satisfaction of the continuity and boundary conditions in the manner described next.

Heat flux continuity conditions The continuity of the heat flux vector $\mathbf{q}^{(\beta\gamma)}$ at the interfaces separating adjacent subcells within the generic cell (q,r) is fulfilled by imposing the integral conditions

$$\int_{-l_\gamma^{(r)}/2}^{l_\gamma^{(r)}/2} q_2^{(1\gamma)} \,|_{\bar{x}_2^{(1)}=h_1^{(q)}/2}^{(q,r)} \, d\bar{x}_3^{(\gamma)} = \int_{-l_\gamma^{(r)}/2}^{l_\gamma^{(r)}/2} q_2^{(2\gamma)} \,|_{\bar{x}_2^{(2)}=-h_2^{(q)}/2}^{(q,r)} \, d\bar{x}_3^{(\gamma)} \tag{3}$$

$$\int_{-h_\beta^{(q)}/2}^{h_\beta^{(q)}/2} q_3^{(\beta 1)} \,|_{\bar{x}_3^{(1)}=l_1^{(r)}/2}^{(q,r)} \, d\bar{x}_2^{(\beta)} = \int_{-h_\beta^{(q)}/2}^{h_\beta^{(q)}/2} q_3^{(\beta 2)} \,|_{\bar{x}_3^{(2)}=-l_2^{(r)}/2}^{(q,r)} \, d\bar{x}_2^{(\beta)} \tag{4}$$

In addition to the above surface-averaged continuity conditions within the (q,r)th generic cell, the heat flux continuity conditions at the interfaces between adjacent cells are given by

$$\int_{-l_\gamma^{(r)}/2}^{l_\gamma^{(r)}/2} q_2^{(2\gamma)} \,|_{\bar{x}_2^{(2)}=h_2^{(q)}/2}^{(q,r)} \, d\bar{x}_3^{(\gamma)} = \int_{-l_\gamma^{(r)}/2}^{l_\gamma^{(r)}/2} q_2^{(1\gamma)} \,|_{\bar{x}_2^{(1)}=-h_1^{(q+1)}/2}^{(q+1,r)} \, d\bar{x}_3^{(\gamma)} \tag{5}$$

$$\int_{-h_\beta^{(q)}/2}^{h_\beta^{(q)}/2} q_3^{(\beta 2)} \,|_{\bar{x}_3^{(2)}=l_2^{(r)}/2}^{(q,r)} \, d\bar{x}_2^{(\beta)} = \int_{-h_\beta^{(q)}/2}^{h_\beta^{(q)}/2} q_3^{(\beta 1)} \,|_{\bar{x}_3^{(1)}=-l_1^{(r+1)}/2}^{(q,r+1)} \, d\bar{x}_2^{(\beta)} \tag{6}$$

Thermal continuity conditions The thermal continuity conditions at the interfaces separating adjacent subcells within the generic cell (q,r) are similar to the corresponding heat flux continuity conditions,

$$\int_{-l_\gamma^{(r)}/2}^{l_\gamma^{(r)}/2} T^{(1\gamma)} \,|_{\bar{x}_2^{(1)}=h_1^{(q)}/2}^{(q,r)} \, d\bar{x}_3^{(\gamma)} = \int_{-l_\gamma^{(r)}/2}^{l_\gamma^{(r)}/2} T^{(2\gamma)} \,|_{\bar{x}_2^{(2)}=-h_2^{(q)}/2}^{(q,r)} \, d\bar{x}_3^{(\gamma)} \tag{7}$$

$$\int_{-h_\beta^{(q)}/2}^{h_\beta^{(q)}/2} T^{(\beta 1)} \,|_{\bar{x}_3^{(1)}=l_1^{(r)}/2}^{(q,r)} \, d\bar{x}_2^{(\beta)} = \int_{-h_\beta^{(q)}/2}^{h_\beta^{(q)}/2} T^{(\beta 2)} \,|_{\bar{x}_3^{(2)}=-l_2^{(r)}/2}^{(q,r)} \, d\bar{x}_2^{(\beta)} \tag{8}$$

Similarly, the thermal continuity conditions at the interfaces between neighboring cells are given by

$$\int_{-l_\gamma^{(r)}/2}^{l_\gamma^{(r)}/2} T^{(2\gamma)} \Big|_{\bar{x}_2^{(2)}=h_2^{(q)}/2}^{(q,r)} d\bar{x}_3^{(\gamma)} = \int_{-l_\gamma^{(r)}/2}^{l_\gamma^{(r)}/2} T^{(1\gamma)} \Big|_{\bar{x}_2^{(1)}=-h_1^{(q+1)}/2}^{(q+1,r)} d\bar{x}_3^{(\gamma)} \tag{9}$$

$$\int_{-h_\beta^{(q)}/2}^{h_\beta^{(q)}/2} T^{(\beta 2)} \Big|_{\bar{x}_3^{(2)}=l_2^{(r)}/2}^{(q,r)} d\bar{x}_2^{(\beta)} = \int_{-h_\beta^{(q)}/2}^{h_\beta^{(q)}/2} T^{(\beta 1)} \Big|_{\bar{x}_3^{(1)}=-l_1^{(r+1)}/2}^{(q,r+1)} d\bar{x}_2^{(\beta)} \tag{10}$$

Boundary conditions The solution for the temperature field must satisfy the boundary conditions at top and bottom, left and right surfaces of the graded material, i.e., on the external surfaces of the boundary cells $q = 1, N_q$; and $r = 1, N_r$. When $q = 1$ and $q = N_q$, the temperature in the cells $(1, r)$ and (N_q, r) at the $x_2 = 0$ and $x_2 = H$ (i.e., left and right) surfaces, respectively, must equal the applied temperature. As in the case of the interfacial continuity conditions, these boundary conditions are imposed in an average sense,

$$\int_{-l_\gamma^{(r)}/2}^{l_\gamma^{(r)}/2} T^{(1\gamma)} \Big|_{\bar{x}_2^{(1)}=-\frac{1}{2}h_1^{(1)}}^{(1,r)} d\bar{x}_3^{(\gamma)} = \int_{-l_\gamma^{(r)}/2}^{l_\gamma^{(r)}/2} T_{left}^{(\gamma)} \, d\bar{x}_3^{(\gamma)} \tag{11}$$

$$\int_{-l_\gamma^{(r)}/2}^{l_\gamma^{(r)}/2} T^{(2\gamma)} \Big|_{\bar{x}_2^{(2)}=+\frac{1}{2}h_2^{(N_q)}}^{(N_q,r)} d\bar{x}_3^{(\gamma)} = \int_{-l_\gamma^{(r)}/2}^{l_\gamma^{(r)}/2} T_{right}^{(\gamma)} \, d\bar{x}_3^{(\gamma)} \tag{12}$$

where $r = 1, \ldots\ldots, N_r$.

Similarly, when $r = 1$ and $r = N_r$, the temperature in the cell $(q, 1)$ and (q, N_r) at the $x_3 = 0$ and $x_3 = L$ (top and bottom) surfaces, respectively, must equal the applied temperature,

$$\int_{-h_\beta^{(q)}/2}^{h_\beta^{(q)}/2} T^{(\beta 1)} \Big|_{\bar{x}_3^{(1)}=-\frac{1}{2}l_1^{(1)}}^{(q,1)} d\bar{x}_2^{(\beta)} = \int_{-h_\beta^{(q)}/2}^{h_\beta^{(q)}/2} T_{bot}^{(\gamma)} \, d\bar{x}_2^{(\beta)} \tag{13}$$

$$\int_{-h_\beta^{(q)}/2}^{h_\beta^{(q)}/2} T^{(\beta 2)} \Big|_{\bar{x}_3^{(2)}=+\frac{1}{2}l_2^{(Nr)}}^{(q,N_r)} d\bar{x}_2^{(\beta)} = \int_{-h_\beta^{(q)}/2}^{h_\beta^{(q)}/2} T_{top}^{(\gamma)} \, d\bar{x}_2^{(\beta)} \tag{14}$$

where $q = 1, \ldots\ldots, N_q$.

Alternatively, we can also apply mixed-boundary conditions involving temperature and heat flux on different portions of the boundary.

2.1.2 Solution of the thermal problem

The temperature distribution in the subcell $(\beta\gamma)$ of the (q, r)th generic cell, measured with respect to a reference temperature T$_{ref}$, is denoted by T$^{(\beta\gamma)}$. The temperature field is approximated by a second-order expansion in the local coordinates $\bar{x}_2^{(\beta)}, \bar{x}_3^{(\gamma)}$as follows (omitting the indices (q, r) for notational simplicity):

$$T^{(\beta\gamma)} = T_{(00)}^{(\beta\gamma)} + \bar{x}_2^{(\beta)} T_{(10)}^{(\beta\gamma)} + \bar{x}_3^{(\gamma)} T_{(01)}^{(\beta\gamma)} + \frac{1}{2}(3\bar{x}_2^{(\beta)^2} - \frac{h_\beta^{(q)^2}}{4}) T_{(20)}^{(\beta\gamma)} + \frac{1}{2}(3\bar{x}_3^{(\gamma)^2} - \frac{l_\gamma^{(r)^2}}{4}) T_{(02)}^{(\beta\gamma)} \tag{15}$$

In the two-directional version of HOTFGM, the temperature field varies only in the $x_2 - x_3$ plane, so the temperature field expansion terms in the x_1 direction are not included. In the above temperature

field approximation, we can see clearly that there are five unknowns, where $T_{(00)}^{(\beta\gamma)}$ is the volume-averaged temperature within the subcell, and $\mathrm{T}_{(mn)}^{(\beta\gamma)}$ ($m, n = 0, 1, 2$ with $m+n \leq 2$) are higher-order terms which are determined from the conditions outlined previously. The reason for the absence of the product terms $x_i^{(.)} x_j^{(.)}$ ($i \neq j$) is due to the averaging procedure employed in the higher-order theory.

In summary, in each generic cell there are four subcells and in every subcell the five unknown coefficients,

$$[T_{(00)}, T_{(10)}, T_{(01)}, T_{(20)}, T_{(02)}]^{(\beta\gamma)}$$

describe the temperature field. Therefore, there are altogether $20N_qN_r$ unknown quantities which must be determined for a composite with N_q rows and N_r columns of cells containing arbitrarily specified materials within their subcells. These unknown coefficients are determined by first satisfying the heat conduction equation, as well as the first and second moment of this equation in each subcell in a volumetric sense. Then the temperature and heat flux continuity conditions are applied in an average sense at the interfaces separating adjacent subcells as well as adjacent cells. Finally, the boundary conditions are imposed in an average sense. Following this procedure, we obtain $20N_qN_r$ equations for the $20N_qN_r$ unknown coefficients in the temperature field expansion as summarized below.

2.1.3 Heat conduction equation

In the course of satisfying the steady-state heat equation in a volumetric sense, the heat flux quantities given below are defined for convenience

$$Q_{i(m,n)}^{(\beta\gamma)} = \frac{1}{A_{(\beta\gamma)}^{(qr)}} \int_{-h_{(\beta)}^{(q)}/2}^{+h_{(\beta)}^{(q)}/2} \int_{-l_{(\gamma)}^{(r)}/2}^{+l_{(\gamma)}^{(r)}/2} (\bar{x}_2^{(\beta)})^m (\bar{x}_3^{(\gamma)})^n q_i^{(\beta\gamma)} d\bar{x}_2^{(\beta)} d\bar{x}_3^{(\gamma)} \tag{16}$$

where $m, n = 0, 1$, or 2 with $m+n \leq 2$, and $A_{(\beta\gamma)}^{(qr)} = h_\beta^{(q)} l_\gamma^{(r)}$ is the cross-sectional area of the subcell $(\beta\gamma)$ in the (q, r)th generic cell. For example, when $m = n = 0$, $Q_{i(00)}^{(\beta\gamma)}$ is the volume-averaged value of the heat flux component $q_i^{(\beta\gamma)}$ in the subcell, while for other values of (m, n), higher-order volume integrals of the heat flux components are obtained. These flux quantities can be evaluated explicitly in terms of the coefficients $T_{(mn)}^{(\beta\gamma)}$ by performing the required volume integration using Eqs. (2) and (15) in Eq. (16). This yields the following non-vanishing zeroth-order and first-order heat fluxes expressed in terms of the unknown coefficients in the temperature field expansion.

$$Q_{2(00)}^{(\beta\gamma)} = -k_2^{(\beta\gamma)} T_{(10)}^{(\beta\gamma)} \tag{17}$$

$$Q_{2(10)}^{(\beta\gamma)} = -k_2^{(\beta\gamma)} \frac{h_\beta^{(q)2}}{4} T_{(20)}^{(\beta\gamma)} \tag{18}$$

$$Q_{3(00)}^{(\beta\gamma)} = -k_3^{(\beta\gamma)} T_{(01)}^{(\beta\gamma)} \tag{19}$$

$$Q_{3(01)}^{(\beta\gamma)} = -k_3^{(\beta\gamma)} \frac{l_\gamma^{(r)2}}{4} T_{(02)}^{(\beta\gamma)} \tag{20}$$

Satisfaction of the zeroth, first and second moment of the steady-state heat equation, Eq. (1), in volumetric sense results in the following four relationships among the first-order heat fluxes $Q_{i(m,n)}^{(\beta\gamma)}$

in the different subcells $(\beta\gamma)$ of the $(q,r)th$ generic cell, where $(\beta\gamma)$ assumes all permutations of the integers 1 and 2,

$$[Q_{2(10)}^{(\beta\gamma)}/h_\beta^2 + Q_{3(01)}^{(\beta\gamma)}/l_\gamma^2]^{(q,r)} = 0 \tag{21}$$

Heat flux continuity equations The equations that ensure heat flux continuity at the subcell interfaces, as well as between individual cells, associated with the x_2 and x_3 directions, Eqs. (3)-(6) are given by

$$[-12Q_{2(1,0)}^{(1\gamma)}/h_1 + Q_{2(0,0)}^{(2\gamma)} - 6Q_{2(1,0)}^{(2\gamma)}/h_2]^{(q,r)} - [Q_{2(0,0)}^{(2\gamma)} + 6Q_{2(1,0)}^{(2\gamma)}/h_2]^{(q-1,r)} = 0 \tag{22}$$

$$[-Q_{2(0,0)}^{(1\gamma)} + \frac{1}{2}Q_{2(0,0)}^{(2\gamma)} - 3Q_{2(1,0)}^{(2\gamma)}/h_2]^{(q,r)} + \frac{1}{2}[Q_{2(0,0)}^{(2\gamma)} + 6Q_{2(1,0)}^{(2\gamma)}/h_2]^{(q-1,r)} = 0 \tag{23}$$

$$[-12Q_{3(0,1)}^{(\beta 1)}/l_1 + Q_{3(0,0)}^{(\beta 2)} - 6Q_{3(0,1)}^{(\beta 2)}/l_2]^{(q,r)} - [Q_{3(0,0)}^{(\beta 2)} + 6Q_{3(0,1)}^{(\beta 2)}/l_2]^{(q,r-1)} = 0 \tag{24}$$

$$[-Q_{3(0,0)}^{(\beta 1)} + \frac{1}{2}Q_{3(0,0)}^{(\beta 2)} - 3Q_{3(0,1)}^{(\beta 2)}/l_2]^{(q,r)} + \frac{1}{2}[Q_{3(0,0)}^{(\beta 2)} + 6Q_{3(0,1)}^{(\beta 2)}/l_2]^{(q,r-1)} = 0 \tag{25}$$

Equations (22)-(25) provide eight relations among the zeroth-order and first-order heat fluxes. It is observed that Eqs. (22)-(25) together with Eq. (21) can be expressed in terms of $T_{mn}^{(\beta\gamma)}$ by using Eqs. (17)-(20).

Thermal continuity equations The equations that ensure the continuity of temperature at the interfaces between the subcells, as well as between the neighboring cells in the x_2 and x_3 directions, obtained from Eqs. (7)-(8) and Eqs. (9)-(10), are as follows:

$$[T_{(00)}^{(1\gamma)} + \frac{1}{2}h_1 T_{(10)}^{(1\gamma)} + \frac{1}{4}h_1^2 T_{(20)}^{(1\gamma)}]^{(q,r)} = [T_{(00)}^{(2\gamma)} - \frac{1}{2}h_2 T_{(10)}^{(2\gamma)} + \frac{1}{4}h_2^2 T_{(20)}^{(2\gamma)}]^{(q,r)} \tag{26}$$

$$[T_{(00)}^{(2\gamma)} + \frac{1}{2}h_2 T_{(10)}^{(2\gamma)} + \frac{1}{4}h_2^2 T_{(20)}^{(2\gamma)}]^{(q,r)} = [T_{(00)}^{(1\gamma)} - \frac{1}{2}h_1 T_{(10)}^{(1\gamma)} + \frac{1}{4}h_1^2 T_{(20)}^{(1\gamma)}]^{(q+1,r)} \tag{27}$$

$$[T_{(00)}^{(\beta 1)} + \frac{1}{2}l_1 T_{(01)}^{(\beta 1)} + \frac{1}{4}l_1^2 T_{(02)}^{(\beta 1)}]^{(q,r)} = [T_{(00)}^{(\beta 2)} - \frac{1}{2}l_2 T_{(01)}^{(\beta 2)} + \frac{1}{4}l_2^2 T_{(02)}^{(\beta 2)}]^{(q,r)} \tag{28}$$

$$[T_{(00)}^{(\beta 2)} + \frac{1}{2}l_2 T_{(01)}^{(\beta 2)} + \frac{1}{4}l_2^2 T_{(02)}^{(\beta 2)}]^{(q,r)} = [T_{(00)}^{(\beta 1)} - \frac{1}{2}l_1 T_{(01)}^{(\beta 1)} + \frac{1}{4}l_1^2 T_{(02)}^{(\beta 1)}]^{(q,r+1)} \tag{29}$$

Equations (26)-(29) provide us with the remaining eight relations governing the temperature field within interior generic cells.

Governing equations The heat conduction equation, Eq. (21), together with the heat flux and thermal continuity conditions, Eqs. (22)-(25) and (26)-(29), respectively, form $20N_qN_r$ linear algebraic equations which govern the $20N_qN_r$ microvariables $T_{mn}^{(\beta\gamma)}$ in the four subcells $(\beta\gamma)$ of an interior cell (q,r); $q = 2, ...N_q - 1$, $r = 2, ...N_r - 1$. For the boundary cells $q = 1$, Eq. (21) as well as Eqs. (24)-(29) are still applicable. However, the heat flux continuity conditions between a given cell and the preceding cell given by Eqs. (22) and (23) are not applicable. They are replaced by the applied temperature or heat flux conditions at the left boundary $x_2 = 0$, i.e., Eq. (11), and the condition that the heat flux at the interface between subcell (1γ) and (2γ) of the cell $(1,r)$ is

continuous. For the boundary cells $q = N_q$, the previous equations are applicable except for Eq. (27), which is replaced by the specific temperature applied at the right boundary $x_2 = H$, i.e., Eq. (12). Similar situation holds for the boundary cells $r = 1$ and $r = N_r$.

The governing equations for the interior and boundary cells form a system of $20N_qN_r$ algebraic equations in the unknown coefficients $\mathbf{T}^{(\beta\gamma)}_{(mn)}$. The solution of these equations determines the temperature distribution within the functionally graded composite subjected to the boundary conditions specified by Eqs. (11)-(14). The final form of this system of equations is symbolically represented below:

$$\bar{\mathbf{k}}\mathbf{T}{=}\mathbf{t} \tag{30}$$

where the structural thermal conductivity matrix $\bar{\mathbf{k}}$ contains information on the geometry and thermal conductivities of the individual subcells $(\beta\gamma)$ in the N_qN_r generic cells (q, r). The thermal coefficient vector $\mathbf{T}$ contains the unknown coefficients that describe the temperature fields in each subcell. It is given by

$$\mathbf{T} = [\mathbf{T}^{(11)}_{11,}..................,\mathbf{T}^{(22)}_{N_qN_r}]$$

where

$$\mathbf{T}^{(\beta\gamma)}_{qr} = [T_{(00)}, T_{(10)}, T_{(01)}, T_{(20)}, T_{(02)}]^{(\beta\gamma)}_{(qr)}$$

Finally, the thermal force vector $\mathbf{t}$ contains information on the boundary conditions.

2.2 User-Friendly Formulation of HOTFGM-2D

The motivation for the development of user-friendly thermal formulation of HOTFGM-2D is to ultimately construct a basis for an efficient reformulation using the local/global conductivity matrix approach, which will be outlined in the next section. User-friendly formulation of HOTFGM-2D basically follows the solution technique of the original formulation which was outlined in the preceding section. The major difference between these two formulations is simplification of the equations through the elimination of the generic cell concept which also simplifies the heat flux continuity conditions.

In the user-friendly formulation, therefore, the microstructure of the heterogeneous composite is discretized into $N_\beta N\gamma$ subcells in the intervals $0 \le x_2 \le H$, $0 \le x_3 \le L$, i.e., the $x_2 - x_3$ plane, Figure 5. The arbitrary subcell $(\beta\gamma)$ has length h_β, and width l_γ, where the $\beta = 1, 2, ..., N_\beta$; $\gamma = 1, 2, ..., N_\gamma$. In the original formulation, there are five unknown quantities associated with each subcell and four subcells within each generic cell, therefore, $20N_qN_r$ unknown coefficients must be determined by establishing a $20N_qN_r$ system of equations involving field equations and continuity conditions, together with the imposed thermal or heat flux boundary conditions. In the user-friendly formulation, there are still five unknown quantities in the temperature field expansion associated with every subcell, because the same temperature expansion is employed. Since the total number of subcells is $N_\beta N_\gamma$, $5N_\beta N_\gamma$ equations must be constructed for the determination of the unknown quantities. Although the number of unknowns in each subcell and the total number of equations remain the same in the user-friendly formulation (since $2N_q = N_\beta$ and $2N_r = N_\gamma$), the simplified notation leads to a more systematic method of assembling the final system of equations for the determination of the unknown coefficients in the temperature field expansion. More importantly, it also provides a basis for the efficient reformulation described in the next section.

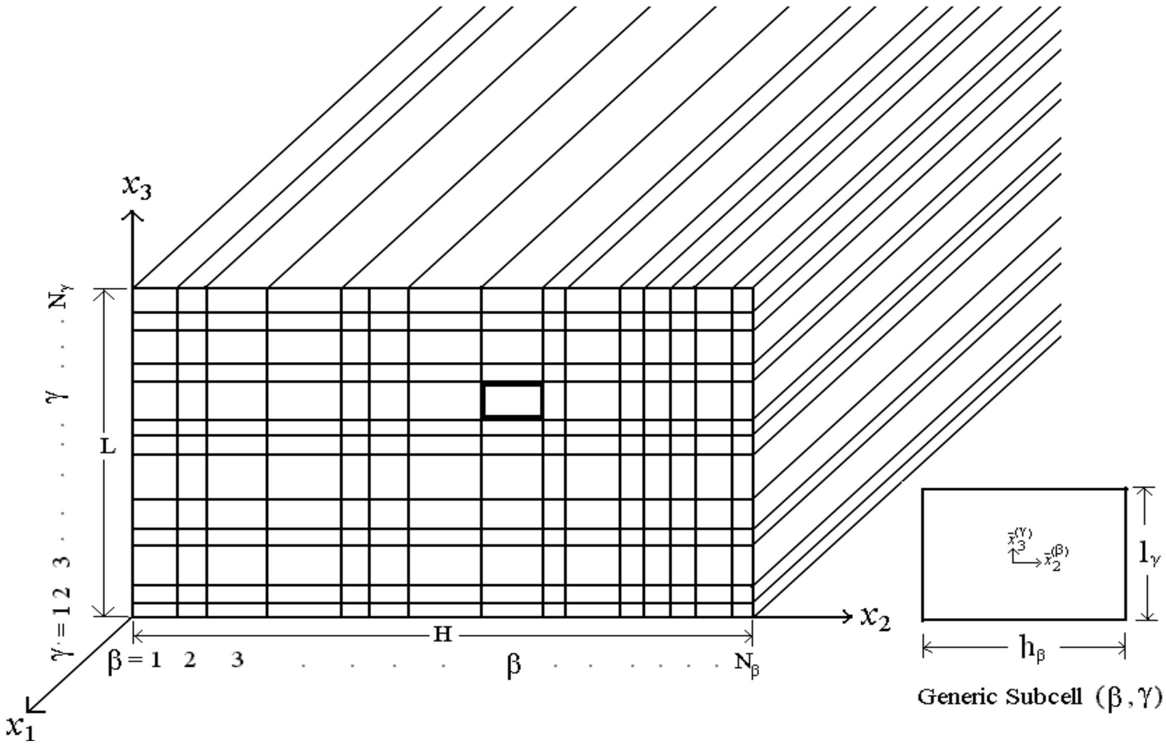

Figure 5. Schematic of the user-friendly HOTFGM formulation geometry.

2.2.1 Thermal analysis

As before, the temperature distribution $T^{(\beta\gamma)}$ in the subcell $(\beta\gamma)$ is approximated by

$$T^{(\beta\gamma)} = T^{(\beta\gamma)}_{(00)} + \bar{x}_2^{(\beta)} T^{(\beta\gamma)}_{(10)} + \bar{x}_3^{(\gamma)} T^{(\beta\gamma)}_{(01)} + \frac{1}{2}(3\bar{x}_2^{(\beta)2} - \frac{h_\beta^2}{4})T^{(\beta\gamma)}_{(20)} + \frac{1}{2}(3\bar{x}_3^{(\gamma)2} - \frac{l_\gamma^2}{4})T^{(\beta\gamma)}_{(02)} \tag{31}$$

Heat conduction equation As in the original formulation of HOTFGM-2D, under steady-state heat conduction, the heat flux field in the material occupying subcell $(\beta\gamma)$ in the region $|\bar{x}_1| < \infty$, $\left|\bar{x}_2^{(\beta)}\right| \le \frac{1}{2}h_\beta$, $\left|\bar{x}_3^{(\gamma)}\right| \le \frac{1}{2}l_\gamma$ must satisfy Eq. (1) in a volumetric sense,

$$\int_{V^{(\beta\gamma)}} (\frac{\partial q_2^{(\beta\gamma)}}{\partial \bar{x}_2^{(\beta)}} + \frac{\partial q_3^{(\beta\gamma)}}{\partial \bar{x}_3^{(\gamma)}}) dV^{(\beta\gamma)} = 0 \tag{32}$$

The heat flux components $q_2^{(\beta\gamma)}$ and $q_3^{(\beta\gamma)}$ can be expressed in terms of the unknown coefficients in the temperature field expansion, Eg. (31), using Eq. (2),

$$q_2^{(\beta\gamma)} = -k_2^{(\beta\gamma)} \frac{\partial T^{(\beta\gamma)}}{\partial \bar{x}_2^{(\beta)}} = -k_2^{(\beta\gamma)} (T^{(\beta\gamma)}_{(10)} + 3\bar{x}_2^{(\beta)} T^{(\beta\gamma)}_{(20)}) \tag{33}$$

$$q_3^{(\beta\gamma)} = -k_3^{(\beta\gamma)} \frac{\partial T^{(\beta\gamma)}}{\partial \bar{x}_3^{(\gamma)}} = -k_3^{(\beta\gamma)} (T^{(\beta\gamma)}_{(01)} + 3\bar{x}_3^{(\gamma)} T^{(\beta\gamma)}_{(02)}) \tag{34}$$

Therefore, substituting Eqs. (33) and (34) into the steady-state heat conduction equation, Eq. (32), yields,

$$k_2^{(\beta\gamma)} T_{(20)}^{(\beta\gamma)} + k_3^{(\beta\gamma)} T_{(02)}^{(\beta\gamma)} = 0 \tag{35}$$

This is the same equation as Eq.(21) in the original formulation at the subcell level, after replacing the temperature microvariables with the volume-averaged heat fluxes using Eqs. (18) and (20).

Heat flux continuity conditions between adjacent subcells Using the new generic cell-free notation, the heat flux continuity condition between adjacent subcell's along the x_2 direction is

$$\int_{-l_\gamma/2}^{l_\gamma/2} q_2^{(\beta,\gamma)} \mid_{\bar{x}_2=h_\beta/2} d\bar{x}_3^{(\gamma)} = \int_{-l_\gamma/2}^{l_\gamma/2} q_2^{(\beta+1,\gamma)} \mid_{\bar{x}_2=-h_{\beta+1}/2} d\bar{x}_3^{(\gamma)} \tag{36}$$

Substituting for the heat flux components in the x_2 direction using Eq. (33), the above equation becomes:

$$-k_2^{(\beta,\gamma)}(T_{(10)}^{(\beta,\gamma)} l_\gamma + \frac{3h_\beta}{2} T_{(20)}^{(\beta,\gamma)} l_\gamma) = -k_2^{(\beta+1,\gamma)}(T_{(10)}^{(\beta+1,\gamma)} l_\gamma - \frac{3h_{\beta+1}}{2} T_{(20)}^{(\beta+1,\gamma)} l_\gamma) \tag{37}$$

Similarly, the heat flux continuity condition along the x_3 direction is

$$\int_{-h_\beta/2}^{h_\beta/2} q_3^{(\beta,\gamma)} \mid_{\bar{x}_3=l_\gamma/2} d\bar{x}_2^{(\beta)} = \int_{-h_\beta/2}^{h_\beta/2} q_3^{(\beta,\gamma+1)} \mid_{\bar{x}_3=-l_{\gamma+1}/2} d\bar{x}_2^{(\beta)} \tag{38}$$

which, upon using Eq. (34), becomes

$$-k_3^{(\beta,\gamma)}(T_{(01)}^{(\beta,\gamma)} h_\beta + \frac{3l_\gamma}{2} T_{(02)}^{(\beta,\gamma)} h_\beta) = -k_3^{(\beta,\gamma+1)}(T_{(01)}^{(\beta,\gamma+1)} h_\beta - \frac{3l_{\gamma+1}}{2} T_{(02)}^{(\beta,\gamma+1)} h_\beta) \tag{39}$$

Thermal continuity conditions between adjacent subcells Using the new notation, the thermal continuity condition at adjacent subcells interfaces along the x_2 direction is,

$$\int_{-l_\gamma/2}^{l_\gamma/2} T^{(\beta\gamma)} \mid_{\bar{x}_2=h_\beta/2} d\bar{x}_3^{(\gamma)} = \int_{-l_\gamma/2}^{l_\gamma/2} T^{(\beta+1,\gamma)} \mid_{\bar{x}_2=-h_{\beta+1}/2} d\bar{x}_3^{(\gamma)} \tag{40}$$

Upon substituting for the temperature field defined by Eq. (31) and performing the required integration, the above condition reduces to

$$T_{(00)}^{(\beta\gamma)} l_\gamma + \frac{h_\beta l_\gamma}{2} T_{(10)}^{(\beta\gamma)} + \frac{h_\beta^2 l_\gamma}{4} T_{(20)}^{(\beta\gamma)} = T_{(00)}^{(\beta+1,\gamma)} l_\gamma - \frac{h_{\beta+1} l_\gamma}{2} T_{(10)}^{(\beta+1,\gamma)} + \frac{h_{\beta+1}^2 l_\gamma}{4} T_{(20)}^{(\beta+1,\gamma)} \tag{41}$$

Similarly, in the x_3 direction, the thermal continuity condition is,

$$\int_{-h_\beta/2}^{h_\beta/2} T^{(\beta\gamma)} \mid_{\bar{x}_3=l_\gamma/2} d\bar{x}_2^{(\beta)} = \int_{-h_\beta/2}^{h_\beta/2} T^{(\beta,\gamma+1)} \mid_{\bar{x}_3=-l_{\gamma+1}/2} d\bar{x}_2^{(\beta)} \tag{42}$$

which, upon using Eq. (31), becomes

$$T_{(00)}^{(\beta\gamma)} h_\beta + \frac{l_\gamma h_\beta}{2} T_{(01)}^{(\beta\gamma)} + \frac{l_\gamma^2 h_\beta}{4} T_{(02)}^{(\beta\gamma)} = T_{(00)}^{(\beta,\gamma+1)} h_\beta - \frac{l_{\gamma+1} h_\beta}{2} T_{(01)}^{(\beta,\gamma+1)} + \frac{l_{\gamma+1}^2 h_\beta}{4} T_{(02)}^{(\beta,\gamma+1)} \tag{43}$$

Boundary conditions The temperature or heat flux at the exterior surfaces of the boundary subcells $(\beta,1)$ and (β,N_γ) at $x_3=0$ and $x_3=L$, Figure 6, respectively, must equal the applied boundary condition (given temperature or given heat flux) in an average sense,

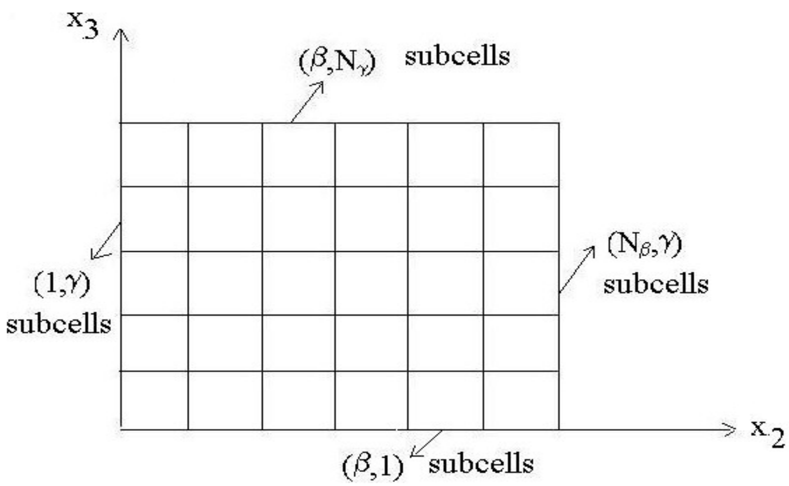

Figure 6. Boundary subcells.

$$\int_{-h_\beta/2}^{h_\beta/2} T^{(\beta,1)}|_{\bar{x}_3=-l_1/2} d\bar{x}_2^{(\beta)} = T_{(00)}^{(\beta,1)} - T_{(01)}^{(\beta,1)} l_1/2 + T_{(02)}^{(\beta,1)} l_1^2/4 = \int_{-h_\beta/2}^{h_\beta/2} T_{bot}^{(\beta)} d\bar{x}_2^{(\beta)} = \bar{T}_{bot}^{(\beta)} \quad (44)$$

or

$$\int_{-h_\beta/2}^{h_\beta/2} q_3^{(\beta,1)}|_{\bar{x}_3=-l_1/2} d\bar{x}_2^{(\beta)} = -k_3^{(\beta,1)}(T_{(01)}^{(\beta,1)} - 3l_1 T_{(02)}^{(\beta,1)}/2) = \int_{-h_\beta/2}^{h_\beta/2} q_{bot}^{(\beta)} d\bar{x}_2^{(\beta)} = \bar{q}_{bot}^{(\beta)} \quad (45)$$

and

$$\int_{-h_\beta/2}^{h_\beta/2} T^{(\beta,N_\gamma)}|_{\bar{x}_3=l_{N_\gamma}/2} d\bar{x}_2^{(\beta)} = T_{(00)}^{(\beta,N_\gamma)} + T_{(01)}^{(\beta,N_\gamma)} l_{N_\gamma}/2 + T_{(02)}^{(\beta,N_\gamma)} l_{N_\gamma}^2/4 = \int_{-h_\beta/2}^{h_\beta/2} T_{top}^{(\beta)} d\bar{x}_2^{(\beta)} = \bar{T}_{top}^{(\beta)} \quad (46)$$

or

$$\int_{-h_\beta/2}^{h_\beta/2} q_3^{(\beta,N_\gamma)}|_{\bar{x}_3=l_{N_\gamma}/2} d\bar{x}_2^{(\beta)} = -k_3^{(\beta,N_\gamma)}(T_{(01)}^{(\beta,N_\gamma)} + 3l_{N_\gamma} T_{(02)}^{(\beta,N_\gamma)}/2) = \int_{-h_\beta/2}^{h_\beta/2} q_{top}^{(\beta)} d\bar{x}_2^{(\beta)} = \bar{q}_{top}^{(\beta)} \quad (47)$$

Similarly the temperature or heat flux in the boundary subcells $(1,\gamma)$ and (N_β,γ) at $x_2=0$ and $x_2=H$ must be equal to the applied boundary condition (given temperature or given heat flux) in an average sense,

$$\int_{-l_\gamma/2}^{l_\gamma/2} T^{(1,\gamma)}|_{\bar{x}_2=-h_1/2} d\bar{x}_3^{(\gamma)} = T_{(00)}^{(1,\gamma)} - T_{(10)}^{(1,\gamma)} h_1/2 + T_{(20)}^{(1,\gamma)} h_1^2/4 = \int_{-l_\gamma/2}^{l_\gamma/2} T_{left}^{(\gamma)} d\bar{x}_3^{(\gamma)} = \bar{T}_{left}^{(\gamma)} \quad (48)$$

or

$$\int_{-l_\gamma/2}^{l_\gamma/2} q_2^{(1,\gamma)}|_{\bar{x}_2=-h_1/2} d\bar{x}_3^{(\gamma)} = -k_2^{(1,\gamma)}(T_{(10)}^{(1,\gamma)} - 3h_1 T_{(20)}^{(1,\gamma)}/2) = \int_{-l_\gamma/2}^{l_\gamma/2} q_{left}^{(\gamma)} d\bar{x}_3^{(\gamma)} = \bar{q}_{left}^{(\gamma)} \tag{49}$$

and

$$\int_{-l_\gamma/2}^{l_\gamma/2} T^{(N_\beta,\gamma)}|_{\bar{x}_2=h_{N_\beta}/2}\, d\bar{x}_3^{(\gamma)} = T_{(00)}^{(N_\beta,\gamma)} + T_{(10)}^{(N_\beta,\gamma)} h_{N_\beta}/2 + T_{(20)}^{(N_\beta,\gamma)} h_{N_\beta}^2/4 = \int_{-l_\gamma/2}^{l_\gamma/2} T_{right}^{(\gamma)} d\bar{x}_3^{(\gamma)} = \bar{T}_{right}^{(\gamma)} \tag{50}$$

or

$$\int_{-l_\gamma/2}^{l_\gamma/2} q_2^{(N_\beta,\gamma)}|_{\bar{x}_2=h_{N_\beta}/2} d\bar{x}_3^{(\gamma)} = -k_2^{(N_\beta,\gamma)}(T_{(10)}^{(N_\beta,\gamma)} + 3h_{N_\beta} T_{(20)}^{(N_\beta,\gamma)}/2) = \int_{-l_\gamma/2}^{l_\gamma/2} q_{right}^{(\gamma)} d\bar{x}_3^{(\gamma)} = \bar{q}_{right}^{(\gamma)} \tag{51}$$

2.2.2 Assembly of the governing equations

As stated before, there are five unknown quantities in the temperature field expansion associated with an arbitrary subcell $(\beta\gamma)$. They can be represented by the vector $\mathbf{T}^{(\beta\gamma)}$ defined as follows,

$$\mathbf{T}^{(\beta\gamma)} = [T_{(00)}, T_{(10)}, T_{(01)}, T_{(20)}, T_{(02)}]^{(\beta\gamma)} \tag{52}$$

Therefore, we need to construct five equations for every subcell to solve for the unknown coefficients. Two equations involve temperature continuity in the x_2 and x_3 directions, another two involve heat flux continuity in the x_2 and x_3 directions, and the remaining equation is the steady-state heat conduction equation. These will be arranged into an organized system of equations along each row sequence and column sequence of subcells representing the functionally graded material.

Let the assembly of the system of equations proceed first from left to right (in the x_2 direction) along each row of subcells starting from the first row, Figure 7. Subsequently, we proceed from bottom to top (in the x_3 direction) along each column of subcells starting from the first column. Finally, we take care of the steady-state heat equation within each subcell along either a row sequence or a column sequence. In summary, we obtain two equations at each interior interface along either direction after rearrangement, one involving temperature continuity and the other associated with heat flux continuity. We also obtain one steady-state heat equation for each subcell along either a row sequence or a column sequence for a total of five equations.

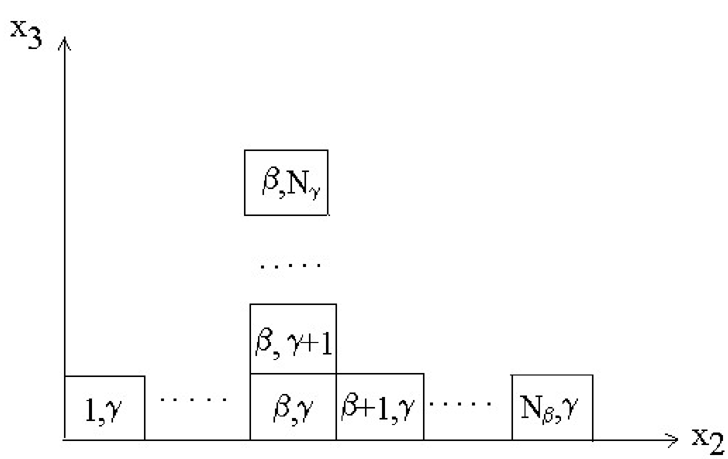

Figure 7. Governing equation assembly.

Continuity and boundary conditions along x_2 direction For a given γ, the left boundary condition, Eq. (48) or (49), can be rewritten in matrix form as follows,

$$\left[\mathbf{K}^B_{1\gamma}\right]\left[\mathbf{T}^{(1\gamma)}\right] = \bar{T}^{(\gamma)}_{left} \;\text{ or }\; \bar{q}^{(\gamma)}_{left} \tag{53}$$

where $\mathbf{K}^B_{1\gamma}$ depends on the applied boundary condition, and $\bar{T}^{(\gamma)}_{left}$ and $\bar{q}^{(\gamma)}_{left}$ are the surface integrals of the temperature and heat flux on the external surface of the boundary subcell $(1, \gamma)$ given by the right side of Eqs. (48) and (49). If the applied boundary condition is temperature, then

$$\mathbf{K}^B_{1\gamma} = \begin{bmatrix}1 & -h_1/2 & 0 & h_1^2/4 & 0\end{bmatrix}$$

Alternatively, if the applied boundary condition is heat flux, then

$$\mathbf{K}^B_{1\gamma} = \begin{bmatrix}0 & -k_2^{(1,\gamma)} & 0 & -3/2k_2^{(1,\gamma)}h_1 & 0\end{bmatrix}$$

The definition of $\mathbf{T}^{(\beta\gamma)}$ is given by Eq. (52).

Proceeding into the interior, we can rewrite the temperature and heat flux continuity conditions at the interface separating two adjacent subcells (β, γ) and $(\beta + 1, \gamma)$ in the interior, Eqs. (37) and (41), along the x_2 direction as follows,

$$\begin{bmatrix}\mathbf{K}^{T+}_{\beta\gamma} & \mathbf{K}^{T-}_{\beta+1,\gamma} \\ \mathbf{K}^{H+}_{\beta\gamma} & \mathbf{K}^{H-}_{\beta+1,\gamma}\end{bmatrix}\begin{bmatrix}\mathbf{T}^{(\beta\gamma)} \\ \mathbf{T}^{(\beta+1,\gamma)}\end{bmatrix} = \begin{bmatrix}0 \\ 0\end{bmatrix} \tag{54}$$

where

$$\mathbf{K}^{T+}_{\beta\gamma} = \begin{bmatrix}1 & h_\beta/2 & 0 & h_\beta^2/4 & 0\end{bmatrix}$$

$$\mathbf{K}^{T-}_{\beta+1,\gamma} = \begin{bmatrix}-1 & h_{\beta+1}/2 & 0 & -h_{\beta+1}^2/4 & 0\end{bmatrix}$$

$$\mathbf{K}^{H+}_{\beta\gamma} = \begin{bmatrix}0 & -k_2^{(\beta\gamma)} & 0 & -3/2h_\beta k_2^{(\beta\gamma)} & 0\end{bmatrix}$$

$$\mathbf{K}^{H-}_{\beta+1,\gamma} = \begin{bmatrix}0 & k_2^{(\beta+1,\gamma)} & 0 & -3/2h_{\beta+1}k_2^{(\beta+1,\gamma)} & 0\end{bmatrix}$$

and $\beta = 1, 2, ..., N_\beta - 1$.

Finally, the right boundary condition, Eq. (50) and (51), can be rewritten in matrix form as,

$$\left[\mathbf{K}^B_{N_\beta\gamma}\right]\left[\mathbf{T}^{(N_\beta,\gamma)}\right] = \bar{T}^{(\gamma)}_{right} \;\text{ or }\; \bar{q}^{(\gamma)}_{right} \tag{55}$$

where $\mathbf{K}_{N_\beta,\gamma}$ depends on the applied boundary condition, and $\bar{T}^{(\gamma)}_{right}$ and $\bar{q}^{(\gamma)}_{right}$ are the surface integrals of the temperature and heat flux on the external surface of the boundary subcell (N_β, γ) given by the right side of Eqs. (50) and (51). If the boundary condition is temperature, then

$$\mathbf{K}_{N_\beta,\gamma} = \begin{bmatrix}1 & h_{N_\beta}/2 & 0 & h_{N_\beta}^2/4 & 0\end{bmatrix}$$

Alternatively, if the applied boundary condition is heat flux, then

$$\mathbf{K}_{N_\beta,\gamma} = \begin{bmatrix}0 & -k_2^{(N_\beta,\gamma)} & 0 & -3/2k_2^{(N_\beta,\gamma)}h_{N_\beta} & 0\end{bmatrix}$$

Therefore, for an arbitrary row γ, let $\beta = 1, ..., N_\beta$, Figure 7, and apply the above equations from the left boundary to the right boundary, respectively. This procedure produces a system of equations defined by the matrix $\mathbf{K}_\gamma^{(\vec{\beta})}$, which contains information on the left boundary condition, temperature and heat flux continuity conditions at the interfaces between adjacent subcells, and the right boundary condition, respectively, along the row sequence. The structure of $\mathbf{K}_\gamma^{(\vec{\beta})}$, whose size is $2N_\beta \times 5N_\beta$, is shown below,

$$\mathbf{K}_\gamma^{(\vec{\beta})} = \begin{bmatrix} \mathbf{K}_{1\gamma}^{B} & \mathbf{0} & \mathbf{0} & \mathbf{0} & \mathbf{0} & \mathbf{0} & \mathbf{0} \\ \ldots\ldots & \ldots\ldots & \mathbf{0} & \mathbf{0} & \mathbf{0} & \mathbf{0} & \mathbf{0} \\ \mathbf{0} & \mathbf{0} & \mathbf{K}_{\beta\gamma}^{T+} & \mathbf{K}_{\beta+1,\gamma}^{T-} & \mathbf{0} & \mathbf{0} & \mathbf{0} \\ \mathbf{0} & \mathbf{0} & \mathbf{K}_{\beta\gamma}^{H+} & \mathbf{K}_{\beta+1,\gamma}^{H-} & \mathbf{0} & \mathbf{0} & \mathbf{0} \\ \mathbf{0} & \mathbf{0} & \mathbf{0} & \mathbf{K}_{\beta+1,\gamma}^{T+} & \mathbf{K}_{\beta+2,\gamma}^{T-} & \mathbf{0} & \mathbf{0} \\ \mathbf{0} & \mathbf{0} & \mathbf{0} & \mathbf{K}_{\beta+1,\gamma}^{H+} & \mathbf{K}_{\beta+2,\gamma}^{H-} & \mathbf{0} & \mathbf{0} \\ \mathbf{0} & \mathbf{0} & \mathbf{0} & \mathbf{0} & \mathbf{0} & \ldots\ldots. & \ldots\ldots \\ \mathbf{0} & \mathbf{0} & \mathbf{0} & \mathbf{0} & \mathbf{0} & \mathbf{0} & \mathbf{K}_{N_\beta,\gamma}^{B} \end{bmatrix}$$

Following the same procedure applied to every row, $\gamma = 1, 2, ...N_\gamma$, we obtain a system of equations defined by the matrix $\mathbf{A}$, consisting of the individual matrices $\mathbf{K}_\gamma^{(\vec{\beta})}$, that has the form,

$$\mathbf{A} = \begin{bmatrix} \mathbf{K}_1^{(\vec{\beta})} & \mathbf{0} & \mathbf{0} & \mathbf{0} & \mathbf{0} \\ \mathbf{0} & \ldots.. & \mathbf{0} & \mathbf{0} & \mathbf{0} \\ \mathbf{0} & \mathbf{0} & \mathbf{K}_\gamma^{(\vec{\beta})} & \mathbf{0} & \mathbf{0} \\ \mathbf{0} & \mathbf{0} & \mathbf{0} & \ldots\ldots & \mathbf{0} \\ \mathbf{0} & \mathbf{0} & \mathbf{0} & \mathbf{0} & \mathbf{K}_{N_\gamma}^{(\vec{\beta})} \end{bmatrix}$$

Since the matrix $\mathbf{A}$ consists of N_γ matrices $\mathbf{K}_\gamma^{(\vec{\beta})}$ placed along the main diagonal, its size is $2N_\beta N\gamma \times 5N_\beta N_\gamma$.

Continuity and boundary conditions along x_3 direction Repeating the preceding procedure along the x_3 direction, the bottom boundary condition, Eq. (44) or (45), for a given β, can be rewritten in matrix form as follows,

$$\left[\hat{\mathbf{K}}_{\beta 1}^{B}\right]\left[\mathbf{T}^{(\beta 1)}\right] = \bar{T}_{bot}^{(\beta)} \quad \text{or} \quad \bar{q}_{bot}^{(\beta)} \tag{56}$$

As in the case of the boundary matrix $\mathbf{K}_{1\gamma}^{B}$ in $\mathbf{A}$, $\hat{\mathbf{K}}_{\beta 1}^{B}$ also can be obtained in two ways. When temperature is applied to the boundary, then we get

$$\hat{\mathbf{K}}_{\beta 1}^{B} = \begin{bmatrix} 1 & 0 & -l_1/2 & 0 & l_1^2/4 \end{bmatrix}$$

Alternatively, when the boundary condition involves heat flux, we get

$$\hat{\mathbf{K}}_{\beta 1}^{B} = \begin{bmatrix} 0 & 0 & -k_3^{(\beta 1)} & 0 & 3/2 k_3^{(\beta 1)} l_1 \end{bmatrix}$$

$\bar{T}_{bot}^{(\beta)}$ and $\bar{q}_{bot}^{(\beta)}$ are the surface integrals of the temperature and heat flux on the external surface of the boundary subcell $(\beta, 1)$ given by the right side of Eqs. (44) and (45).

Proceeding into the interior, we can assemble the temperature and heat flux continuity conditions at the interface separating two adjacent subcells (β,γ) and $(\beta,\gamma+1)$ in the interior, Eqs. (39) and (43), along the x_3 direction as follows,

$$\begin{bmatrix} \hat{\mathbf{K}}^{T+}_{\beta\gamma} & \hat{\mathbf{K}}^{T-}_{\beta,\gamma+1} \\ \hat{\mathbf{K}}^{H+}_{\beta\gamma} & \hat{\mathbf{K}}^{H-}_{\beta,\gamma+1} \end{bmatrix} \begin{bmatrix} \mathbf{T}^{(\beta\gamma)} \\ \mathbf{T}^{(\beta,\gamma+1)} \end{bmatrix} = \begin{bmatrix} 0 \\ 0 \end{bmatrix} \tag{57}$$

where

$$\hat{\mathbf{K}}^{T+}_{\beta\gamma} = \begin{bmatrix} 1 & 0 & l_\gamma/2 & 0 & l_\gamma^2/4 \end{bmatrix}$$

$$\hat{\mathbf{K}}^{T-}_{\beta,\gamma+1} = \begin{bmatrix} -1 & 0 & l_{\gamma+1}/2 & 0 & -l_{\gamma+1}^2/4 \end{bmatrix}$$

$$\hat{\mathbf{K}}^{H+}_{\beta\gamma} = \begin{bmatrix} 0 & 0 & -k_3^{(\beta\gamma)} & 0 & -3/2 k_3^{(\beta\gamma)} l_\gamma \end{bmatrix}$$

$$\hat{\mathbf{K}}^{H-}_{\beta,\gamma+1} = \begin{bmatrix} 0 & 0 & k_3^{(\beta,\gamma+1)} & 0 & -3/2 k_3^{(\beta,\gamma+1)} l_{\gamma+1} \end{bmatrix}$$

and $\gamma = 1, ..., N_\gamma - 1$.

Finally, we rewrite the top boundary condition, Eq. (46) or (47), in matrix form as,

$$\begin{bmatrix} \hat{\mathbf{K}}^{B}_{\beta,N_\gamma} \end{bmatrix} \begin{bmatrix} \mathbf{T}^{(\beta,N_\gamma)} \end{bmatrix} = \bar{T}^{(\beta)}_{top} \text{ or } \bar{q}^{(\beta)}_{top} \tag{58}$$

where $\bar{T}^{(\beta)}_{top}$ and $\bar{q}^{(\beta)}_{top}$ are the surface integrals of the temperature and heat flux on the external surface of the boundary subcell (β, N_γ) given by the right side of Eqs. (46) and (47). If the applied boundary condition is temperature defined as $\bar{T}^{(\beta)}_{top}$, then

$$\hat{\mathbf{K}}^{B}_{\beta,N_\gamma} = \begin{bmatrix} 1 & 0 & l_{N_\gamma}/2 & 0 & l^2_{N_\gamma}/4 \end{bmatrix}$$

Similarly, if the boundary is subjected to heat flux given by the form $\bar{q}^{(\beta)}_{top}$, then we obtain

$$\hat{\mathbf{K}}^{B}_{\beta,N_\gamma} = \begin{bmatrix} 0 & 0 & -k_3^{(\beta,N_\gamma)} & 0 & 3/2 k_3^{(\beta,N_\gamma)} l_{N_\gamma} \end{bmatrix}$$

Following these steps, for an arbitrary column β, letting $\gamma = 1 \to N_\gamma$, Figure 7, we construct a system of equations defined by the matrix $\hat{\mathbf{K}}^{(\vec{\gamma})}_\beta$ which contains information on the bottom boundary, interfacial temperature and heat flux continuity conditions, and the top boundary, respectively, along the column sequence (i.e., in the x_3 direction).

$$\hat{\mathbf{K}}^{(\vec{\gamma})}_\beta = \begin{bmatrix} . & \hat{\mathbf{K}}^B_{\beta 1} & .. & \mathbf{0} & .. & \mathbf{0} & .. & \mathbf{0} & .. & \mathbf{0} & ... \\ . & \cdot & .. & \mathbf{0} & .. & \mathbf{0} & .. & \mathbf{0} & .. & \mathbf{0} & ... \\ . & \mathbf{0} & .. & \hat{\mathbf{K}}^{T+}_{\beta\gamma} & .. & \hat{\mathbf{K}}^{T-}_{\beta,\gamma+1} & .. & \mathbf{0} & .. & \mathbf{0} & ... \\ . & \mathbf{0} & .. & \hat{\mathbf{K}}^{H+}_{\beta\gamma} & .. & \hat{\mathbf{K}}^{H-}_{\beta,\gamma+1} & .. & \mathbf{0} & .. & \mathbf{0} & ... \\ . & \mathbf{0} & .. & \mathbf{0} & .. & \hat{\mathbf{K}}^{T+}_{\beta,\gamma+1} & .. & \hat{\mathbf{K}}^{T-}_{\beta,\gamma+2} & .. & \mathbf{0} & ... \\ . & \mathbf{0} & .. & \mathbf{0} & .. & \hat{\mathbf{K}}^{H+}_{\beta,\gamma+1} & .. & \hat{\mathbf{K}}^{H-}_{\beta,\gamma+2} & .. & \mathbf{0} & ... \\ . & \mathbf{0} & .. & \mathbf{0} & .. & \mathbf{0} & .. & \mathbf{0} & .. & \cdot & ... \\ . & \mathbf{0} & .. & \mathbf{0} & .. & \mathbf{0} & .. & \mathbf{0} & .. & \hat{\mathbf{K}}^B_{\beta,N_\gamma} & ... \end{bmatrix}$$

In the above matrix, the designation . indicates $\beta - 1$ $\mathbf{0}$ matrices, the designation .. indicates $N_\beta - 1$ $\mathbf{0}$ matrices, and the designation ... indicates $N_\beta - \beta$ $\mathbf{0}$ matrices, with the zero matrices having the dimensions $[1 \times 5]$. The size of the $\hat{\mathbf{K}}_\beta^{(\vec{\gamma})}$ matrices is $2N_\gamma \times 5N_\beta N_\gamma$.

Extending $\hat{\mathbf{K}}_\beta^{(\vec{\gamma})}$ to all β, $\beta = 1, 2, ..., N_\beta$, we obtain the matrix $\mathbf{B}$ that has the form

$$\mathbf{B} = \begin{bmatrix} \mathbf{K}_1^{(\vec{\gamma})} \\ ...... \\ \mathbf{K}_\beta^{(\vec{\gamma})} \\ ...... \\ \mathbf{K}_{N_\beta}^{(\vec{\gamma})} \end{bmatrix}$$

with $\mathbf{B}$ having the dimensions $2N_\beta N_\gamma \times 5N_\beta N_\gamma$.

Heat conduction equation in x_2 or x_3 direction Finally, we write the steady-state heat conduction equation, Eq. (35), for an arbitrary $(\beta\gamma)$ subcell as follows

$$\left[\mathbf{K}_\gamma^{*(\beta,\gamma)}\right]\left[\mathbf{T}^{(\beta\gamma)}\right] = 0$$

where

$$\mathbf{K}_\gamma^{*(\beta,\gamma)} = [0 \;\; 0 \;\; 0 \;\; -3k_2^{(\beta\gamma)} \;\; -3k_3^{(\beta\gamma)}]$$

Assuming that the assembly proceeds from left to right along a row sequence, we obtain the matrix $\mathbf{K}_\gamma^{*(\vec{\beta})}$ with dimensions $N_\beta \times 5N_\beta$ for a given γ row of subcells

$$\mathbf{K}_\gamma^{*(\vec{\beta})} = \begin{bmatrix} \mathbf{K}_\gamma^{*(1,\gamma)} & \mathbf{0} & \mathbf{0} & \mathbf{0} & \mathbf{0} \\ \mathbf{0} & .... & \mathbf{0} & \mathbf{0} & \mathbf{0} \\ \mathbf{0} & \mathbf{0} & \mathbf{K}_\gamma^{*(\beta,\gamma)} & \mathbf{0} & \mathbf{0} \\ \mathbf{0} & \mathbf{0} & \mathbf{0} & .... & \mathbf{0} \\ \mathbf{0} & \mathbf{0} & \mathbf{0} & \mathbf{0} & \mathbf{K}_\gamma^{*(N_\beta,\gamma)} \end{bmatrix}$$

where $\beta = 1, 2, ...N_\beta$ along the diagonal, respectively.

Extending the procedure to all γ, we obtain the final system of equations that satisfies the heat conduction equation in every subcell. This system of equation is represented by the matrix $\mathbf{C}$, which contains the individual matrices $\mathbf{K}_\gamma^{*(\vec{\beta})}$ along its diagonal as shown below.

$$\mathbf{C} = \begin{bmatrix} \mathbf{K}_1^{*(\vec{\beta})} & \mathbf{0} & \mathbf{0} & \mathbf{0} & \mathbf{0} \\ \mathbf{0} & ..... & \mathbf{0} & \mathbf{0} & \mathbf{0} \\ \mathbf{0} & \mathbf{0} & \mathbf{K}_\gamma^{*(\vec{\beta})} & \mathbf{0} & \mathbf{0} \\ \mathbf{0} & \mathbf{0} & \mathbf{0} & ...... & \mathbf{0} \\ \mathbf{0} & \mathbf{0} & \mathbf{0} & \mathbf{0} & \mathbf{K}_{N_\gamma}^{*(\vec{\beta})} \end{bmatrix}$$

where $\gamma = 1, 2, ...N_\gamma$, respectively, along the diagonal. Since the matrix $\mathbf{C}$ consists of N_γ matrices $\mathbf{K}_\gamma^{*(\vec{\beta})}$ placed along the diagonal, its size is $N_\beta N_\gamma \times 5N_\beta N_\gamma$.

Governing equations The governing equations for the interior and boundary subcells form a system of $5N_\beta N\gamma$ algebraic equations in the $5N_\beta N_\gamma$ unknown coefficients $T^{(\beta\gamma)}_{(mn)}$. This system of equations can be written symbolically as

$$\mathbf{kT} = \mathbf{t} \tag{59}$$

where $\mathbf{k}$ is the structural thermal conductivity matrix. It contains information on the geometry and thermal conductivity of every subcell. The matrix $\mathbf{k}$ is made up of three submatrices as follows

$$\mathbf{k} = \begin{bmatrix} \mathbf{A} \\ \mathbf{B} \\ \mathbf{C} \end{bmatrix} \tag{60}$$

$\mathbf{T}$ is the thermal coefficient vector. It contains the unknown coefficients that describe the temperature field in all the subcells arranged as follows

$$\mathbf{T} = [\mathbf{T}_1, ..., \mathbf{T}_\gamma, ...\mathbf{T}_{N_\gamma}] \tag{61}$$

where

$$\mathbf{T}_\gamma = [\mathbf{T}^{(1\gamma)}, ..., \mathbf{T}^{(\beta\gamma)}, ...\mathbf{T}^{(N_\beta\gamma)}] \tag{62}$$

with $\mathbf{T}^{(\beta\gamma)}$ defined previously in Eq. (52). Finally, $\mathbf{t}$ is the thermal force vector. It contains information on the boundary conditions specified either in terms of temperatures or heat fluxes.

In summary, the elimination of generic cells in the user-friendly formulation has resulted in a system of equations which is easier to visualize and implement in a computer code. Most importantly, the new formulation based on subcells as the basic building blocks sets the stage for an efficient reformulation presented in the next section.

3 Reformulation

The user-friendly formulation of HOTFGM-2D, which was presented in the preceding section, illustrates the feasibility of eliminating the distinction between generic cells and subcells. It should be noted that the simplified geometric model played an important role in the entire analytical process. In other words, the basic building block defined by the subcell itself without a generic cell, which was used to construct the heterogeneous composite, made the indices simpler and the derivation process more straightforward. More importantly, formulating the higher-order theory solely in terms of subcells, which play the role of generic subvolumes, reduces it to a standard thermal boundary-value problem on a discretized domain, thereby facilitating the search for a more efficient solution method.

As discussed by Pindera (1991), the local/global stiffness matrix method is an efficient algorithm for solving mixed boundary-value problems in composite mechanics. This method is particularly well suited to problems involving layered composite materials or structures that require satisfaction of both continuity of tractions and displacements in mechanical problems, or temperature and heat flux in thermal problems, along common interfaces. The method thus far has been applied to layered media composed of continuous layers in Cartesian coordinates, or circular concentric rings/cylinders in polar coordinates. Examples of the method's application include axisymmetric and axial shear problems involving multiple concentric cylinders, Pindera et al. (1993) and Williams and Pindera (1997), composite tube problems, Salzar et al. (1996), a layered composite cylinder subjected to diametral loading, Davison et al. (1994), and contact problems, Pindera and Lane (1993) and Urquhart and Pindera (1994). The local/global stiffness matrix method is based on

a systematic construction of a global stiffness matrix (mechanical problem) or global conductivity matrix (thermal problem) for the entire composite structure in terms of local stiffness matrices (mechanical problem) or local conductivity matrices (thermal problem) of individual layers. Herein, we extend this method to HOTFGM-2D where the volume discretization involves subvolumes of finite dimensions in the $x_2 - x_3$ plane defined by the subcells $(\beta\gamma)$. Since we only discuss the thermal problem here, we will call it henceforth the local/global conductivity matrix method.

In the local/global conductivity matrix method, the local conductivity matrix provides a connection between the surface-averaged heat flux and the corresponding surface-averaged temperature components at top, bottom, left and right surfaces of a given subcell. The assembly of local conductivity matrices into the global conductivity matrix is based on the direct enforcement of continuity conditions along the subcell interfaces, and the interfacial temperatures are considered as the basic unknown variables in the reformulation. Therefore, for a volume discretized into $N_\beta N\gamma$ subcells, the total number of interfacial surface-averaged temperatures will be $(N_\beta + 1)N_\gamma + (N_\gamma + 1)N_\beta$, which includes both the interior subcell interfaces and the external surfaces of boundary subcells.

For a given $(\beta\gamma)$ subcell, the local conductivity matrix can be expressed as follows,

$$\begin{bmatrix} -\bar{Q}_2^- \\ \bar{Q}_2^+ \\ -\bar{Q}_3^- \\ \bar{Q}_3^+ \end{bmatrix}^{(\beta\gamma)} = \begin{bmatrix} \kappa_{11} & \kappa_{12} & \kappa_{13} & \kappa_{14} \\ \kappa_{21} & \kappa_{22} & \kappa_{23} & \kappa_{24} \\ \kappa_{31} & \kappa_{32} & \kappa_{33} & \kappa_{34} \\ \kappa_{41} & \kappa_{42} & \kappa_{43} & \kappa_{44} \end{bmatrix}^{(\beta\gamma)} \begin{bmatrix} \bar{T}_2^- \\ \bar{T}_2^+ \\ \bar{T}_3^- \\ \bar{T}_3^+ \end{bmatrix}^{(\beta\gamma)} \tag{63}$$

It relates the surface-averaged heat flux components $-(\bar{Q}_2^-)^{(\beta\gamma)}, (\bar{Q}_2^+)^{(\beta\gamma)}, -(\bar{Q}_3^-)^{(\beta\gamma)}, (\bar{Q}_3^+)^{(\beta\gamma)}$ on the left, right, top and bottom surfaces of a given subcell to their corresponding surface-averaged temperatures $(\bar{T}_2^-)^{(\beta\gamma)}, (\bar{T}_2^+)^{(\beta\gamma)}, (\bar{T}_3^-)^{(\beta\gamma)}, (\bar{T}_3^+)^{(\beta\gamma)}$, Figure 8. The superscripts + and - refer to the corresponding heat flux or temperature acting on the right/top surface and left/bottom surface of a given subcell. The subscripts 2 and 3 indicate the x_2 and x_3 directions, respectively. The minus signs in front of the heat flux components $\bar{Q}_2^-, \bar{Q}_3^-$ indicate that the direction of the heat flux vector coincides with the direction of the unit normal vector associated with the left and bottom surfaces of the $(\beta\gamma)$ subcell.

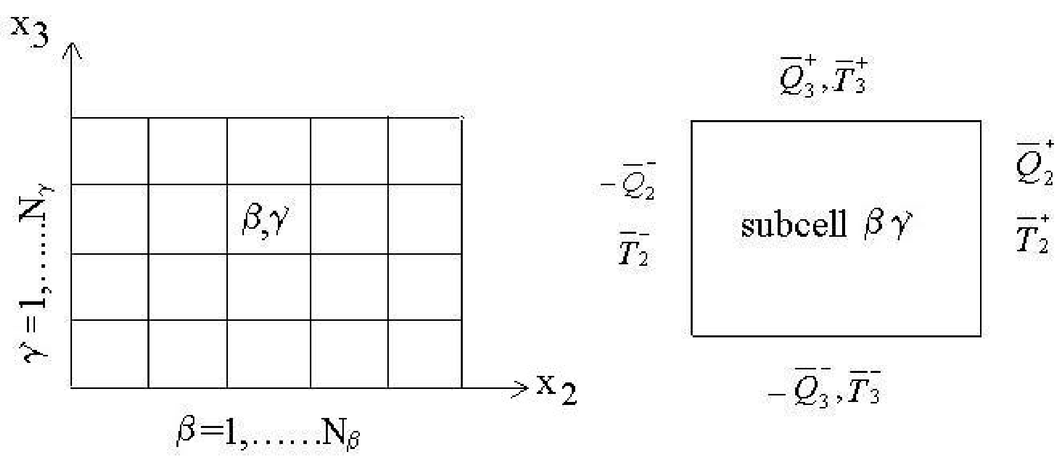

Figure 8. Definition of surface-averaged temperatures and heat fluxes.

Using the Fourier's heat conduction law for orthotropic materials, Eqs. (33)-(34),

$$q_2^{(\beta\gamma)} = -k_2^{(\beta\gamma)} \frac{\partial T^{(\beta\gamma)}}{\partial \bar{x}_2^{(\beta)}}, \qquad q_3^{(\beta\gamma)} = -k_3^{(\beta\gamma)} \frac{\partial T^{(\beta\gamma)}}{\partial \bar{x}_3^{(\gamma)}}$$

the definitions of surface-averaged heat fluxes and temperatures in Eq. (63) are:

$$(\bar{Q}_2^{+})^{(\beta\gamma)} = \frac{1}{l\gamma} \int_{-l_\gamma/2}^{l_\gamma/2} -k_2^{(\beta\gamma)} \frac{\partial T^{(\beta\gamma)}}{\partial \bar{x}_2^{(\beta)}} \mid_{\bar{x}_2^{(\beta)}=h_\beta/2} d\bar{x}_3^{(\gamma)} \tag{64}$$

$$(\bar{Q}_2^{-})^{(\beta\gamma)} = \frac{1}{l\gamma} \int_{-l_\gamma/2}^{l_\gamma/2} -k_2^{(\beta\gamma)} \frac{\partial T^{(\beta\gamma)}}{\partial \bar{x}_2^{(\beta)}} \mid_{\bar{x}_2^{(\beta)}=-h_\beta/2} d\bar{x}_3^{(\gamma)} \tag{65}$$

$$(\bar{Q}_3^{+})^{(\beta\gamma)} = \frac{1}{h_\beta} \int_{-h_\beta/2}^{h_\beta/2} -k_3^{(\beta\gamma)} \frac{\partial T^{(\beta\gamma)}}{\partial \bar{x}_3^{(\gamma)}} \mid_{\bar{x}_3^{(\gamma)}=l_\gamma/2} d\bar{x}_2^{(\beta)} \tag{66}$$

$$(\bar{Q}_3^{-})^{(\beta\gamma)} = \frac{1}{h_\beta} \int_{-h_\beta/2}^{h_\beta/2} -k_3^{(\beta\gamma)} \frac{\partial T^{(\beta\gamma)}}{\partial \bar{x}_3^{(\gamma)}} \mid_{\bar{x}_3^{(\gamma)}=-l_\gamma/2} d\bar{x}_2^{(\beta)} \tag{67}$$

and

$$(\bar{T}_2^{+})^{(\beta\gamma)} = \frac{1}{l_\gamma} \int_{-l\gamma/2}^{l_\gamma/2} T_2^{(\beta\gamma)} \mid_{\bar{x}_2^{(\beta)}=h_\beta/2} d\bar{x}_3^{(\gamma)} \tag{68}$$

$$(\bar{T}_2^{-})^{(\beta\gamma)} = \frac{1}{l_\gamma} \int_{-l\gamma/2}^{l_\gamma/2} T_2^{(\beta\gamma)} \mid_{\bar{x}_2^{(\beta)}=-h_\beta/2} d\bar{x}_3^{(\gamma)} \tag{69}$$

$$(\bar{T}_3^{+})^{(\beta\gamma)} = \frac{1}{h_\beta} \int_{-h_\beta/2}^{h_\beta/2} T_3^{(\beta\gamma)} \mid_{\bar{x}_3^{(\gamma)}=l_\gamma/2} d\bar{x}_2^{(\beta)} \tag{70}$$

$$(\bar{T}_3^{-})^{(\beta\gamma)} = \frac{1}{h_\beta} \int_{-h_\beta/2}^{h_\beta/2} T_3^{(\beta\gamma)} \mid_{\bar{x}_3^{(\gamma)}=l_\gamma/2} d\bar{x}_2^{(\beta)} \tag{71}$$

The detailed derivation of the elements of the local conductivity matrix in Eq. (63) will be outlined in the following section.

Imposition of continuity of heat flux and temperature along common subcell interfaces, together with the external boundary conditions, gives rise to a system of equations in the unknown interfacial temperatures along the x_2 and x_3 directions, respectively. The continuity of interfacial heat flux is ensured by requiring that the sum of the heat fluxes acting on the interface separating (β, γ) and $(\beta + 1, \gamma)$ subcells and the interface separating (β, γ) and $(\beta, \gamma + 1)$ subcells be zero, i.e.,

$$\begin{aligned} (\bar{Q}_2^{+})^{(\beta,\gamma)} + (-\bar{Q}_2^{-})^{(\beta+1,\gamma)} &= 0, && (72) \\ (\bar{Q}_3^{+})^{(\beta,\gamma)} + (-\bar{Q}_3^{-})^{(\beta,\gamma+1)} &= 0 && (73) \end{aligned}$$

where $\beta = 1, 2, ...N_\beta - 1$ and $\gamma = 1, 2, ...N_\gamma - 1$. The thermal continuity is directly enforced by setting the surface-averaged temperatures along interfaces separating adjacent subcells to common values,

$$\begin{aligned} (\bar{T}_2^{+})^{(\beta,\gamma)} &= (\bar{T}_2^{-})^{(\beta+1,\gamma)} = \bar{T}_2^{(\beta+1,\gamma)} && (74) \\ (\bar{T}_3^{+})^{(\beta,\gamma)} &= (\bar{T}_3^{-})^{(\beta,\gamma+1)} = \bar{T}_3^{(\beta,\gamma+1)} && (75) \end{aligned}$$

The system of equations is constructed by applying Eqs. (72)-(75) in conjunction with Eq. (63) to each interface, starting first with the left boundary in the first row of subcells where the boundary condition is prescribed and then progressing in the x_2 direction to each interface separating adjacent interior subcells, and then finally the right boundary with the prescribed boundary condition. This procedure is repeated along every row of subcells. We then repeat the same procedure in the x_3 direction, starting at the bottom of the first column and proceeding up, and then repeating it for each subsequent column. At each interface, the thermal continuity expressed in terms of the common interfacial temperatures defined by Eqs. (74) and (75) is directly enforced in the heat flux continuity conditions given by Eqs. (72) and (73) through the use of Eq. (63). Actually, the assembly of the global conductivity matrix for the entire structure is carried out by superposing local conductivity matrices of individual subcells along x_2 and x_3 directions, respectively, in the manner that will be described in Section 3.3.

Since the continuity of interfacial temperatures is enforced directly through Eqs. (74) and (75) along x_2 and x_3 directions, respectively, the above procedure results in the elimination of a substantial number of redundant interfacial continuity equations which are retained in the original formulation. Thus the reformulation simplifies the computational procedure for thermal boundary-value problems by reducing the size of the global conductivity matrix, which can be large for a large number of subcells. Furthermore, the global conductivity matrix can be generated systematically and automatically, thereby facilitating numerical implementation for any number of subcells.

The above presentation illustrates the general formulation process of the local/global conductivity matrix method in solving thermal boundary-value problems. In the following, the detailed derivation of how to construct the local conductivity matrix based on the generic cell-free formulation of HOTFGM-2D problem is outlined. It is should be noted that herein the thermal conductivity coefficients $k_2^{(\beta\gamma)}$ and $k_3^{(\beta\gamma)}$ are assumed to vary with local subcell coordinates. The same problem but with constant thermal conductivity coefficients was investigated by Bansal (2002).

3.1 Local Conductivity Matrix: Variable Thermal Conductivity

In the present work, the thermal conductivity coefficients $k_2^{(\beta\gamma)}$ and $k_3^{(\beta\gamma)}$ in each $(\beta\gamma)$ subcell are assumed to vary linearly with the local subcell coordinates $\bar{x}_2^{(\beta)}$ and $\bar{x}_3^{(\gamma)}$ as follows

$$k_2^{(\beta\gamma)} = k_{20}^{(\beta\gamma)} + k_{22}^{(\beta\gamma)}\bar{x}_2^{(\beta)} + k_{23}^{(\beta\gamma)}\bar{x}_3^{(\gamma)} \tag{76}$$

$$k_3^{(\beta\gamma)} = k_{30}^{(\beta\gamma)} + k_{32}^{(\beta\gamma)}\bar{x}_2^{(\beta)} + k_{33}^{(\beta\gamma)}\bar{x}_3^{(\gamma)} \tag{77}$$

We note that $k_{23}^{(\beta\gamma)}$ and $k_{32}^{(\beta\gamma)}$ cannot be completely arbitrary as they do not explicitly appear in the surface-averaged heat fluxes and the volume-averaged heat conduction equation derived in the sequel. This is a direct result of the averaging technique employed in the higher-order theory. Therefore, we must impose the following constraint for consistency: $k_{23}^{(\beta\gamma)} = k_{32}^{(\beta\gamma)} = 0$. In other words, we obtain one-dimensional variation of $k_2^{(\beta\gamma)}$ and $k_3^{(\beta\gamma)}$ along the respective directions, if linear thermal conductivity variation is assumed.

As before, the temperature field in the subcell $(\beta\gamma)$ is approximated by a second-order expansion in the local coordinates $\bar{x}_2^{(\beta)}, \bar{x}_3^{(\gamma)}$ in the following way (see Eq. (31))

$$T^{(\beta\gamma)} = T_{(00)}^{(\beta\gamma)} + \bar{x}_2^{(\beta)}T_{(10)}^{(\beta\gamma)} + \bar{x}_3^{(\gamma)}T_{(01)}^{(\beta\gamma)} + \frac{1}{2}(3\bar{x}_2^{(\beta)2} - \frac{h_\beta^2}{4})T_{(20)}^{(\beta\gamma)} + \frac{1}{2}(3\bar{x}_3^{(\gamma)2} - \frac{l_\gamma^2}{4})T_{(02)}^{(\beta\gamma)}$$

Using Eqs. (68)-(71), the surface-averaged temperatures $(\bar{T}_2^+)^{(\beta\gamma)}, (\bar{T}_2^-)^{(\beta\gamma)}, (\bar{T}_3^+)^{(\beta\gamma)}, (\bar{T}_3^-)^{(\beta\gamma)}$ are expressed in terms of the subcell temperature microvariables $T_{mn}^{(\beta\gamma)}$ as follows

$$
\begin{aligned}
(\bar{T}_2^+)^{(\beta\gamma)} &= T_{(00)}^{(\beta\gamma)} + \frac{h_\beta}{2} T_{(10)}^{(\beta\gamma)} + \frac{h_\beta^2}{4} T_{(20)}^{(\beta\gamma)} \\
(\bar{T}_2^-)^{(\beta\gamma)} &= T_{(00)}^{(\beta\gamma)} - \frac{h_\beta}{2} T_{(10)}^{(\beta\gamma)} + \frac{h_\beta^2}{4} T_{(20)}^{(\beta\gamma)} \\
(\bar{T}_3^+)^{(\beta\gamma)} &= T_{(00)}^{(\beta\gamma)} + \frac{l_\gamma}{2} T_{(01)}^{(\beta\gamma)} + \frac{l_\gamma^2}{4} T_{(02)}^{(\beta\gamma)} \\
(\bar{T}_3^-)^{(\beta\gamma)} &= T_{(00)}^{(\beta\gamma)} - \frac{l_\gamma}{2} T_{(01)}^{(\beta\gamma)} + \frac{l_\gamma^2}{4} T_{(02)}^{(\beta\gamma)}
\end{aligned}
$$

Adding and subtracting the above first two equations involving $(\bar{T}_2^+)^{(\beta\gamma)}$ and $(\bar{T}_2^-)^{(\beta\gamma)}$, we obtain expressions for $T_{(10)}^{(\beta\gamma)}$ and $T_{(20)}^{(\beta\gamma)}$ in terms of $(\bar{T}_2^+)^{(\beta\gamma)}$, $(\bar{T}_2^-)^{(\beta\gamma)}$ and $T_{(00)}^{(\beta\gamma)}$. The matrix form of these two expressions become

$$
\begin{bmatrix} T_{(10)} \\ T_{(20)} \end{bmatrix}^{(\beta\gamma)} = \begin{bmatrix} -\dfrac{1}{h_\beta} & \dfrac{1}{h_\beta} \\ \dfrac{2}{h_\beta^2} & \dfrac{2}{h_\beta^2} \end{bmatrix} \begin{bmatrix} \bar{T}_2^- \\ \bar{T}_2^+ \end{bmatrix}^{(\beta\gamma)} - \frac{4}{h_\beta^2} \begin{bmatrix} 0 \\ 1 \end{bmatrix} T_{(00)}^{(\beta\gamma)} \tag{78}
$$

Similarly, $T_{(01)}^{(\beta\gamma)}$ and $T_{(02)}^{(\beta\gamma)}$ can be expressed in terms of $(\bar{T}_3^-)^{(\beta\gamma)}, (\bar{T}_3^+)^{(\beta\gamma)}$ and $T_{(00)}^{(\beta\gamma)}$ by applying the same technique to the above last two equations,

$$
\begin{bmatrix} T_{(01)} \\ T_{(02)} \end{bmatrix}^{(\beta\gamma)} = \begin{bmatrix} -\dfrac{1}{l_\gamma} & \dfrac{1}{l_\gamma} \\ \dfrac{2}{l_\gamma^2} & \dfrac{2}{l_\gamma^2} \end{bmatrix} \begin{bmatrix} \bar{T}_3^- \\ \bar{T}_3^+ \end{bmatrix}^{(\beta\gamma)} - \frac{4}{l_\gamma^2} \begin{bmatrix} 0 \\ 1 \end{bmatrix} T_{(00)}^{(\beta\gamma)} \tag{79}
$$

The next step is to evaluate the surface-averaged heat flux components in terms of the microvariables $T_{(mn)}^{(\beta\gamma)}$. Integrating Eqs. (64)-(67) with $k_2^{(\beta\gamma)}$ and $k_3^{(\beta\gamma)}$ given by Eqs. (76) and (77), the surface-averaged heat fluxes $(\bar{Q}_2^+)^{(\beta\gamma)}, (\bar{Q}_2^-)^{(\beta\gamma)}, (\bar{Q}_3^+)^{(\beta\gamma)}, (\bar{Q}_3^-)^{(\beta\gamma)}$ are obtained in terms of the temperature microvariables $T_{(mn)}^{(\beta\gamma)}$ as follows

$$
\begin{aligned}
(\bar{Q}_2^+)^{(\beta\gamma)} &= T_{(10)}^{(\beta\gamma)}(-k_{20}^{(\beta\gamma)} - \frac{h_\beta}{2} k_{22}^{(\beta\gamma)}) + T_{(20)}^{(\beta\gamma)}(\frac{-3h_\beta}{2} k_{20}^{(\beta\gamma)} - \frac{3h_\beta^2}{4} k_{22}^{(\beta\gamma)}) \\
(\bar{Q}_2^-)^{(\beta\gamma)} &= T_{(10)}^{(\beta\gamma)}(-k_{20}^{(\beta\gamma)} + \frac{h_\beta}{2} k_{22}^{(\beta\gamma)}) + T_{(20)}^{(\beta\gamma)}(\frac{3h_\beta}{2} k_{20}^{(\beta\gamma)} - \frac{3h_\beta^2}{4} k_{22}^{(\beta\gamma)}) \\
(\bar{Q}_3^+)^{(\beta\gamma)} &= T_{(01)}^{(\beta\gamma)}(-k_{30}^{(\beta\gamma)} - \frac{l_\gamma}{2} k_{33}^{(\beta\gamma)}) + T_{(02)}^{(\beta\gamma)}(\frac{-3l_\gamma}{2} k_{30}^{(\beta\gamma)} - \frac{3l_\gamma^2}{4} k_{33}^{(\beta\gamma)}) \\
(\bar{Q}_3^-)^{(\beta\gamma)} &= T_{(01)}^{(\beta\gamma)}(-k_{30}^{(\beta\gamma)} + \frac{l_\gamma}{2} k_{33}^{(\beta\gamma)}) + T_{(02)}^{(\beta\gamma)}(\frac{3l_\gamma}{2} k_{30}^{(\beta\gamma)} - \frac{3l_\gamma^2}{4} k_{33}^{(\beta\gamma)})
\end{aligned}
$$

The above four equations can be rewritten in matrix form as follows

$$
\begin{bmatrix} -\bar{Q}_2^- \\ \bar{Q}_2^+ \end{bmatrix}^{(\beta\gamma)} = \begin{bmatrix} k_{20} - k_{22}\dfrac{h_\beta}{2} & -\dfrac{3h_\beta k_{20}}{2} + \dfrac{3h_\beta^2}{4} k_{22} \\ -k_{20} - k_{22}\dfrac{h_\beta}{2} & -\dfrac{3h_\beta k_{20}}{2} - \dfrac{3h_\beta^2}{4} k_{22} \end{bmatrix}^{(\beta\gamma)} \begin{bmatrix} T_{(10)} \\ T_{(20)} \end{bmatrix}^{(\beta\gamma)} \tag{80}
$$

and

$$\left[\begin{array}{c} -\bar{Q}_3^- \\ \bar{Q}_3^+ \end{array}\right]^{(\beta\gamma)} = \left[\begin{array}{cc} k_{30} - k_{33}\dfrac{l_\gamma}{2} & -\dfrac{3l_\gamma k_{30}}{2} + \dfrac{3l_\gamma^2}{4}k_{33} \\ -k_{30} - k_{33}\dfrac{l_\gamma}{2} & -\dfrac{3l_\gamma k_{30}}{2} - \dfrac{3l_\gamma^2}{4}k_{33} \end{array}\right]^{(\beta\gamma)} \left[\begin{array}{c} T_{(01)} \\ T_{(02)} \end{array}\right]^{(\beta\gamma)} \tag{81}$$

Substituting for $T_{(10)}^{(\beta\gamma)}, T_{(20)}^{(\beta\gamma)}$ and $T_{(01)}^{(\beta\gamma)}, T_{(02)}^{(\beta\gamma)}$ using Eqs. (78) and (79), the above equations become

$$\left[\begin{array}{c} -\bar{Q}_2^- \\ \bar{Q}_2^+ \end{array}\right]^{(\beta\gamma)} = \left[\begin{array}{cc} 2k_{22} - \dfrac{4k_{20}}{h_\beta} & k_{22} - \dfrac{2k_{20}}{h_\beta} \\ -k_{22} - \dfrac{2k_{20}}{h_\beta} & -2k_{22} - \dfrac{4k_{20}}{h_\beta} \end{array}\right]^{(\beta\gamma)} \left[\begin{array}{c} \bar{T}_2^- \\ \bar{T}_2^+ \end{array}\right]^{(\beta\gamma)} + \left[\begin{array}{c} \dfrac{6k_{20}}{h_\beta} - 3k_{22} \\ \dfrac{6k_{20}}{h_\beta} + 3k_{22} \end{array}\right]^{(\beta\gamma)} T_{(00)}^{(\beta\gamma)} \tag{82}$$

and

$$\left[\begin{array}{c} -\bar{Q}_3^- \\ \bar{Q}_3^+ \end{array}\right]^{(\beta\gamma)} = \left[\begin{array}{cc} 2k_{33} - \dfrac{4k_{30}}{l_\gamma} & k_{33} - \dfrac{4k_{30}}{l_\gamma} \\ -k_{33} - \dfrac{4k_{30}}{l_\gamma} & -2k_{33} - \dfrac{4k_{30}}{l_\gamma} \end{array}\right]^{(\beta\gamma)} \left[\begin{array}{c} \bar{T}_3^- \\ \bar{T}_3^+ \end{array}\right]^{(\beta\gamma)} + \left[\begin{array}{c} \dfrac{6k_{30}}{l_\gamma} - 3k_{33} \\ \dfrac{6k_{30}}{l_\gamma} - 3k_{33} \end{array}\right]^{(\beta\gamma)} T_{(00)}^{(\beta\gamma)} \tag{83}$$

The last step is to develop a relationship between the surface-averaged temperatures and the volume-averaged temperature $T_{(00)}^{(\beta\gamma)}$. This relationship is obtained from the volume-averaged heat conduction equation

$$\int_{-l_\gamma/2}^{l_\gamma/2}\int_{-h_\beta/2}^{h_\beta/2} \left(\frac{\partial q_2^{(\beta\gamma)}}{\partial \bar{x}_2^{(\beta)}} + \frac{\partial q_3^{(\beta\gamma)}}{\partial \bar{x}_3^{(\gamma)}} \right) d\bar{x}_2^{(\beta)} d\bar{x}_3^{(\gamma)} = 0 \tag{84}$$

where $q_2^{(\beta\gamma)}$ and $q_3^{(\beta\gamma)}$ are given by Eqs. (33) and (34). Since the thermal conductivity coefficients $k_2^{(\beta\gamma)}$ and $k_3^{(\beta\gamma)}$ are functions of the coordinates $\bar{x}_2^{(\beta)}$ and $\bar{x}_3^{(\gamma)}$, the above equation can be developed by using the chain rule as

$$\int\limits_{-l_\gamma/2}^{l_\gamma/2}\int\limits_{-h_\beta/2}^{h_\beta/2} \Big(\frac{\partial k_2^{(\beta\gamma)}}{\partial \bar{x}_2^{(\beta)}} \frac{\partial T^{(\beta\gamma)}}{\partial \bar{x}_2^{(\beta)}} + \frac{\partial^2 T^{(\beta\gamma)}}{\partial \bar{x}_2^{2\,(\beta)}} k_2^{(\beta\gamma)} + \frac{\partial k_3^{(\beta\gamma)}}{\partial \bar{x}_3^{(\gamma)}} \frac{\partial T^{(\beta\gamma)}}{\partial \bar{x}_3^{(\gamma)}} + \frac{\partial^2 T^{(\beta\gamma)}}{\partial \bar{x}_3^{2\,(\gamma)}} k_3^{(\beta\gamma)} \Big) d\bar{x}_2^{(\beta)} d\bar{x}_3^{(\gamma)} = 0 \tag{85}$$

Upon determining the derivatives of temperature and thermal conductivity, respectively, the above equation becomes

$$\begin{aligned} \int\limits_{-l_\gamma/2}^{l_\gamma/2}\int\limits_{-h_\beta/2}^{h_\beta/2} & [k_{22}^{(\beta\gamma)} T_{(10)}^{(\beta\gamma)} + 3T_{(20)}^{(\beta\gamma)} (2k_{22}^{(\beta\gamma)} \bar{x}_2^{(\beta)} + k_{20}^{(\beta\gamma)}) + \\ & k_{33}^{(\beta\gamma)} T_{(01)}^{(\beta\gamma)} + 3T_{(02)}^{(\beta\gamma)} (2k_{33}^{(\beta\gamma)} \bar{x}_3^{(\gamma)} + k_{30}^{(\beta\gamma)})] d\bar{x}_2^{(\beta)} d\bar{x}_3^{(\gamma)} = 0 \end{aligned} \tag{86}$$

Substituting for ${T_{(10)}}^{(\beta\gamma)}$, ${T_{(20)}}^{(\beta\gamma)}$, and ${T_{(01)}}^{(\beta\gamma)}$, ${T_{(02)}}^{(\beta\gamma)}$ using Eqs. (78) and (79), the above equation becomes

$$\frac{k_{22}^{(\beta\gamma)}}{h_\beta}[(\bar{T}_2^+)^{(\beta\gamma)} - (\bar{T}_2^-)^{(\beta\gamma)}] + \frac{3k_{20}^{(\beta\gamma)}}{h_\beta^2}[2(\bar{T}_2^-)^{(\beta\gamma)} + 2(\bar{T}_2^+)^{(\beta\gamma)} - 4T_{(00)}^{(\beta\gamma)}] +$$
$$\frac{k_{33}^{(\beta\gamma)}}{l_\gamma}[(\bar{T}_3^+)^{(\beta\gamma)} - (\bar{T}_3^-)^{(\beta\gamma)}] + \frac{3k_{30}^{(\beta\gamma)}}{l_\gamma^2}[2(\bar{T}_3^-)^{(\beta\gamma)} + 2(\bar{T}_3^+)^{(\beta\gamma)} - 4T_{(00)}^{(\beta\gamma)}] = 0 \tag{87}$$

Therefore, the expression for $T_{(00)}^{(\beta\gamma)}$ can be obtained from the above equation in terms of $(\bar{T}_2^-)^{(\beta\gamma)}$, $(\bar{T}_2^+)^{(\beta\gamma)}$, $(\bar{T}_3^-)^{(\beta\gamma)}$, $(\bar{T}_3^+)^{(\beta\gamma)}$ as follows

$$T_{(00)}^{(\beta\gamma)} = [(\bar{T}_2^-)^{(\beta\gamma)}(\frac{6k_{20}^{(\beta\gamma)}}{h_\beta^2} - \frac{k_{22}^{(\beta\gamma)}}{h_\beta}) + (\bar{T}_2^+)^{(\beta\gamma)}(\frac{k_{22}^{(\beta\gamma)}}{h_\beta} + \frac{6k_{20}^{(\beta\gamma)}}{h_\beta^2}) +$$
$$(\bar{T}_3^-)^{(\beta\gamma)}(\frac{6k_{30}^{(\beta\gamma)}}{l_\gamma^2} - \frac{k_{33}^{(\beta\gamma)}}{l_\gamma}) + (\bar{T}_3^+)^{(\beta\gamma)}(\frac{k_{33}^{(\beta\gamma)}}{l_\gamma} + \frac{6k_{30}^{(\beta\gamma)}}{l_\gamma^2})]/12(\frac{k_{20}^{(\beta\gamma)}}{h_\beta^2} + \frac{k_{30}^{(\beta\gamma)}}{l_\gamma^2}) \tag{88}$$

Upon substituting the above expression for $T_{(00)}^{(\beta\gamma)}$ into the expressions for $(\bar{Q}_2^+)^{(\beta\gamma)}$, $(\bar{Q}_2^-)^{(\beta\gamma)}$, $(\bar{Q}_3^+)^{(\beta\gamma)}$, $(\bar{Q}_3^-)^{(\beta\gamma)}$ given by Eqs. (82) and (83), the local conductivity matrix $\boldsymbol{\kappa}^{(\beta\gamma)}$ is obtained which directly relates the surface-averaged heat fluxes to the corresponding surface-averaged temperatures. These expressions can be written in matrix form as follows

$$\begin{bmatrix} -\bar{Q}_2^- \\ \bar{Q}_2^+ \\ -\bar{Q}_3^- \\ \bar{Q}_3^+ \end{bmatrix}^{(\beta\gamma)} = \begin{bmatrix} \kappa_{11} & \kappa_{12} & \kappa_{13} & \kappa_{14} \\ \kappa_{21} & \kappa_{22} & \kappa_{23} & \kappa_{24} \\ \kappa_{31} & \kappa_{32} & \kappa_{33} & \kappa_{34} \\ \kappa_{41} & \kappa_{42} & \kappa_{43} & \kappa_{44} \end{bmatrix}^{(\beta\gamma)} \begin{bmatrix} \bar{T}_2^- \\ \bar{T}_2^+ \\ \bar{T}_3^- \\ \bar{T}_3^+ \end{bmatrix}^{(\beta\gamma)} \tag{89}$$

with the individual local conductivity matrix elements given below in terms of the subcell thermal conductivity coefficients and geometry, upon setting $\lambda = 12(k_{20}^{(\beta\gamma)}/h_\beta^2 + k_{30}^{(\beta\gamma)}/l_\gamma^2)$ for convenience.

$$\kappa_{11}^{(\beta\gamma)} = 2k_{22}^{(\beta\gamma)} - \frac{4k_{20}^{(\beta\gamma)}}{h_\beta} + (\frac{6k_{20}^{(\beta\gamma)}}{h_\beta} - 3k_{22}^{(\beta\gamma)})(\frac{-k_{22}^{(\beta\gamma)}}{h_\beta} + \frac{6k_{20}^{(\beta\gamma)}}{h_\beta^2})/\lambda$$
$$\kappa_{12}^{(\beta\gamma)} = k_{22}^{(\beta\gamma)} - \frac{2k_{20}^{(\beta\gamma)}}{h_\beta} + (\frac{6k_{20}^{(\beta\gamma)}}{h_\beta} - 3k_{22}^{(\beta\gamma)})(\frac{k_{22}^{(\beta\gamma)}}{h_\beta} + \frac{6k_{20}^{(\beta\gamma)}}{h_\beta^2})/\lambda$$
$$\kappa_{13}^{(\beta\gamma)} = (\frac{6k_{20}^{(\beta\gamma)}}{h_\beta} - 3k_{22}^{(\beta\gamma)})(\frac{-k_{33}^{(\beta\gamma)}}{l_\gamma} + \frac{6k_{30}^{(\beta\gamma)}}{l_\gamma^2})/\lambda$$
$$\kappa_{14}^{(\beta\gamma)} = (\frac{6k_{20}^{(\beta\gamma)}}{h_\beta} - 3k_{22}^{(\beta\gamma)})(\frac{k_{33}^{(\beta\gamma)}}{l_\gamma} + \frac{6k_{30}^{(\beta\gamma)}}{l_\gamma^2})/\lambda$$
$$\kappa_{21}^{(\beta\gamma)} = -k_{22}^{(\beta\gamma)} - \frac{2k_{20}^{(\beta\gamma)}}{h_\beta} + (\frac{6k_{20}^{(\beta\gamma)}}{h_\beta} + 3k_{22}^{(\beta\gamma)})(\frac{-k_{22}^{(\beta\gamma)}}{h_\beta} + \frac{6k_{20}^{(\beta\gamma)}}{h_\beta^2})/\lambda$$
$$\kappa_{22}^{(\beta\gamma)} = -2k_{22}^{(\beta\gamma)} - \frac{4k_{20}^{(\beta\gamma)}}{h_\beta} + (\frac{6k_{20}^{(\beta\gamma)}}{h_\beta} + 3k_{22}^{(\beta\gamma)})(\frac{k_{22}^{(\beta\gamma)}}{h_\beta} + \frac{6k_{20}^{(\beta\gamma)}}{h_\beta^2})/\lambda$$
$$\kappa_{23}^{(\beta\gamma)} = (\frac{6k_{20}^{(\beta\gamma)}}{h_\beta} + 3k_{22}^{(\beta\gamma)})(\frac{-k_{33}^{(\beta\gamma)}}{l_\gamma} + \frac{6k_{30}^{(\beta\gamma)}}{l_\gamma^2})/\lambda$$
$$\kappa_{24}^{(\beta\gamma)} = (\frac{6k_{20}^{(\beta\gamma)}}{h_\beta} + 3k_{22}^{(\beta\gamma)})(\frac{k_{33}^{(\beta\gamma)}}{l_\gamma} + \frac{6k_{30}^{(\beta\gamma)}}{l_\gamma^2})/\lambda$$

$$\kappa_{31}^{(\beta\gamma)} = 2k_{33}^{(\beta\gamma)} - \frac{4k_{30}^{(\beta\gamma)}}{l_\gamma} + (\frac{6k_{30}^{(\beta\gamma)}}{l_\gamma} - 3k_{33}^{(\beta\gamma)})(\frac{-k_{33}^{(\beta\gamma)}}{l_\gamma} + \frac{6k_{30}^{(\beta\gamma)}}{l_\gamma^2})/\lambda$$
$$\kappa_{32}^{(\beta\gamma)} = k_{33}^{(\beta\gamma)} - \frac{2k_{30}^{(\beta\gamma)}}{l_\gamma} + (\frac{6k_{30}^{(\beta\gamma)}}{l_\gamma} - 3k_{33}^{(\beta\gamma)})(\frac{k_{33}^{(\beta\gamma)}}{l_\gamma} + \frac{6k_{30}^{(\beta\gamma)}}{l_\gamma^2})/\lambda$$
$$\kappa_{33}^{(\beta\gamma)} = (\frac{6k_{30}^{(\beta\gamma)}}{l_\gamma} - 3k_{33}^{(\beta\gamma)})(\frac{-k_{22}^{(\beta\gamma)}}{h_\beta} + \frac{6k_{20}^{(\beta\gamma)}}{h_\beta^2})/\lambda$$
$$\kappa_{34}^{(\beta\gamma)} = (\frac{6k_{30}^{(\beta\gamma)}}{l_\gamma} - 3k_{33}^{(\beta\gamma)})(\frac{k_{22}^{(\beta\gamma)}}{h_\beta} + \frac{6k_{20}^{(\beta\gamma)}}{h_\beta^2})/\lambda$$
$$\kappa_{41}^{(\beta\gamma)} = -k_{33}^{(\beta\gamma)} - \frac{2k_{30}^{(\beta\gamma)}}{l_\gamma} + (\frac{6k_{30}^{(\beta\gamma)}}{l_\gamma} + 3k_{33}^{(\beta\gamma)})(\frac{-k_{33}^{(\beta\gamma)}}{l_\gamma} + \frac{6k_{30}^{(\beta\gamma)}}{l_\gamma^2})/\lambda$$
$$\kappa_{42}^{(\beta\gamma)} = -2k_{33}^{(\beta\gamma)} - \frac{4k_{30}^{(\beta\gamma)}}{l_\gamma} + (\frac{6k_{30}^{(\beta\gamma)}}{l_\gamma} + 3k_{33}^{(\beta\gamma)})(\frac{k_{33}^{(\beta\gamma)}}{l_\gamma} + \frac{6k_{30}^{(\beta\gamma)}}{l_\gamma^2})/\lambda$$
$$\kappa_{43}^{(\beta\gamma)} = (\frac{6k_{30}^{(\beta\gamma)}}{l_\gamma} + 3k_{33}^{(\beta\gamma)})(\frac{-k_{22}^{(\beta\gamma)}}{h_\beta} + \frac{6k_{20}^{(\beta\gamma)}}{h_\beta^2})/\lambda$$
$$\kappa_{44}^{(\beta\gamma)} = (\frac{6k_{30}^{(\beta\gamma)}}{l_\gamma} + 3k_{33}^{(\beta\gamma)})(\frac{k_{22}^{(\beta\gamma)}}{h_\beta} + \frac{6k_{20}^{(\beta\gamma)}}{h_\beta^2})/\lambda$$

3.2 Constant Thermal Conductivity

When the coefficients associated with the local coordinates $\bar{x}_2^{(\beta)}$ and $\bar{x}_3^{(\gamma)}$ in the expressions for $k_2^{(\beta\gamma)}$ and $k_3^{(\beta\gamma)}$ are set to zero, i.e., let $k_{22}^{(\beta\gamma)} = k_{23}^{(\beta\gamma)} = k_{32}^{(\beta\gamma)} = k_{33}^{(\beta\gamma)} = 0$ in Eqs. (76) and (77), constant thermal conductivities are obtained, i.e., $k_2^{(\beta\gamma)} = k_{20}^{(\beta\gamma)}$ and $k_3^{(\beta\gamma)} = k_{30}^{(\beta\gamma)}$.

Replacing $k_{20}^{(\beta\gamma)}$ with $k_2^{(\beta\gamma)}$, $k_{30}^{(\beta\gamma)}$ with $k_3^{(\beta\gamma)}$and letting $k_{22}^{(\beta\gamma)} = k_{33}^{(\beta\gamma)} = 0$ in the local conductivity matrix $\boldsymbol{\kappa}^{(\beta\gamma)}$ with variable thermal conductivity in Eq. (89), the new local conductivity matrix with constant thermal conductivities is obtained.

$$\begin{bmatrix} -\bar{Q}_2^- \\ \bar{Q}_2^+ \\ -\bar{Q}_3^- \\ \bar{Q}_3^+ \end{bmatrix}^{(\beta\gamma)} = \begin{bmatrix} \kappa_{11} & \kappa_{12} & \kappa_{13} & \kappa_{14} \\ \kappa_{21} & \kappa_{22} & \kappa_{23} & \kappa_{24} \\ \kappa_{31} & \kappa_{32} & \kappa_{33} & \kappa_{34} \\ \kappa_{41} & \kappa_{42} & \kappa_{43} & \kappa_{44} \end{bmatrix}^{(\beta\gamma)} \begin{bmatrix} \bar{T}_2^- \\ \bar{T}_2^+ \\ \bar{T}_3^- \\ \bar{T}_3^+ \end{bmatrix}^{(\beta\gamma)} \tag{90}$$

where

$$\kappa_{11}^{(\beta\gamma)} = \kappa_{22}^{(\beta\gamma)} = \frac{-2k_2^{(\beta\gamma)}}{h_\beta}(2 - \frac{k_2^{(\beta\gamma)}}{2\bar{k}_2^{(\beta\gamma)}})$$
$$\kappa_{12}^{(\beta\gamma)} = \kappa_{21}^{(\beta\gamma)} = \frac{-2k_2^{(\beta\gamma)}}{h_\beta}(1 - \frac{k_2^{(\beta\gamma)}}{2\bar{k}_2^{(\beta\gamma)}})$$
$$\kappa_{13}^{(\beta\gamma)} = \kappa_{14}^{(\beta\gamma)} = \kappa_{23}^{(\beta\gamma)} = \kappa_{24}^{(\beta\gamma)} = \frac{k_2^{(\beta\gamma)} k_3^{(\beta\gamma)} h_\beta}{\bar{k}_2^{(\beta\gamma)} l_\gamma^2}$$
$$\kappa_{31}^{(\beta\gamma)} = \kappa_{32}^{(\beta\gamma)} = \kappa_{41}^{(\beta\gamma)} = \kappa_{42}^{(\beta\gamma)} = \frac{k_2^{(\beta\gamma)} k_3^{(\beta\gamma)} l_\gamma}{\bar{k}_2^{(\beta\gamma)} h_\beta^2}$$
$$\kappa_{33}^{(\beta\gamma)} = \kappa_{44}^{(\beta\gamma)} = \frac{-2k_3^{(\beta\gamma)}}{l_\gamma}(2 - \frac{k_3^{(\beta\gamma)}}{2\bar{k}_3^{(\beta\gamma)}})$$

$$\kappa_{34}^{(\beta\gamma)} = \kappa_{43}^{(\beta\gamma)} = \frac{-2k_3^{(\beta\gamma)}}{l_\gamma}(1 - \frac{k_3^{(\beta\gamma)}}{2\bar{k}_3^{(\beta\gamma)}})$$

and where

$$\bar{k}_2^{(\beta\gamma)} = h_\beta^2(\frac{k_2^{(\beta\gamma)}}{h_\beta^2} + \frac{k_3^{(\beta\gamma)}}{l_\gamma^2})/3$$
$$\bar{k}_3^{(\beta\gamma)} = l_\gamma^2(\frac{k_2^{(\beta\gamma)}}{h_\beta^2} + \frac{k_3^{(\beta\gamma)}}{l_\gamma^2})/3$$

This is the same local conductivity matrix as that obtained by Bansal (2002), which confirms that the present development reduces correctly.

3.3 Global Conductivity Matrix Assembly

As mentioned above, the assembly of the global conductivity matrix is carried out by applying heat flux continuity conditions, Eq. (72) and (73), at each interface along x_2 and x_3 directions, respectively, together with the temperature continuity condition defined by Eqs. (74) and (75), starting at the boundary with prescribed boundary conditions.

3.3.1 Temperature continuity conditions

From the temperature continuity, we know that the surface-averaged temperature $(\bar{T}_2^+)^{(\beta\gamma)}$ of the (β, γ) subcell is the same as $(\bar{T}_2^-)^{(\beta+1,\gamma)}$ of the $(\beta+1, \gamma)$ subcell defined in Eq. (74). The same holds true in the x_3 direction, Eq. (75). These conditions are applied $\beta = 1, ..., N_\beta - 1$ and $\gamma = 1, ..., N_\gamma - 1$ times at the subcell interfaces in the x_2 and x_3 directions, respectively, in the heat flux continuity conditions described below. Thus, altogether, the number of unknown surface-averaged interfacial temperatures in the interior is $(N_\beta - 1)N_\gamma + (N_\gamma - 1)N_\beta$.

3.3.2 Heat flux continuity conditions

The continuity of interfacial surfaced-averaged heat flux along each interface requires that the sum of the heat fluxes across the interfaces separating adjacent subcells be zero, i.e., Eq. (72) in the x_2 direction and Eq. (73) in the x_3 direction, respectively. Expressing these two equations in terms of the surface-averaged temperatures by using Eq. (63) yields for the interface between (β, γ) and $(\beta + 1, \gamma)$ subcells,

$$\kappa_{21}^{(\beta,\gamma)}(\bar{T}_2^-)^{(\beta\gamma)} + \kappa_{22}^{(\beta,\gamma)}(\bar{T}_2^+)^{(\beta\gamma)} + \kappa_{23}^{(\beta,\gamma)}(\bar{T}_3^-)^{(\beta\gamma)} + \kappa_{24}^{(\beta,\gamma)}(\bar{T}_3^+)^{(\beta\gamma)} + \kappa_{11}^{(\beta+1,\gamma)}(\bar{T}_2^-)^{(\beta+1,\gamma)}$$
$$+\kappa_{12}^{(\beta+1,\gamma)}(\bar{T}_2^+)^{(\beta+1,\gamma)} + \kappa_{13}^{(\beta+1,\gamma)}(\bar{T}_3^-)^{(\beta+1,\gamma)} + \kappa_{14}^{(\beta+1,\gamma)}(\bar{T}_3^+)^{(\beta+1,\gamma)} = 0 \quad (91)$$

while for the interface between (β, γ) and $(\beta, \gamma + 1)$ subcells we get,

$$\kappa_{41}^{(\beta,\gamma)}(\bar{T}_2^-)^{(\beta\gamma)} + \kappa_{42}^{(\beta,\gamma)}(\bar{T}_2^+)^{(\beta\gamma)} + \kappa_{43}^{(\beta,\gamma)}(\bar{T}_3^-)^{(\beta\gamma)} + \kappa_{44}^{(\beta,\gamma)}(\bar{T}_3^+)^{(\beta\gamma)} + \kappa_{31}^{(\beta,\gamma+1)}(\bar{T}_2^-)^{(\beta,\gamma+1)}$$
$$+\kappa_{32}^{(\beta,\gamma+1)}(\bar{T}_2^+)^{(\beta,\gamma+1)} + \kappa_{33}^{(\beta,\gamma+1)}(\bar{T}_3^-)^{(\beta,\gamma+1)} + \kappa_{34}^{(\beta,\gamma+1)}(\bar{T}_3^+)^{(\beta,\gamma+1)} = 0 \quad (92)$$

Employing the temperature continuity conditions, Eqs. (74) and (75), the above equations become

$$\kappa_{21}^{(\beta,\gamma)}\bar{T}_2^{(\beta,\gamma)} + (\kappa_{22}^{(\beta,\gamma)} + \kappa_{11}^{(\beta+1,\gamma)})\bar{T}_2^{(\beta+1,\gamma)} + \kappa_{12}^{(\beta+1,\gamma)}\bar{T}_2^{(\beta+2,\gamma)} + \kappa_{23}^{(\beta,\gamma)}\bar{T}_3^{(\beta,\gamma)} \quad (93)$$
$$+\kappa_{24}^{(\beta,\gamma)}\bar{T}_3^{(\beta,\gamma+1)} + \kappa_{13}^{(\beta+1,\gamma)}\bar{T}_3^{(\beta+1,\gamma)} + \kappa_{14}^{(\beta+1,\gamma)}\bar{T}_3^{(\beta+1,\gamma+1)} = 0$$

$$\kappa_{41}^{(\beta,\gamma)}\bar{T}_2^{(\beta,\gamma)} + \kappa_{42}^{(\beta,\gamma)}\bar{T}_2^{(\beta+1,\gamma)} + \kappa_{31}^{(\beta,\gamma+1)}\bar{T}_2^{(\beta,\gamma+1)} + \kappa_{32}^{(\beta,\gamma+1)}\bar{T}_2^{(\beta+1,\gamma+1)} + \kappa_{43}^{(\beta,\gamma)}\bar{T}_3^{(\beta,\gamma)}$$
$$+(\kappa_{44}^{(\beta,\gamma)} + \kappa_{33}^{(\beta,\gamma+1)})\bar{T}_3^{(\beta,\gamma+1)} + \kappa_{34}^{(\beta,\gamma+1)}\bar{T}_3^{(\beta,\gamma+2)} = 0 \qquad (94)$$

Thus, these two equations provide us with $(N_\beta - 1)N_\gamma + (N_\gamma - 1)N_\beta$ equations for the unknown $(N_\beta - 1)N_\gamma + (N_\gamma - 1)N_\beta$ common interfacial surface-averaged temperatures.

3.3.3 Boundary conditions

At external boundaries, the remaining $2(N_\beta + N_\gamma)$ equations are obtained from the imposed boundary conditions specified either in terms of applied temperature or heat flux as given below

$$\bar{T}_3^{(\beta,1)} \mid_{\bar{x}_3=-l_1/2} \; = \frac{1}{h_\beta}\int_{-h_\beta/2}^{h_\beta/2} T_{bot}^{(\beta)} d\bar{x}_2^{(\beta)} \qquad (95)$$

or

$$\bar{Q}_3^{(\beta,1)} \mid_{\bar{x}_3=-l_1/2} \; = \frac{1}{h_\beta}\int_{-h_\beta/2}^{h_\beta/2} q_{bot}^{(\beta)} d\bar{x}_2^{(\beta)} \qquad (96)$$

and

$$\bar{T}_3^{(\beta,N_\gamma)} \mid_{\bar{x}_3=l_{N_\gamma}/2} \; = \frac{1}{h_\beta}\int_{-h_\beta/2}^{h_\beta/2} T_{top}^{(\beta)} d\bar{x}_2^{(\beta)} \qquad (97)$$

or

$$\bar{Q}_3^{(\beta,N_\gamma)} \mid_{\bar{x}_3=l_{N_\gamma}/2} \; = \frac{1}{h_\beta}\int_{-h_\beta/2}^{h_\beta/2} q_{top}^{(\beta)} d\bar{x}_2^{(\beta)} \qquad (98)$$

at $(\beta, 1)$ and (β, N_γ) subcells. Similar reasoning holds for subcells $(1, \gamma)$, and (N_β, γ) where the applied boundary conditions are given by

$$\bar{T}_2^{(1,\gamma)} \mid_{\bar{x}_2=-h_1/2} \; = \frac{1}{l_\gamma}\int_{-l_\gamma/2}^{l_\gamma/2} T_{left}^{(\gamma)} d\bar{x}_3^{(\gamma)} \qquad (99)$$

or

$$\bar{Q}_2^{(1,\gamma)} \mid_{\bar{x}_2=-h_1/2} \; = \frac{1}{l_\gamma}\int_{-l_\gamma/2}^{l_\gamma/2} q_{left}^{(\gamma)} d\bar{x}_3^{(\gamma)} \qquad (100)$$

and

$$\bar{T}_2^{(N_\beta,\gamma)} \mid_{\bar{x}_2=h_{N_\beta}/2} \; = \frac{1}{l_\gamma}\int_{-l_\gamma/2}^{l_\gamma/2} T_{right}^{(\gamma)} d\bar{x}_3^{(\gamma)} \qquad (101)$$

or

$$\bar{Q}_2^{(N_\beta,\gamma)} \mid_{\bar{x}_2=h_{N_\beta}/2} \; = \frac{1}{l_\gamma}\int_{-l_\gamma/2}^{l_\gamma/2} q_{right}^{(\gamma)} d\bar{x}_3^{(\gamma)} \qquad (102)$$

3.3.4 Governing equations

The general form of the final system of equations can be written symbolically as

$$\mathbf{Q} = \hat{\boldsymbol{\kappa}}\mathbf{T} \qquad (103)$$

which can be decomposed for convenience as follows

$$\begin{bmatrix} \bar{\mathbf{Q}}_2 \\ \bar{\mathbf{Q}}_3 \end{bmatrix} = \begin{bmatrix} \hat{\boldsymbol{\kappa}}_{11} & \hat{\boldsymbol{\kappa}}_{12} \\ \hat{\boldsymbol{\kappa}}_{21} & \hat{\boldsymbol{\kappa}}_{22} \end{bmatrix} \begin{bmatrix} \bar{\mathbf{T}}_2 \\ \bar{\mathbf{T}}_3 \end{bmatrix} \qquad (104)$$

where the heat flux vectors $\bar{\mathbf{Q}}_2$ and $\bar{\mathbf{Q}}_3$ are defined as

$$\begin{array}{l} \bar{\mathbf{Q}}_2 = [\bar{\mathbf{Q}}_2^{(1)}, ..., \bar{\mathbf{Q}}_2^{(\gamma)}, ..., \bar{\mathbf{Q}}_2^{(N_\gamma)}] \\ \bar{\mathbf{Q}}_3 = [\bar{\mathbf{Q}}_3^{(1)}, ..., \bar{\mathbf{Q}}_3^{(\beta)}, ..., \bar{\mathbf{Q}}_3^{(N_\beta)}] \end{array} \tag{105}$$

where

$$\begin{array}{l} \bar{\mathbf{Q}}_2^{(\gamma)} = [\bar{Q}_2^{(1,\gamma)},\ 0, ..., 0,\ \bar{Q}_2^{(N_\beta+1,\gamma)}] \\ \bar{\mathbf{Q}}_3^{(\beta)} = [\bar{Q}_3^{(\beta,1)},\ 0, ..., 0,\ \bar{Q}_3^{(\beta,N_\gamma+1)}] \end{array}$$

The vectors $\bar{\mathbf{T}}_2$ and $\bar{\mathbf{T}}_3$ contain the unknown surface-averaged temperatures at the subcell interfaces and the outer edges of the composite and are given by

$$\begin{array}{l} \bar{\mathbf{T}}_2 = [\bar{\mathbf{T}}_2^{(1)}, ..., \bar{\mathbf{T}}_2^{(\gamma)}, ..., \bar{\mathbf{T}}_2^{(N_\gamma)}] \\ \bar{\mathbf{T}}_3 = [\bar{\mathbf{T}}_3^{(1)}, ..., \bar{\mathbf{T}}_3^{(\beta)}, ..., \bar{\mathbf{T}}_3^{(N_\beta)}] \end{array} \tag{106}$$

where

$$\begin{array}{l} \bar{\mathbf{T}}_2^{(\gamma)} = [\bar{T}_2^{(1,\gamma)}, ..., \bar{T}_2^{(N_\beta+1,\gamma)}] \\ \bar{\mathbf{T}}_3^{(\beta)} = [\bar{T}_3^{(\beta,1)}, ..., \bar{T}_3^{(\beta,N_\gamma+1)}] \end{array}$$

The global thermal conductivity matrix $\hat{\boldsymbol{\kappa}}$ is obtained by assembling the local conductivity matrices as explained above. It contains information on the geometry and thermal conductivities of the individual $N_\beta N_\gamma$ subcells. The general structure of the global conductivity submatrices $\hat{\boldsymbol{\kappa}}_{11}, \hat{\boldsymbol{\kappa}}_{12}, \hat{\boldsymbol{\kappa}}_{21}, \hat{\boldsymbol{\kappa}}_{22}$ is given below

$$\hat{\boldsymbol{\kappa}}_{11} = \begin{bmatrix} \mathbf{A}_{\vec{\beta}}^{(1)} & \mathbf{0} & \mathbf{0} & \mathbf{0} & \mathbf{0} \\ \mathbf{0} & ..... & \mathbf{0} & \mathbf{0} & \mathbf{0} \\ \mathbf{0} & \mathbf{0} & \mathbf{A}_{\vec{\beta}}^{(\gamma)} & \mathbf{0} & \mathbf{0} \\ \mathbf{0} & \mathbf{0} & \mathbf{0} & ..... & \mathbf{0} \\ \mathbf{0} & \mathbf{0} & \mathbf{0} & \mathbf{0} & \mathbf{A}_{\vec{\beta}}^{(N_\gamma)} \end{bmatrix} \quad \hat{\boldsymbol{\kappa}}_{12} = \begin{bmatrix} \mathbf{B}_{\vec{\beta}}^{(1,1)} & \mathbf{B}_{\vec{\beta}}^{(2,1)} & ..... & \mathbf{B}_{\vec{\beta}}^{(N_\beta,1)} \\ \mathbf{B}_{\vec{\beta}}^{(1,2)} & \mathbf{B}_{\vec{\beta}}^{(2,2)} & ..... & \mathbf{B}_{\vec{\beta}}^{(N_\beta,2)} \\ ..... & ..... & ..... & ..... \\ ..... & ..... & ..... & ..... \\ \mathbf{B}_{\vec{\beta}}^{(1,N_\gamma)} & \mathbf{B}_{\vec{\beta}}^{(2,N_\gamma)} & ..... & \mathbf{B}_{\vec{\beta}}^{(N_\beta,N_\gamma)} \end{bmatrix}$$

$$\hat{\boldsymbol{\kappa}}_{21} = \begin{bmatrix} \mathbf{B}_{\vec{\gamma}}^{(1,1)} & \mathbf{B}_{\vec{\gamma}}^{(1,2)} & ..... & \mathbf{B}_{\vec{\gamma}}^{(1,N_\gamma)} \\ \mathbf{B}_{\vec{\gamma}}^{(2,1)} & \mathbf{B}_{\vec{\gamma}}^{(2,2)} & ..... & \mathbf{B}_{\vec{\gamma}}^{(2,N_\gamma)} \\ ..... & ..... & ..... & ..... \\ ..... & ..... & ..... & ..... \\ \mathbf{B}_{\vec{\gamma}}^{(N_\beta,1)} & \mathbf{B}_{\vec{\gamma}}^{(N_\beta,2)} & ..... & \mathbf{B}_{\vec{\gamma}}^{(N_\beta,N_\gamma)} \end{bmatrix} \quad \hat{\boldsymbol{\kappa}}_{22} = \begin{bmatrix} \mathbf{A}_{\vec{\gamma}}^{(1)} & \mathbf{0} & \mathbf{0} & \mathbf{0} & \mathbf{0} \\ \mathbf{0} & ..... & \mathbf{0} & \mathbf{0} & \mathbf{0} \\ \mathbf{0} & \mathbf{0} & \mathbf{A}_{\vec{\gamma}}^{(\beta)} & \mathbf{0} & \mathbf{0} \\ \mathbf{0} & \mathbf{0} & \mathbf{0} & ..... & \mathbf{0} \\ \mathbf{0} & \mathbf{0} & \mathbf{0} & \mathbf{0} & \mathbf{A}_{\vec{\gamma}}^{(N_\beta)} \end{bmatrix}$$

The elements of the submatrices $\mathbf{A}_{\vec{\beta}}^{(\gamma)}$, $\mathbf{A}_{\vec{\gamma}}^{(\beta)}$, $\mathbf{B}_{\vec{\beta}}^{(\beta,\gamma)}$, and $\mathbf{B}_{\vec{\gamma}}^{(\beta,\gamma)}$ are given below

$$\mathbf{A}_{\vec{\beta}}^{(\gamma)} = \begin{bmatrix} \kappa_{11}^{(1,\gamma)} & \kappa_{12}^{(1,\gamma)} & 0 & 0 & 0 & 0 & 0 & 0 \\ .... & .... & .... & 0 & 0 & 0 & 0 & 0 \\ 0 & 0 & \kappa_{11}^{(\beta,\gamma)} & \kappa_{12}^{(\beta,\gamma)} & 0 & 0 & 0 & 0 \\ 0 & 0 & \kappa_{21}^{(\beta,\gamma)} & \kappa_{22}^{(\beta,\gamma)} + \kappa_{11}^{(\beta+1,\gamma)} & \kappa_{12}^{(\beta+1,\gamma)} & 0 & 0 & 0 \\ 0 & 0 & 0 & .... & .... & .... & .... & .... \\ 0 & 0 & 0 & 0 & 0 & 0 & \kappa_{21}^{(N_\beta,\gamma)} & \kappa_{22}^{(N_\beta,\gamma)} \end{bmatrix}$$

where $\gamma = 1, 2, ...N_\gamma$.

$$
\mathbf{A}_{\vec{\gamma}}^{(\beta)} = \begin{bmatrix}
\kappa_{33}^{(\beta,1)} & \kappa_{34}^{(\beta,1)} & 0 & 0 & 0 & 0 & 0 & 0 \\
.... & .... & .... & 0 & 0 & 0 & 0 & 0 \\
0 & 0 & \kappa_{33}^{(\beta,\gamma)} & \kappa_{34}^{(\beta,\gamma)} & 0 & 0 & 0 & 0 \\
0 & 0 & \kappa_{43}^{(\beta,\gamma)} & \kappa_{44}^{(\beta,\gamma)} + \kappa_{33}^{(\beta,\gamma+1)} & \kappa_{34}^{(\beta,\gamma+1)} & 0 & 0 & 0 \\
0 & 0 & 0 & .... & .... & .... & .... & .... \\
0 & 0 & 0 & 0 & 0 & 0 & \kappa_{43}^{(\beta,N_\gamma)} & \kappa_{44}^{(\beta,N_\gamma)}
\end{bmatrix}
$$

where $\beta = 1, 2, ...N_\beta$.

$$
\mathbf{B}_{\vec{\beta}}^{(\beta,\gamma)} = \begin{array}{cc}
\boldsymbol{\gamma} \rightarrow & \begin{array}{ccccccc} \mathbf{1} & \mathbf{2} & .... & \boldsymbol{\gamma}^{th}\mathbf{col.} & (\boldsymbol{\gamma}+\mathbf{1})^{th}\mathbf{col.} & .... & \mathbf{N}_\gamma\mathbf{+1} \end{array} \\
\begin{array}{c} \boldsymbol{\beta} \downarrow \\ \mathbf{1} \\ \mathbf{2} \\ .... \\ \boldsymbol{\beta}^{th}\mathbf{row} \\ (\boldsymbol{\beta}+\mathbf{1})^{th}\mathbf{row} \\ .... \\ \mathbf{N}_\beta\mathbf{+1} \end{array} &
\begin{bmatrix}
\\
0 & 0 & .... & 0 & 0 & .... & 0 \\
0 & 0 & .... & 0 & 0 & .... & 0 \\
.... & .... & .... & .... & .... & .... & .... \\
0 & 0 & .... & \kappa_{13}^{(\beta,\gamma)} & \kappa_{14}^{(\beta,\gamma)} & .... & 0 \\
0 & 0 & .... & \kappa_{23}^{(\beta,\gamma)} & \kappa_{24}^{(\beta,\gamma)} & .... & 0 \\
.... & .... & .... & .... & .... & .... & .... \\
0 & 0 & .... & 0 & 0 & .... & 0
\end{bmatrix}
\end{array}
$$

$$
\mathbf{B}_{\vec{\gamma}}^{(\beta,\gamma)} = \begin{array}{cc}
\beta \rightarrow & \begin{array}{ccccccc} \mathbf{1} & \mathbf{2} & .... & \boldsymbol{\beta}^{th}\mathbf{col.} & (\boldsymbol{\beta}+\mathbf{1})^{th}\mathbf{col.} & .... & \mathbf{N}_\beta\mathbf{+1} \end{array} \\
\begin{array}{c} \boldsymbol{\gamma} \downarrow \\ \mathbf{1} \\ \mathbf{2} \\ .... \\ \boldsymbol{\gamma}^{th}\mathbf{row} \\ (\boldsymbol{\gamma}+\mathbf{1})^{th}\mathbf{row} \\ .... \\ \mathbf{N}_\gamma\mathbf{+1} \end{array} &
\begin{bmatrix}
\\
0 & 0 & .... & 0 & 0 & .... & 0 \\
0 & 0 & .... & 0 & 0 & .... & 0 \\
.... & .... & .... & .... & .... & .... & .... \\
0 & 0 & .... & \kappa_{31}^{(\beta,\gamma)} & \kappa_{32}^{(\beta,\gamma)} & .... & 0 \\
0 & 0 & .... & \kappa_{41}^{(\beta,\gamma)} & \kappa_{42}^{(\beta,\gamma)} & .... & 0 \\
.... & .... & .... & .... & .... & .... & .... \\
0 & 0 & .... & 0 & 0 & .... & 0
\end{bmatrix}
\end{array}
$$

3.4 Reformulated vs Unreformulated HOTFGM

The motivation for the above outlined reformulation of HOTFGM is the reduction in the number of simultaneous equations whose solution determines the temperature field in the individual subcells. The reduction is a direct result of enforcing the thermal continuity at the common subcell interfaces directly. This is possible because the fundamental unknowns in the reformulation are the surface-averaged interfacial temperatures. In the original formulation, the size of the global conductivity matrix is $5N_\beta N_\gamma \times 5N_\beta N_\gamma$, while in the reformulation version we have $(2N_\beta N_\gamma + N_\beta + N_\gamma) \times (2N_\beta N_\gamma + N_\beta + N_\gamma)$. Figure 9 compares the size of the global thermal conductivity matrices in the two versions. For discretized volumes with the same number of subcells in the two directions, $N_\beta = N_\gamma$, the reduction can be as much as about 60%.

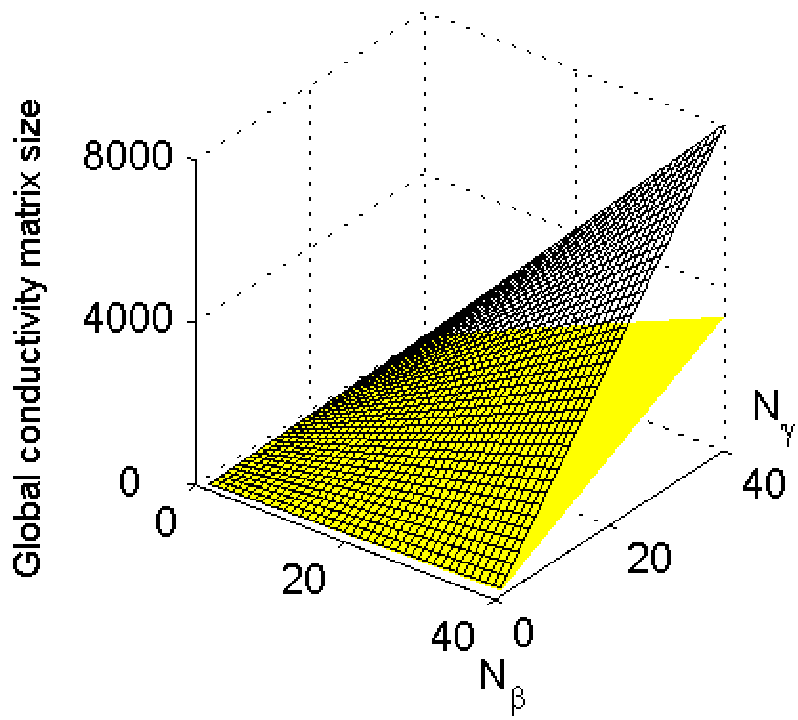

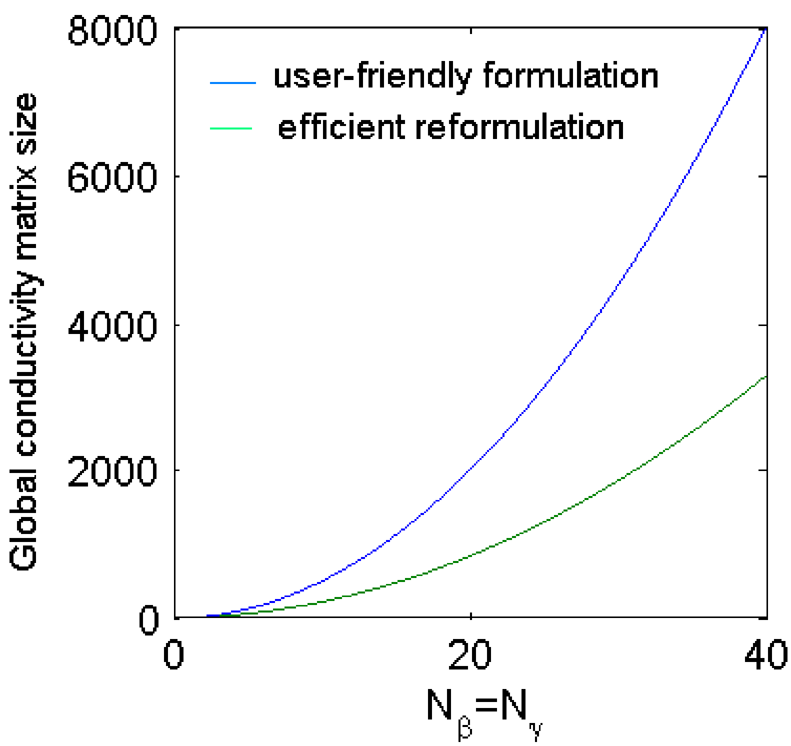

Figure 9. Reduction in the size of the global conductivity matrix due to reformulation.

4 Analytical Solution

In this section, an analytical solution methodology is developed for determining temperature distributions in homogeneous and layered plates subjected to steady-state thermal loading. The solutions will be employed in validating both the user-friendly and reformulated versions of the higher-order theory. First, we develop a solution for a single strip or plate subjected to thermal boundary conditions, and then generalize it to layered plates consisting of an arbitrary number of strips.

4.1 Single Plate/Strip Case

Consider the problem of determining the temperature distribution in a rectangular plate whose length is a and height is b in the $x_2 - x_3$ plane, Figure 10, subjected to steady-state thermal boundary conditions to be specified later. The thermal conductivity of the plate's material is constant. Therefore, the governing equation for the temperature distribution within the plate in this problem is the Laplace equation

$$\nabla^2 T = 0 \tag{107}$$

We solve this equation by the separation-of-variables method, seeking a solution of the form

$$T(x_2, x_3) = X(x_2)Y(x_3) \tag{108}$$

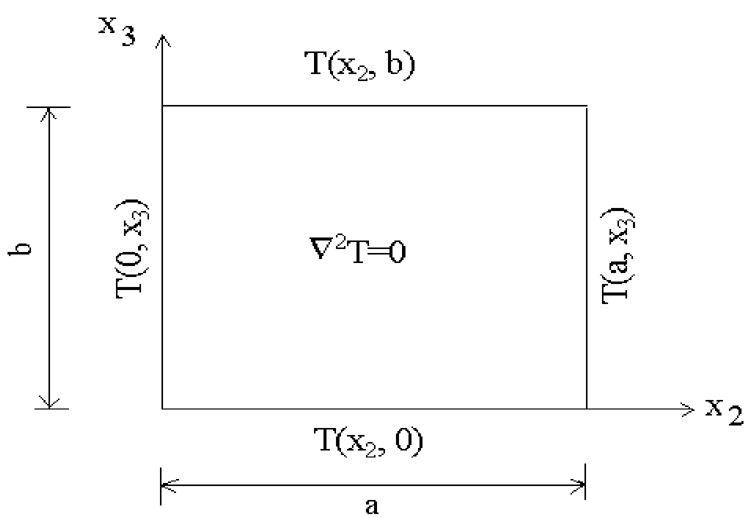

Figure 10. Problem definition.

Substituting Eq. (108) into Eq. (107) and separating the variables gives

$$\frac{X''}{X} = -\frac{Y''}{Y} = k^2 \tag{109}$$

so that

$$X'' - k^2 X = 0 \tag{110}$$

$$Y'' + k^2 Y = 0 \tag{111}$$

and

$$X(x_2) = \begin{cases} A + Bx_2, & k = 0 \\ C\cosh kx_2 + D\sinh kx_2, & k \neq 0 \end{cases} \tag{112}$$

$$Y(x_3) = \{ \begin{matrix} E + Fx_3, & k = 0 \\ G\cos kx_3 + H\sin kx_3, & k \neq 0 \end{matrix} \tag{113}$$

Because the Laplace equation $\nabla^2 T = 0$ is linear, we can use superposition and combine the $k = 0$ and $k \neq 0$ product solutions as follows

$$T(x_2, x_3) = (A + Bx_2)(E + Fx_3) + (C\cosh kx_2 + D\sinh kx_2)(G\cos kx_3 + H\sin kx_3) \tag{114}$$

The coefficients $A, ..., H$ depend on the particular boundary conditions applied at the plate's edges. We consider two cases below:

Case (i)

The first case produces an internal temperature field that has no axes of symmetry when $a \neq b$, and when $a = b$ the temperature field is symmetric about the diagonal connecting the upper left and the lower right corners. The corresponding boundary conditions are

$$\begin{aligned} T(0, x_3) &= 100, \quad T(a, x_3) = 200 \\ T(x_2, 0) &= 200, \quad T(x_2, b) = 100 \end{aligned}$$

Application of the boundary conditions at the bottom face $x_3 = 0$, where $T = 200$, yields

$$(A + Bx_2)E + (C\cosh kx_2 + D\sinh kx_2)G = 200$$

from which we obtain

$$AE = 200, B = 0, G = 0$$

Therefore Eq. (114) becomes

$$T(x_2, x_3) = 200 + Jx_3 + (C^{'}\cosh kx_2 + D^{'}\sinh kx_2)\sin kx_3 \tag{115}$$

where AF has been combined into J, CH into $C^{'}$, and DH into $D^{'}$ for convenience.

Next, application of the boundary condition at the top face $x_3 = b$, where $T = 100$, yields

$$200 + Jb + (C^{'}\cosh kx_2 + D^{'}\sinh kx_2)\sin kb = 100$$

from which we obtain

$$J = -100/b, \text{ and } \sin kb = 0$$

Hence,

$$k = m\pi/b \quad (m = 1, 2, ...)$$

Therefore, Eq.(115) becomes

$$T(x_2, x_3) = 200 - \frac{100x_3}{b} + \sum_{n=1}^{\infty}(C_m\cosh\frac{m\pi x_2}{b} + D_m\sinh\frac{m\pi x_2}{b})\sin\frac{m\pi x_3}{b} \tag{116}$$

Application of the boundary condition at the left face $x_2 = 0$, where $T = 100$, yields

$$200 - \frac{100x_3}{b} + \sum_{m=1}^{\infty} C_m \sin\frac{m\pi x_3}{b} = 100 \tag{117}$$

Solving for the unknown coefficients C_m using the orthogonality properties of $\sin\frac{m\pi x_3}{b}$, we obtain

$$C_m = \frac{2}{b}\int_0^b (\frac{100x_3}{b} - 100)\sin\frac{m\pi x_3}{b} dx_3 \tag{118}$$

or

$$C_m = -\frac{200}{m\pi} \tag{119}$$

Finally, application of the boundary condition at the right face $x_2 = a$, where $T = 200$, yields

$$200 - \frac{100x_3}{b} + \sum_{m=1}^{\infty}(-\frac{200}{m\pi}\cosh\frac{m\pi a}{b} + D_m \sinh\frac{m\pi a}{b})\sin\frac{m\pi x_3}{b} = 200 \tag{120}$$

from which the solution for D_m can be obtained in the form

$$D_m = \frac{2}{b\sinh(\frac{m\pi a}{b})}\int_0^b (\frac{100x_3}{b}\sin\frac{m\pi x_3}{b} + \frac{200}{m\pi}\cosh\frac{m\pi a}{b}\sin^2\frac{m\pi x_3}{b})dx_3 \tag{121}$$

or

$$D_m = \frac{200[\cosh(\frac{m\pi a}{b}) - \cos m\pi]}{m\pi \sinh(\frac{m\pi a}{b})} \tag{122}$$

Thus, the solution to Eq. (107) is given by Eq. (116), with the coefficients C_m and D_m computed using Eqs. (119) and (122).

Case (ii)

If the boundary conditions are changed to produce temperature distribution which is symmetric about the $x_3 = b/2$ line, i.e.,

$$\begin{aligned} T(0, x_3) &= 100, \quad T(a, x_3) = 200 \\ T(x_2, 0) &= 100, \quad T(x_2, b) = 100 \end{aligned}$$

then we obtain a simpler form of solution. First, applying the boundary condition $T(x_2, 0) = 100$, we get

$$T(x_2, x_3) = 100 + Jx_3 + (C' \cosh kx_2 + D' \sinh kx_2)\sin kx_3 \tag{123}$$

where $AE = 100, B = 0, G = 0$, and CH has been combined into C', DH into D', and AF into J. Next, application of the boundary condition $T(x_2, b) = 100$ in the above equation produces

$$T(x_2, b) = 100 + Jx_3 + (C' \cosh kx_2 + D' \sinh kx_2)\sin kb = 100 \tag{124}$$

from which we obtain

$$J = 0, \ \ \sin kb = 0$$

Therefore, the solution becomes

$$T(x_2, x_3) = 100 + \sum_{n=1}^{\infty}(C_m \cosh\frac{m\pi x_2}{b} + D_m \sinh\frac{m\pi x_2}{b})\sin\frac{m\pi x_3}{b} \tag{125}$$

After application of the boundary conditions $T(0, x_3) = 100$ and $T(a, x_3) = 200$, the unknown coefficients C_m, D_m are obtained, by using orthogonality properties of $\sin\frac{m\pi y}{b}$, in the form

$$C_m = 0 \tag{126}$$

$$D_m = \frac{2}{\sinh\frac{m\pi a}{b}}\int_0^b 100\sin\frac{m\pi x_3}{b}dx_3 = \frac{400}{m\pi\sinh\frac{m\pi a}{b}} \qquad (m = 1, 3, 5, ...) \tag{127}$$

Thus, the solution in this case is given by Eqs. (125), (126), and (127).

4.2 N$_\beta$-strip Case

In the N$_\beta$-strip problem, the rectangular plate, which has length a and height b, is divided into N$_\beta$ strips along the x_2 direction. Therefore, every strip has height b and width a_β, where $\beta = 1, ..., N_\beta$, Figure 11. Since the boundary conditions on the top and bottom surface are given in terms of constant temperature, the analytical solution can be developed first from Eqs. (116) or (125) of the previous section depending on the applied boundary conditions.

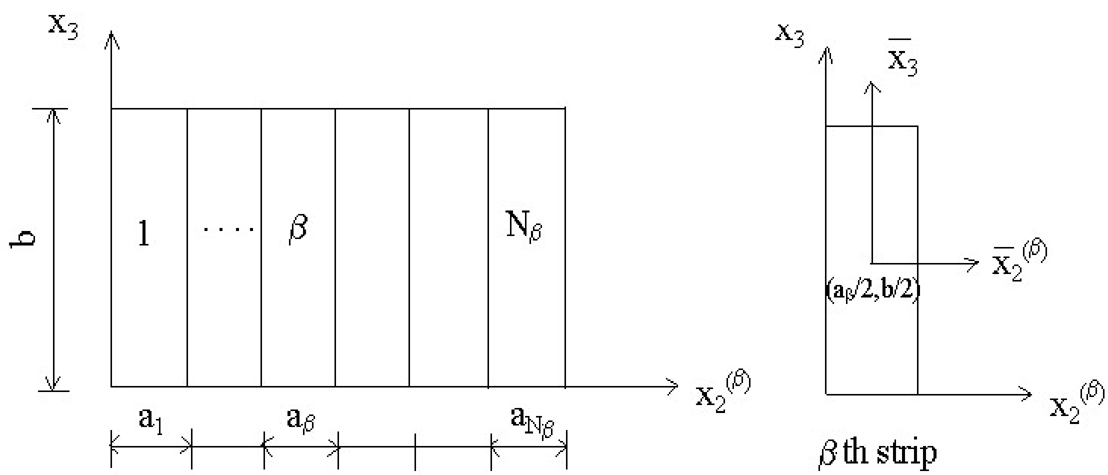

Figure 11. N$_\beta$-strip case problem definition.

Case (i)

Assume the boundary conditions on the top and bottom faces are $T_{top} = 200$ and $T_{bot} = 100$. Then the temperature field in the arbitrary βth strip is given by Eq. (116) as follows,

$$T^{(\beta)}(x_2^{(\beta)}, x_3) = 200 - \frac{100x_3}{b} + \sum_{m=1}^{\infty}(C_m^{(\beta)} \cosh \frac{m\pi x_2^{(\beta)}}{b} + D_m^{(\beta)} \sinh \frac{m\pi x_2^{(\beta)}}{b}) \sin \frac{m\pi x_3}{b}$$

However, it should be noted that this solution is obtained in the coordinate system with the origin located at the left-bottom corner. In order to obtain the solution in the coordinate system with the origin in the plate's center, we use the following coordinate transformation, Figure 11.

$$\bar{x}_2^{(\beta)} = x_2^{(\beta)} - a_\beta/2 \;\Rightarrow\; x_2^{(\beta)} = \bar{x}_2^{(\beta)} + a_\beta/2$$

$$\bar{x}_3 = x_3 - b/2 \;\Rightarrow\; x_3 = \bar{x}_3 + b/2$$

Therefore, the solution of the Laplace's equation in the translated coordinate system becomes

$$\begin{aligned} T^{(\beta)}(\bar{x}_2^{(\beta)}, \bar{x}_3) \;\;=\;\; & \sum_{m=1}^{\infty}[C_m^{(\beta)} \cosh \frac{m\pi(\bar{x}_2^{(\beta)} + a_\beta/2)}{b} + D_m^{(\beta)} \sinh \frac{m\pi(\bar{x}_2^{(\beta)} + a_\beta/2)}{b}] \times \\ & \sin \frac{m\pi(\bar{x}_3 + b/2)}{b} + 200 - \frac{100(\bar{x}_3 + b/2)}{b} \end{aligned} \tag{128}$$

Case (ii)

If the boundary conditions are changed to produce temperature distribution which is symmetric about the $x_3 = b/2$ line, i.e.,

$$T_{top} = T_{bottom} = 100$$

the temperature field in the arbitrary βth strip is given by Eq. (125) as follows

$$T^{(\beta)}(x_2^{(\beta)}, x_3) = 100 + \sum_{m=1}^{\infty}(C_m^{(\beta)} \cosh \frac{m\pi x_2^{(\beta)}}{b} + D_m^{(\beta)} \sinh \frac{m\pi x_2^{(\beta)}}{b}) \sin \frac{m\pi x_3}{b}$$

Upon transforming the above solution from the coordinate system with the origin located at the left-bottom corner to that with the origin in the plate's center, the solution of the Laplace's equation with the symmetry boundary condition becomes,

$$\begin{aligned} T^{(\beta)}(\bar{x}_2^{(\beta)}, \bar{x}_3) &= 100 + \sum_{m=1}^{\infty}[C_m^{(\beta)} \cosh \frac{m\pi(\bar{x}_2^{(\beta)} + a_\beta/2)}{b} + D_m^{(\beta)} \sinh \frac{m\pi(\bar{x}_2^{(\beta)} + a_\beta/2)}{b}] \times \\ & \quad \sin \frac{m\pi(\bar{x}_3 + b/2)}{b} \end{aligned} \tag{129}$$

In both cases, the solution for the unknown coefficients $C_m^{(\beta)}, D_m^{(\beta)}$ is obtained by constructing a system of equations which satisfies the heat flux and temperature continuity conditions at the interfaces separating the individual layers and the remaining boundary conditions. In order to make this as efficient as possible for large number of layers, we formulate the solution procedure using the local/global conductivity matrix approach.

In the local/global conductivity matrix approach, the unknown coefficients $C_m^{(\beta)}$ and $D_m^{(\beta)}$ are the key elements in constructing the local conductivity matrix. They are expressed and calculated in terms of the harmonics of common interfacial temperatures between adjacent strips and subsequently related to the corresponding interfacial heat flux harmonics through the local conductivity matrix. The detailed derivation is outlined in the following section.

4.2.1 Construction of the local conductivity matrix

In order to construct the local conductivity matrix, we start with the heat flux constitutive equation in the x_2 direction

$$q_2^{(\beta)} = -k_\beta \frac{\partial T}{\partial \bar{x}_2^{(\beta)}}, \;\; \beta = 1, ..., N_\beta \tag{130}$$

Substituting the expression for the temperature field given by Eq. (128) or (129), the above equation becomes

$$q_2^{(\beta)} = -k_\beta \sum_{m=1}^{\infty} \frac{m\pi}{b} \left[C_m^{(\beta)} \sinh \frac{m\pi(\bar{x}_2^{(\beta)} + a_\beta/2)}{b} + D_m^{(\beta)} \cosh \frac{m\pi(\bar{x}_2^{(\beta)} + a_\beta/2)}{b} \right] \sin \frac{m\pi(\bar{x}_3 + b/2)}{b} \tag{131}$$

The determination of the coefficients $C_m^{(\beta)}$ and $D_m^{(\beta)}$ for case (i) and case (ii) is outlined below.

Case (i)

In order to express the coefficients $C_m^{(\beta)}$ and $D_m^{(\beta)}$ in terms of the surface temperatures on the vertical boundaries of the βth strip, Eq. (128) is evaluated at $(a_\beta/2, \bar{x}_3)$ and $(-a_\beta/2, \bar{x}_3)$, respectively, yielding

$$T^{(\beta)}(a_\beta/2, \bar{x}_3) = 200 - \frac{100(\bar{x}_3 + b/2)}{b} + \sum_{m=1}^{\infty}[C_m^{(\beta)} \cosh \frac{m\pi a_\beta}{b} + D_m^{(\beta)} \sinh \frac{m\pi a_\beta}{b}] \sin \frac{m\pi(\bar{x}_3 + b/2)}{b} \tag{132}$$

or

$$[T^{(\beta)}(a_\beta/2,\bar{x}_3)-200+\frac{100(\bar{x}_3+b/2)}{b}]_m=\sum_{m=1}^{\infty}[C_m^{(\beta)}\cosh\frac{m\pi a_\beta}{b}+D_m^{(\beta)}\sinh\frac{m\pi a_\beta}{b}]\sin\frac{m\pi(\bar{x}_3+b/2)}{b} \tag{133}$$

and

$$T^{(\beta)}(-a_\beta/2,\bar{x}_3)=200-\frac{100(\bar{x}_3+b/2)}{b}+\sum_{m=1}^{\infty}C_m^{(\beta)}\sin\frac{m\pi(\bar{x}_3+b/2)}{b} \tag{134}$$

or

$$[T^{(\beta)}(-a_\beta/2,\bar{x}_3)-200+\frac{100(\bar{x}_3+b/2)}{b}]_m=\sum_{m=1}^{\infty}C_m^{(\beta)}\sin\frac{m\pi(\bar{x}_3+b/2)}{b} \tag{135}$$

The corresponding interfacial temperature harmonics at the left $(-a_\beta/2,\bar{x}_3)$ and right $(a_\beta/2,\bar{x}_3)$ boundary for an arbitrary βth strip can be obtained from Eqs. 133) and (135), respectively, using orthogonality relations

$$\begin{aligned}(T_2^+)_m^{(\beta)} &= \int_{-b/2}^{b/2}\left[T^{(\beta)}(a_\beta/2,\bar{x}_3)-200+\frac{100(\bar{x}_3+b/2)}{b}\right]\sin\frac{m\pi(\bar{x}_3+b/2)}{b}d\bar{x}_3\\ &= \int_{-b/2}^{b/2}\sum_{m=1}^{\infty}[C_m^{(\beta)}\cosh\frac{m\pi a_\beta}{b}+D_m^{(\beta)}\sinh\frac{m\pi a_\beta}{b}]\sin^2\frac{m\pi(\bar{x}_3+b/2)}{b}d\bar{x}_3\end{aligned}$$

and

$$\begin{aligned}(T_2^-)_m^{(\beta)} &= \int_{-b/2}^{b/2}\left[T^{(\beta)}(-a_\beta/2,\bar{x}_3)-200+\frac{100(\bar{x}_3+b/2)}{b}\right]\sin\frac{m\pi(\bar{x}_3+b/2)}{b}d\bar{x}_3\\ &= \int_{-b/2}^{b/2}\sum_{m=1}^{\infty}C_m^{(\beta)}\sin^2\frac{m\pi(\bar{x}_3+b/2)}{b}d\bar{x}_3\end{aligned}$$

Performing the required integrations, the above two equations become

$$(T_2^+)_m^{(\beta)} = \frac{b}{2}(C_m^{(\beta)}\cosh\frac{m\pi a_\beta}{b}+D_m^{(\beta)}\sinh\frac{m\pi a_\beta}{b}) \tag{136}$$

$$(T_2^-)_m^{(\beta)} = \frac{b}{2}C_m^{(\beta)} \tag{137}$$

Upon writing the above two equations in matrix form, we obtain

$$\left[\begin{array}{c}T_2^-\\T_2^+\end{array}\right]_m^{(\beta)}=\left[\begin{array}{cc}\frac{b}{2} & 0\\ \frac{b}{2}\cosh\frac{m\pi a_\beta}{b} & \frac{b}{2}\sinh\frac{m\pi a_\beta}{b}\end{array}\right]\left[\begin{array}{c}C_m\\D_m\end{array}\right]^{(\beta)} \tag{138}$$

Inverting the above system, the coefficients $C_m^{(\beta)}$ and $D_m^{(\beta)}$ are expressed in terms of the interfacial temperature harmonics as follows

$$
\left[\begin{array}{c} C_m \\ D_m \end{array}\right]^{(\beta)} = \left[\begin{array}{cc} \dfrac{b}{2} & 0 \\ \dfrac{b}{2}\cosh\dfrac{m\pi a_\beta}{b} & \dfrac{b}{2}\sinh\dfrac{m\pi a_\beta}{b} \end{array}\right]^{-1} \left[\begin{array}{c} T_2^- \\ T_2^+ \end{array}\right]_m^{(\beta)} \tag{139}
$$

Similarly, evaluating the heat flux at the left $(-a_\beta/2, \bar{x}_3)$ and right $(a_\beta/2, \bar{x}_3)$ boundary for the βth strip, respectively, yields

$$
\begin{aligned}
q_2^{(\beta)}(a_\beta/2, \bar{x}_3) &= -k_\beta \sum_{m=1}^{\infty} \left(\frac{m\pi}{b} C_m^{(\beta)} \sinh\frac{m\pi a_\beta}{b} + D_m^{(\beta)} \cosh\frac{m\pi a_\beta}{b}\right) \sin\frac{m\pi(\bar{x}_3 + b/2)}{b} \\
-q_2^{(\beta)}(-a_\beta/2, \bar{x}_3) &= k_\beta \sum_{m=1}^{\infty} \frac{m\pi}{b} D_m^{(\beta)} \sin\frac{m\pi(\bar{x}_3 + b/2)}{b}
\end{aligned}
$$

The interfacial heat flux harmonics for an arbitrary βth strip are obtained from the above two equations by using orthogonality relations,

$$
\begin{aligned}
(Q_2^+)_m^{(\beta)} &= \int_{-b/2}^{b/2} q_2^{(\beta)}(a_\beta/2, \bar{x}_3) \sin\frac{m\pi(\bar{x}_3 + b/2)}{b} d\bar{x}_3 \qquad (140) \\
&= \int_{-b/2}^{b/2} -k_\beta \sum_{m=1}^{\infty} \left(\frac{m\pi}{b} C_m^{(\beta)} \sinh\frac{m\pi a_\beta}{b} + D_m^{(\beta)} \cosh\frac{m\pi a_\beta}{b}\right) \sin^2\frac{m\pi(\bar{x}_3 + b/2)}{b} d\bar{x}_3 \\
-(Q_2^-)_m^{(\beta)} &= \int_{-b/2}^{b/2} q_2^{(\beta)}(-a_\beta/2, \bar{x}_3) \sin\frac{m\pi(\bar{x}_3 + b/2)}{b} d\bar{x}_3 \\
&= \int_{-b/2}^{b/2} -k_\beta \sum_{m=1}^{\infty} \frac{m\pi}{b} D_m^{(\beta)} \sin^2\frac{m\pi(\bar{x}_3 + b/2)}{b} d\bar{x}_3 \qquad (141)
\end{aligned}
$$

The above two equations can be expressed in matrix form as follows

$$
\left[\begin{array}{c} -Q_2^- \\ Q_2^+ \end{array}\right]_m^{(\beta)} = \left[\begin{array}{cc} 0 & -\dfrac{m\pi k_\beta}{2} \\ -\dfrac{m\pi k_\beta}{2}\sinh\dfrac{m\pi a_\beta}{b} & -\dfrac{m\pi k_\beta}{2}\cosh\dfrac{m\pi a_\beta}{b} \end{array}\right] \left[\begin{array}{c} C_m \\ D_m \end{array}\right]^{(\beta)} \tag{142}
$$

Case (ii)

Similar to case (i), evaluating the surface temperatures on the vertical boundaries of the βth strip i.e., Eq. (129) at $(a_\beta/2, \bar{x}_3)$ and $(-a_\beta/2, \bar{x}_3)$, respectively, yields

$$
T^{(\beta)}(a_\beta/2, \bar{x}_3) = 100 + \sum_{m=1}^{\infty} [C_m^{(\beta)} \cosh\frac{m\pi a}{b} + D_m^{(\beta)} \sinh\frac{m\pi a_\beta}{b}] \sin\frac{m\pi(\bar{x}_3 + b/2)}{b} \tag{143}
$$

or

$$
[T^{(\beta)}(a_\beta/2, \bar{x}_3) - 100]_m = \sum_{m=1}^{\infty} [C_m^{(\beta)} \cosh\frac{m\pi a_\beta}{b} + D_m^{(\beta)} \sinh\frac{m\pi a_\beta}{b}] \sin\frac{m\pi(\bar{x}_3 + b/2)}{b} \tag{144}
$$

and

$$T^{(\beta)}(-a_\beta/2, \bar{x}_3) = 100 + \sum_{m=1}^{\infty} C_m^{(\beta)} \sin \frac{m\pi(\bar{x}_3 + b/2)}{b} \tag{145}$$

or

$$[T^{(\beta)}(-a_\beta/2, \bar{x}_3) - 100]_m = \sum_{m=1}^{\infty} C_m^{(\beta)} \sin \frac{m\pi(\bar{x}_3 + b/2)}{b} \tag{146}$$

The corresponding interfacial temperature harmonics at the left $(-a_\beta/2, \bar{x}_3)$ and right $(a_\beta/2, \bar{x}_3)$ boundary for an arbitrary βth strip can be obtained from Eqs. (144) and (146), respectively, using orthogonality relations

$$\begin{aligned} (T_2^+)_m^{(\beta)} &= \int_{-b/2}^{b/2} \left[T^{(\beta)}(a_\beta/2, \bar{x}_3) - 100\right] \sin \frac{m\pi(\bar{x}_3 + b/2)}{b} d\bar{x}_3 \\ &= \int_{-b/2}^{b/2} \sum_{m=1}^{\infty} [C_m^{(\beta)} \cosh \frac{m\pi a_\beta}{b} + D_m^{(\beta)} \sinh \frac{m\pi a_\beta}{b}] \sin^2 \frac{m\pi(\bar{x}_3 + b/2)}{b} d\bar{x}_3 \end{aligned}$$

and

$$\begin{aligned} (T_2^-)_m^{(\beta)} &= \int_{-b/2}^{b/2} \left[T^{(\beta)}(-a_\beta/2, \bar{x}_3) - 100\right] \sin \frac{m\pi(\bar{x}_3 + b/2)}{b} d\bar{x}_3 \\ &= \int_{-b/2}^{b/2} \sum_{m=1}^{\infty} C_m^{(\beta)} \sin^2 \frac{m\pi(\bar{x}_3 + b/2)}{b} d\bar{x}_3 \end{aligned}$$

Upon performing the above integrations, these two equations simplify to

$$(T_2^+)_m^{(\beta)} = \frac{b}{2}(C_m^{(\beta)} \cosh \frac{m\pi a_\beta}{b} + D_m^{(\beta)} \sinh \frac{m\pi a_\beta}{b}) \tag{147}$$

$$(T_2^-)_m^{(\beta)} = \frac{b}{2} C_m^{(\beta)} \tag{148}$$

Writing the above two equations in matrix form, we obtain

$$\begin{bmatrix} T_2^- \\ T_2^+ \end{bmatrix}_m^{(\beta)} = \begin{bmatrix} \frac{b}{2} & 0 \\ \frac{b}{2} \cosh \frac{m\pi a_\beta}{b} & \frac{b}{2} \sinh \frac{m\pi a_\beta}{b} \end{bmatrix} \begin{bmatrix} C_m \\ D_m \end{bmatrix}^{(\beta)} \tag{149}$$

which has the same form as Eq. (138) obtained for case (i) with the first kind of boundary conditions. Further, since the expression for the heat flux, Eq. (131), for both boundary conditions does not change, the relationship between the coefficients $C_m^{(\beta)}$ and $D_m^{(\beta)}$ and the interfacial heat flux harmonics, i.e., Eq. (142), is also the same. However, the specific values of the coefficients $C_m^{(\beta)}$, $D_m^{(\beta)}$ and the corresponding interfacial temperatures $(T_2^-)_m^{(\beta)}, (T_2^+)_m^{(\beta)}$, heat fluxes $(Q_2^-)_m^{(\beta)}, (Q_2^+)_m^{(\beta)}$ are not the same due to the different expressions for the solution of Laplace's equation with different kinds of boundary conditions.

Nevertheless, in both cases, upon substituting the expression for the coefficients $C_m^{(\beta)}$ and $D_m^{(\beta)}$ given by Eq. (139) into Eq. (142), carrying out the matrix multiplication and simplifying, we obtain the same relationship between the interfacial heat flux and interfacial temperature harmonics, i.e., the local conductivity matrix,

$$\begin{bmatrix} -Q_2^- \\ Q_2^+ \end{bmatrix}_m^{(\beta)} = \begin{bmatrix} \kappa_{11} & \kappa_{12} \\ \kappa_{21} & \kappa_{22} \end{bmatrix}_m^{(\beta)} \begin{bmatrix} T_2^- \\ T_2^+ \end{bmatrix}_m^{(\beta)} \tag{150}$$

where

$$(\kappa_{11})_m^{(\beta)} = \frac{m\pi k_\beta \cosh \dfrac{m\pi a_\beta}{b}}{b \sinh \dfrac{m\pi a_\beta}{b}}$$
$$(\kappa_{12})_m^{(\beta)} = -\frac{m\pi k_\beta}{b \sinh \dfrac{m\pi a_\beta}{b}}$$
$$(\kappa_{21})_m^{(\beta)} = -\frac{m\pi k_\beta}{b} \sinh \frac{m\pi a_\beta}{b} + \frac{k_\beta m\pi \cosh^2 \dfrac{m\pi a_\beta}{b}}{b \sinh \dfrac{m\pi a_\beta}{b}}$$
$$(\kappa_{22})_m^{(\beta)} = -\frac{m\pi k_\beta \cosh \dfrac{m\pi a_\beta}{b}}{b \sinh \dfrac{m\pi a_\beta}{b}}$$

4.2.2 Global conductivity matrix assembly

Imposition of the continuity of interfacial heat flux and interfacial temperature along common interfaces between adjacent strips, together with the external boundary conditions, gives rise to a system of equations in the unknown interfacial temperature harmonics. The continuity of interfacial heat flux is obtained by requiring the sum of the heat flux acting on the interface separating β and $\beta + 1$ strip to be zero,

$$(Q_2^+)_m^{(\beta)} + (Q_2^-)_m^{(\beta+1)} = 0 \qquad \beta = 1, ...N_\beta - 1 \tag{151}$$

whereas the continuity of interfacial temperature is given by

$$(T_2^+)_m^{(\beta)} = (T_2^-)_m^{(\beta+1)} = T_2^\beta \quad \beta = 1, ...N_\beta - 1 \tag{152}$$

The system equations is constructed by using Eq. (151) at each interface along the x_2 direction, starting with the left boundary where the boundary condition is prescribed, together with application of the temperature continuity condition defined by Eq. (152), and proceeding to the right boundary. Following this procedure, we obtain the following system of equations for the mth harmonic of the interfacial temperatures

$$\begin{array}{ll}
\text{left boundary:} & \kappa_{11}^1 T_2^{left} + \kappa_{12}^1 T_2^1 = -Q_2^{left} \\
1st \text{ interface:} & \kappa_{21}^1 T_2^{left} + (\kappa_{22}^1 + \kappa_{11}^2) T_2^1 + \kappa_{12}^2 T_2^2 = 0 \\
. & \\
\beta th \text{ interface:} & \kappa_{21}^{\beta-1} T_2^{\beta-2} + (\kappa_{22}^{\beta-1} + \kappa_{11}^{\beta}) T_2^{\beta-1} + \kappa_{12}^{\beta} T_2^{\beta} = 0 \\
\beta + 1th \text{ interface:} & \kappa_{21}^{\beta} T_2^{\beta-1} + (\kappa_{22}^{\beta} + \kappa_{11}^{\beta+1}) T_2^{\beta} + \kappa_{12}^{\beta+1} T_2^{\beta+1} = 0 \\
. & \\
N_\beta - 1th \text{ interface:} & \kappa_{21}^{N_\beta-1} T_2^{N_\beta-2} + (\kappa_{11}^{N_\beta} + \kappa_{22}^{N_\beta-1}) T_2^{N_\beta-1} + \kappa_{12}^{N_\beta} T_2^{right} = 0 \\
\text{right boundary:} & \kappa_{21}^{N_\beta} T_2^{N_\beta-1} + \kappa_{22}^{N_\beta} T_2^{right} = Q_2^{right}
\end{array}$$

where N_β is the number of strips, and the harmonic number m has been suppressed. The above equations can be expressed in matrix form for the mth harmonic as follows

$$\begin{bmatrix} \kappa_{11}^1 & \kappa_{12}^1 & . & 0 & 0 & . & 0 & 0 \\ \kappa_{21}^1 & \kappa_{22}^1+\kappa_{11}^2 & . & 0 & 0 & . & 0 & 0 \\ 0 & 0 & . & 0 & 0 & . & 0 & 0 \\ 0 & 0 & . & \kappa_{22}^{\beta-1}+\kappa_{11}^{\beta} & \kappa_{12}^{\beta} & . & 0 & 0 \\ 0 & 0 & . & \kappa_{21}^{\beta} & \kappa_{22}^{\beta}+\kappa_{11}^{\beta+1} & . & 0 & 0 \\ 0 & 0 & . & 0 & 0 & . & 0 & 0 \\ 0 & 0 & . & 0 & 0 & . & \kappa_{22}^{N_\beta-1}+\kappa_{11}^{N_\beta} & \kappa_{12}^{N_\beta} \\ 0 & 0 & . & 0 & 0 & . & \kappa_{21}^{N_\beta} & \kappa_{22}^{N_\beta} \end{bmatrix}_m \begin{bmatrix} T_2^{left} \\ T_2^1 \\ . \\ T_2^{k-1} \\ T_2^k \\ . \\ T_2^{N_\beta-1} \\ T_2^{right} \end{bmatrix}_m = \begin{bmatrix} -Q_2^{left} \\ 0 \\ . \\ . \\ . \\ . \\ 0 \\ Q_2^{right} \end{bmatrix}_m$$

The solution of the above system of equations for each interfacial temperature harmonic makes possible the determination of the coefficients $C_m^{(\beta)}$ and $D_m^{(\beta)}$ using Eq. (139). These, in turn, determine the temperature field in each strip of the plate using either Eq. (128) or (129).

5 Mesh Sensitivity, Validation and Application Studies

The user-friendly formulation of HOTFGM, developed in Section 2, dispenses with the two-level volume discretization employed in the original HOTFGM formulation wherein generic cells are further discretized into subcells. In the user-friendly formulation the graded microstructure is built up directly using subcells which play the role of fundamental subvolumes. This simplification in the volume discretization, which also simplified the derivation of the interfacial heat flux continuity conditions, provided the basis for the efficient reformulation outlined in Section 3. Therefore, the present section begins with the validation of the user-friendly formulation using the analytical solutions developed in Section 4. This is accomplished in two steps. First, we examine the convergence of the temperature field to the analytical solution as a function of the mesh discretization for the problem of a homogeneous plate subjected to the thermal boundary conditions discussed in Section 4. Once the convergence characteristics of the solution based on the user-friendly formulation are established, we then consider the problem of a piece-wise uniformly graded plate for which the analytical solution has also been derived in Section 4. This problem is subsequently re-solved using the reformulation of HOTFGM with variable thermal conductivity in order to demonstrate the reduction in the graded microstructure's volume dicretization obtained by assuming linearly varying material properties. In the last example, a graded thermal barrier coating subjected to a through-thickness thermal gradient is considered, and the differences in the solutions based on the actual and homogenized microstructures are discussed.

5.1 User-Friendly Formulation

5.1.1 Mesh sensitivity study: homogeneous plate

Let us consider a square plate, whose sides are unit length (i.e., $a = b = 1$), Figure 12, subjected to the following two sets of boundary conditions:

$$\begin{array}{lll} (1) & : & T_{left} = 100^\circ C, \quad T_{right} = 200^\circ C, \quad T_{top} = 100^\circ C, \quad T_{bottom} = 100^\circ C \\ (2) & : & T_{left} = 100^\circ C, \quad T_{right} = 200^\circ C, \quad T_{top} = 100^\circ C, \quad T_{bottom} = 200^\circ C \end{array}$$

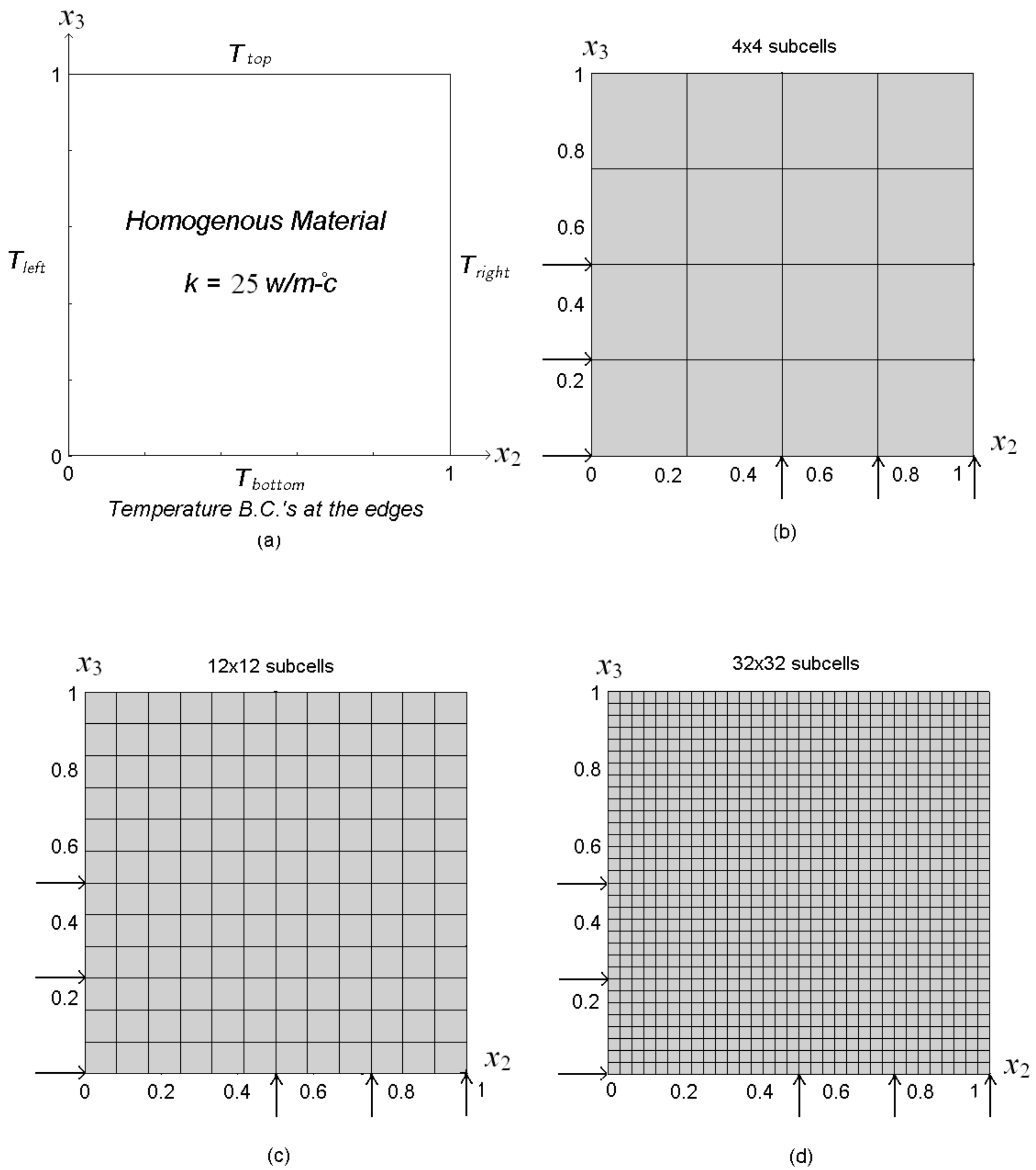

Figure 12. Problem definition and mesh discretization for a homogeneous plate.

The first set produces a temperature field that is symmetric about a horizontal line halfway across the plate's height, whereas the second set produces a temperature field that is symmetric about a line connecting the upper left and lower right corners of the plate. Such temperature fields are sufficiently complicated to test the higher-order theory's predictive capability. The plate's thermal conductivity k has a constant value, i.e., $k = 25\ W/m -^\circ C$. Since the plate is homogeneous, however, the temperature field does not depend on the conductivity under steady-state boundary conditions. This provided an additional check on the user-friendly formulation's correctness as verified during preliminary numerical tests.

The convergence behavior of the user-friendly formulation is investigated as a function of volume discretization by dividing the plate into $4 \times 4, 12 \times 12, 32 \times 32$ uniformly-spaced subcells, Figure 12. The corresponding contour plots of the temperature distributions for the employed volume discretizations are compared with the analytical solution in Figure 13 for the first set of applied thermal boundary conditions. As is clearly seen in the contour plots, the temperature distributions obtained from the user-friendly formulation are symmetric with respect to the horizontal line halfway across the plate's height irrespective of the volume discretization, and gradually approach the analytical solution with increasing number of subcells. In the case of the 4×4 subcell mesh, we obtain only an approximate temperature field which, nevertheless, exhibits the basic characteristics of the analytical solution. Increasing the volume discretization to 12×12 subcells generates a temperature field which appears quite close to the analytical solution except at the upper and lower right corners where the boundary temperature distributions change suddenly, producing discontinuities at these corners. Increasing the mesh to 32×32 subcells eliminates these local corner disturbances, producing smooth curve patterns in the temperature field which are visually the same as those obtained from the analytical solution.

A more quantitive picture of the user-friendly formulation's convergence behavior with mesh refinement is obtained by plotting the temperature distributions along specific cross sections. Three horizontal cross sections and three vertical cross sections have been chosen as illustrated by the arrows in Figure 12. The horizontal cross sections are situated at the elevations $x_3 = 0.0$, 0.25, 0.5, and the vertical cross sections are situated at $x_2 = 0.5, 0.75, 1.0$. The cross sections include the lower horizontal boundary defined by $x_3 = 0.0$ and the right vertical boundary defined by $x_2 = 1.0$. The interior cross sections have been chosen such that they run along subcell interfaces. For example, the cross-section situated at $x_3 = 0.25$ runs along the horizontal interfaces that separate the sets of subcells ($\beta 1$) and ($\beta 2$) in the case of the 4×4 subcell mesh. This same cross section runs along the horizontal interfaces that separate the sets of subcells ($\beta 3$) and ($\beta 4$) for the 12×12 subcell mesh.

As we know from the user-friendly formulation, the temperature distributions along the different interior cross sections can be obtained by using microvariables associated with the subcell on either side of the common interface. Furthermore, recall that the thermal and heat flux continuity conditions were applied in a surface-average sense. Therefore, the temperature distributions along a given cross section separating two sets of subcells, obtained using two different sets of microvariables associated with either set of subcells, will generally be different. However, these distributions should approach the actual temperature distributions with increasing mesh refinement. Furthermore, the surface-averaged interfacial temperatures, which exhibit piece-wise uniform distributions, should approach the actual temperature distributions in a step-wise manner with increasing mesh refinement.

In order to demonstrate the above behavior, three types of temperature distributions along the chosen subcell interfaces have been generated for the interior cross sections. In the following horizontal cross-section plots, we define the common interfacial surface-averaged temperature as $\bar{T}$, the interfacial temperature obtained using the microvariables of the subcells below the interfaces as T^+, and the interfacial temperature obtained sing the microvariables of the subcells above the

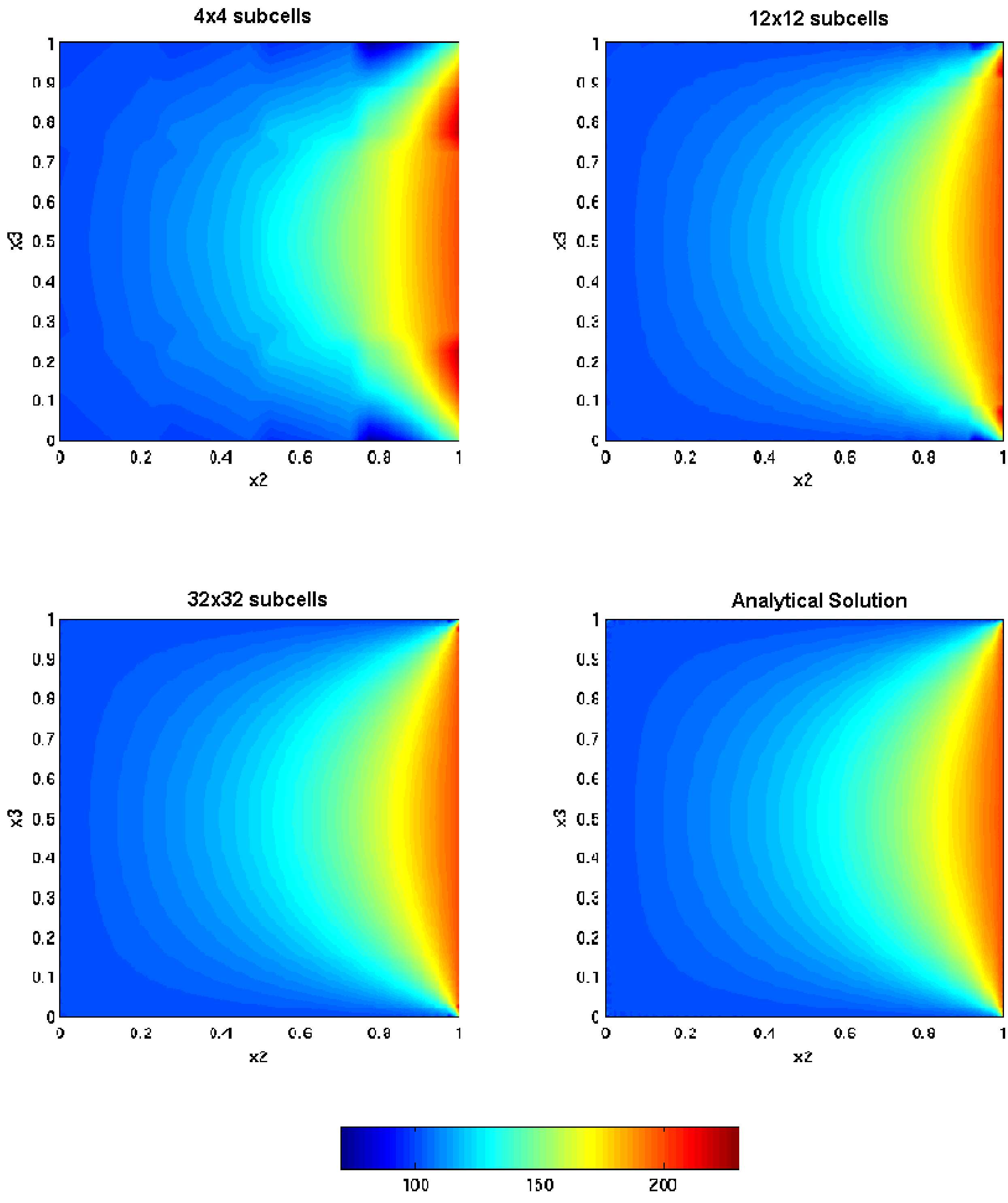

Figure 13. Temperature fields for the three mesh discretizations and first set of boundary conditions. Comparison with the analytical solution.

interfaces as T^-. Similar notation is used for the vertical cross-section plots. In these cases, T^+ indicates the interfacial temperature obtained using the microvariables of the subcells lying to the left of the subcell interfaces and T^- denotes the interfacial temperature obtained using the microvariables of the subcells lying to the right of the subcell interfaces. In the case of the boundary subcells, only two curves are given since there is only one set of subcells forming the boundary. As before, the designation $\bar{T}$ is used to denote the surface-averaged temperature distribution along both the horizontal and vertical boundaries. The second curve is obtained using the properties of the boundary subcells: for the lower horizontal boundary it is denoted by T^- and for the right vertical boundary it is denoted by T^+ for consistency with the established notation.

The temperature distributions along the interior horizontal cross sections at the two elevations $x_3 = 0.25$ and $x_3 = 0.5$ for the first set of boundary conditions are shown in Figure 14. For the 4×4 subcell mesh, the temperature distributions calculated on the different sides of the subcell interfaces in the $x_3 = 0.25$ cross section shown in the left column of Figure 14 are quite different, with discontinuities or jumps evident as the subcell vertical interfaces are traversed along the x_2 direction. The differences, however, gradually disappear with increasing mesh refinement, including the above-mentioned jumps. In the case of the 12×12 subcell mesh the differences are already quite small and barely visually discernible, while in the case of the 32×32 subcell mesh the differences cannot be identified visually. These distributions are graphically indistinguishable from the actual distributions obtained from the analytical solution (not shown). The surface-averaged temperature distributions also gradually converge to the actual temperature distributions in a step-wise manner.

The corresponding distributions in the $x_3 = 0.5$ cross section are shown in the right column of Figure 14. The same observations with regard to the solution's convergence with increasing mesh refinement hold in this cross section as in the preceding one, with one important difference however. Interestingly, we only see two curves in this cross section, namely the surface-averaged temperature distribution $\bar{T}$ and the two T^+ and T^- distributions superposed on each other. This is due to the symmetric boundary conditions employed in this example, which in turn produce a temperature field that is symmetric with respect to the $x_3 = 0.5$ cross section. This, in turn, ensures that the subcell microvariables on either side of the line of symmetry are the same, producing the same interfacial temperature distributions. This behavior is clearly captured by the user-friendly formulation, providing further evidence of its correctness.

Figure 15 shows the temperature distributions along the vertical cross sections $x_2 = 0.5$ and $x_2 = 0.75$ as a function of the volume discretization for the first set of boundary conditions. In this case, the temperature distributions are not symmetric about any of the two cross sections, and consequently three distinct sets of interfacial temperature distributions, $\bar{T}$, T^+ and T^- are present. Symmetry exists only about the $x_3 = 0.5$ cross section, and this is reflected in each of the individual distributions for each cross section (since the temperature distributions are given as a function of the x_3 coordinate) and for each volume discretization. As in the case of the horizontal cross sections, the difference between the T^+ and T^- distributions vanish with increasing mesh refinement (including the jumps at the subcell horizontal interfaces), while the $\bar{T}$ distribution approaches the actual distribution in a step-wise manner.

The temperature distributions at the two external boundaries $x_3 = 0$ and $x_2 = 1$ are given in Figure 16 for the three volume discretizations and the first set of boundary conditions. From these figures, we conclude that the T^- temperature distributions for the lower horizontal boundary, shown in the left column of Figure 16, and the T^+ temperature distributions for the right vertical boundary, shown in the right column of Figure 16, gradually approach the applied boundary conditions. However, even with 32×32 subcell mesh, they exhibit some fluctuations at the lower and upper right corners of the plate. That is because the applied temperature distributions possess discontinuities at these corners, requiring further mesh discretization in the vicinity of these points.

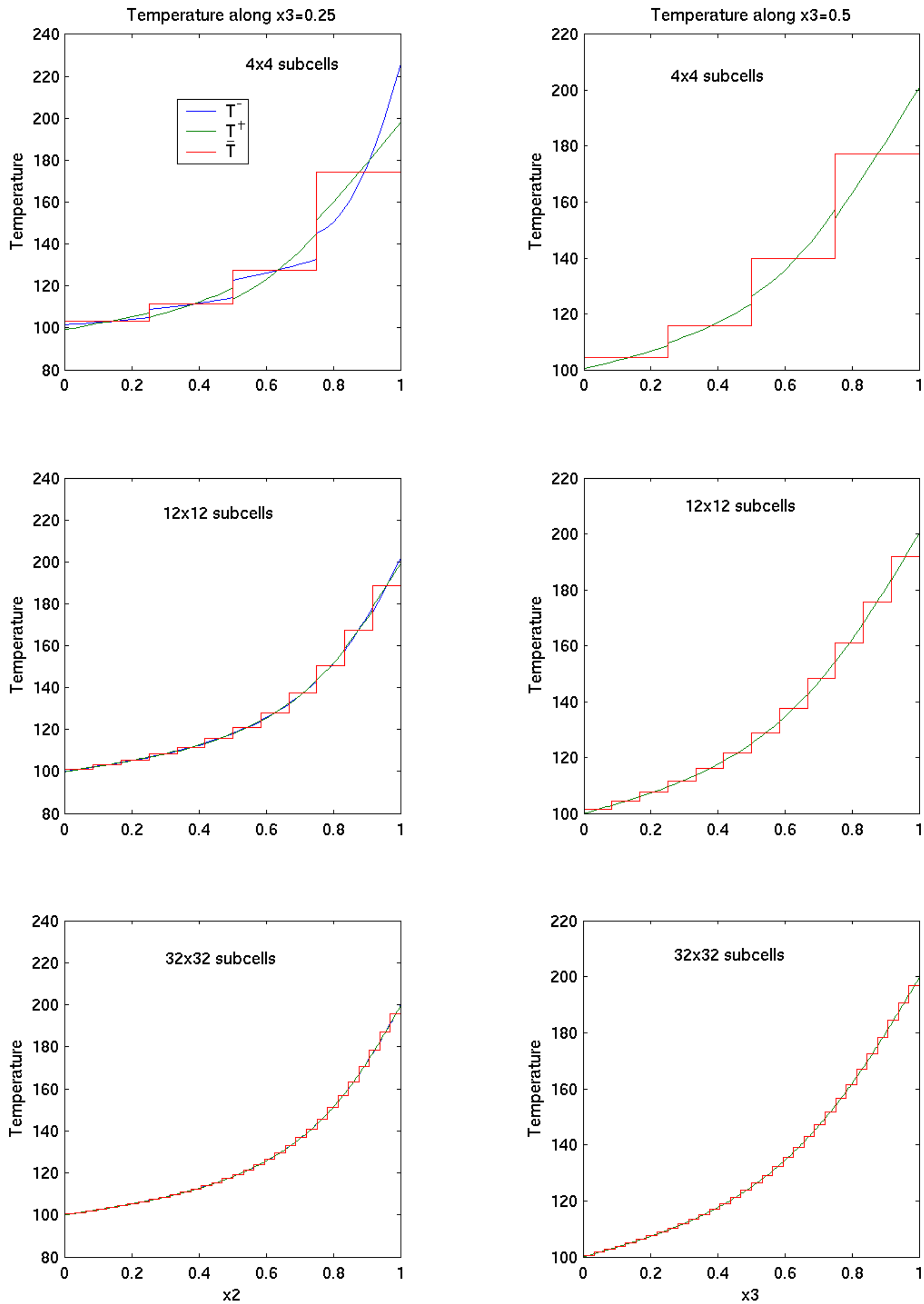

Figure 14. Convergence of temperature distributions along the cross-sections $x_3 = 0.25, 0.5$.

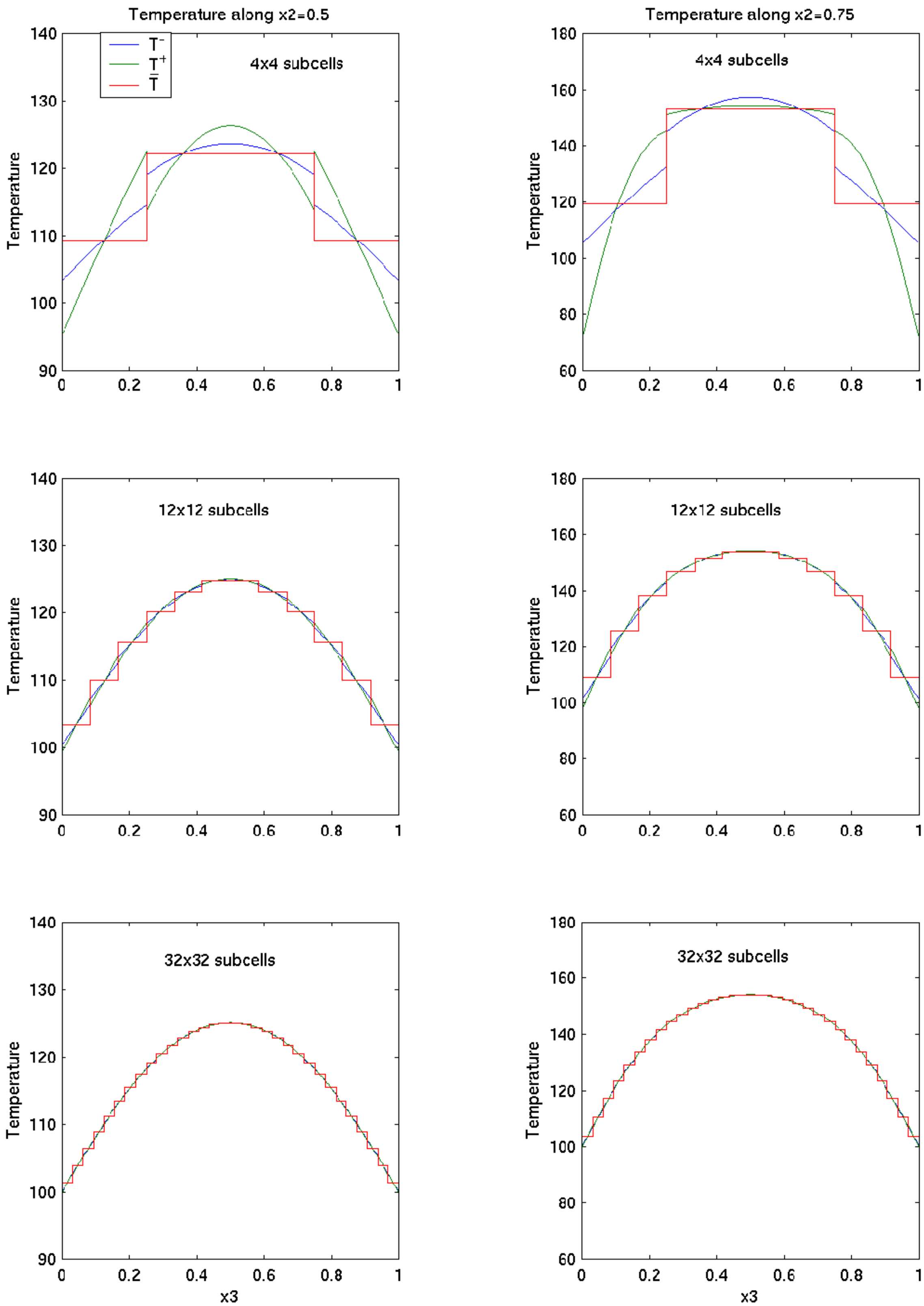

Figure 15. Convergences of the temperature distributions along the cross-sections $x_2 = 0.5, 0.75$.

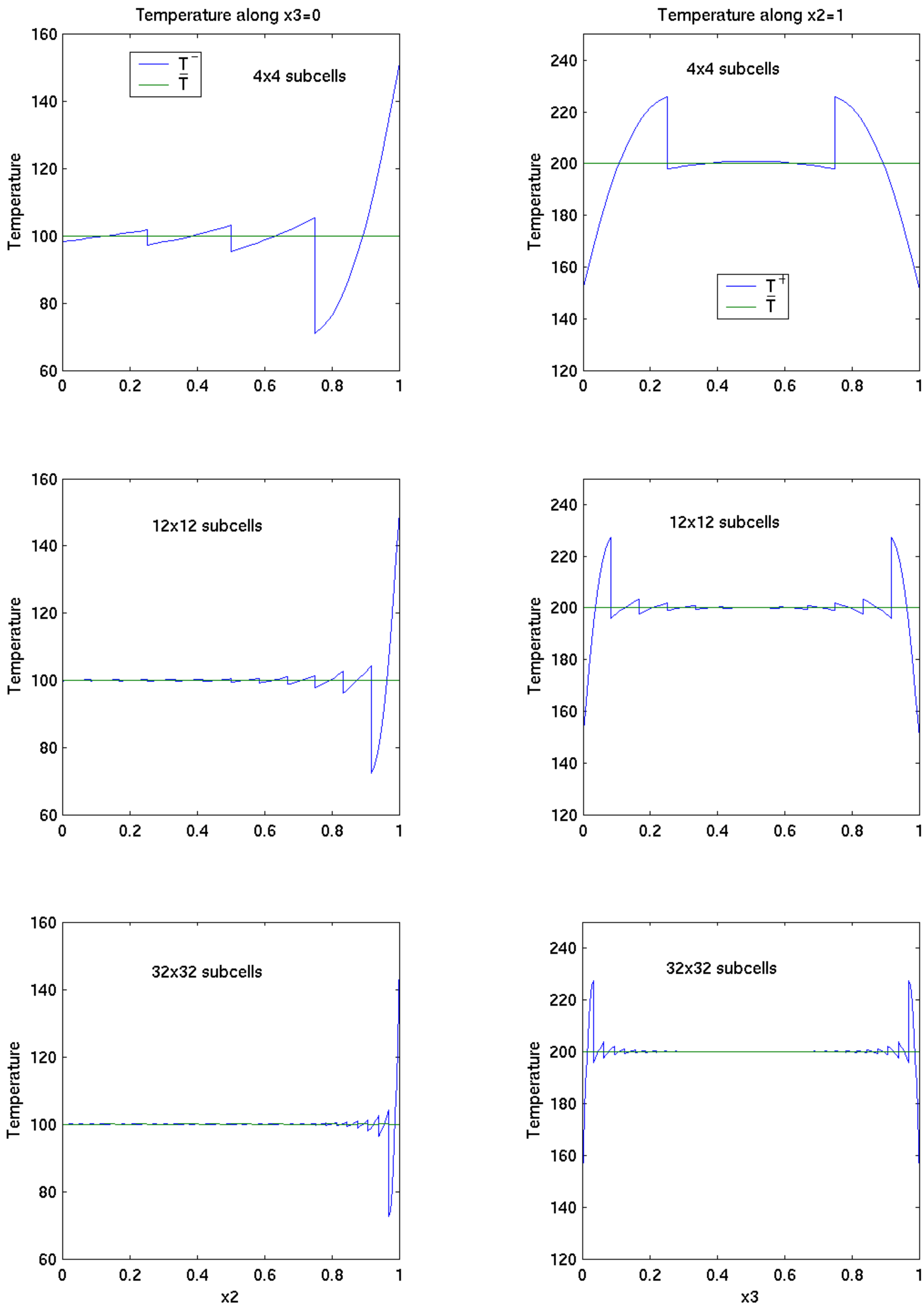

Figure 16. Convergence of the temperature distributions along the edges $x_3 = 0$ and $x_2 = 1$.

The corresponding temperature contour plots and cross section distributions for the second set of boundary conditions are given in Figures 17 through 20. The full field contour distributions shown in Figure 17 illustrate temperature field symmetry with respect to the cross section passing through the upper left and lower right corners of the plate for all three volume discretizations. As in the preceding case, the results obtained from the user-friendly formulation of the higher-order theory converge to the actual temperature distribution obtained from the analytical solution with increasing mesh refinement. The full field temperature distribution obtained from the 32×32 subcell mesh is visually indistinguishable from the distribution generated by the analytical solution. Similar observations with regard to the convergence behavior with increasing mesh refinement hold for the cross section temperature distributions along interfaces separating the interior subcells, presented in Figures 18 and 19, and along external boundaries presented in Figure 20. In this case, the temperature distributions are not symmetric about the chosen cross sections as expected, and therefore three distinct sets of interfacial distributions are evident in the interior, which converge with increasing mesh refinement at the same rate as before.

In summary, as observed from the above figures, whatever interfaces are considered, for either set of the boundary conditions (Figures 13-15 or Figures 17-20), the differences between the temperature distributions based on the microvariables belonging to adjacent subcells decrease with increasing number of subcells, while the surface-averaged temperature distributions approach the actual distributions in a step-wise manner, with the step increments becoming increasingly smaller. In other words, the greater the mesh refinement, the better the point-wise convergence or accuracy to the actual distribution.

5.1.2 Validation: discretely graded plate

In this section, the results from the user-friendly formulation for a plate with discretely graded thermal conductivity in a piecewise uniform manner are compared with the corresponding analytical solution outlined in Section 4 for the N_β-strip plate. The effect of thermal conductivity variation on the temperature field is also investigated.

We consider the same boundary value problem discussed in the preceding section but limit the investigation to the first type of boundary conditions, i.e., the plate is subjected to a temperature of $200°C$ on the right boundary and a temperature of $100°C$ on the remaining boundaries, Figure 21. The plate is divided into vertical strips and the thermal conductivity k (assuming isotropic thermal properties) is assigned a different constant value in each strip, producing a piecewise uniformly graded plate. The overall variation of the thermal conductivity is given by exponential functions in the x_2 coordinate. Two different thermal conductivity variations are employed. One is an exponentially increasing function of x_2

$$k = 0.5e^{5x_2}$$

while the other is an exponentially decreasing function of x_2

$$k = 60e^{-5x_2}$$

These continuous functions are employed to produce piecewise uniform variations as follows. The plate is divided into 25 vertical strips of equal width and the above functions are used to calculate the thermal conductivity at the center of each strip, which is then assumed to remain constant in that strip, as shown in the two lower graphs of Figure 21. The analytical solutions for this problem are then obtained based on the N_β-strip solution outlined in Section 4 using a 200 harmonic representation of the temperature field in each of the 25 strips. The corresponding user-friendly formulation solution is obtained by dividing the plate into 25×25 subcells of equal

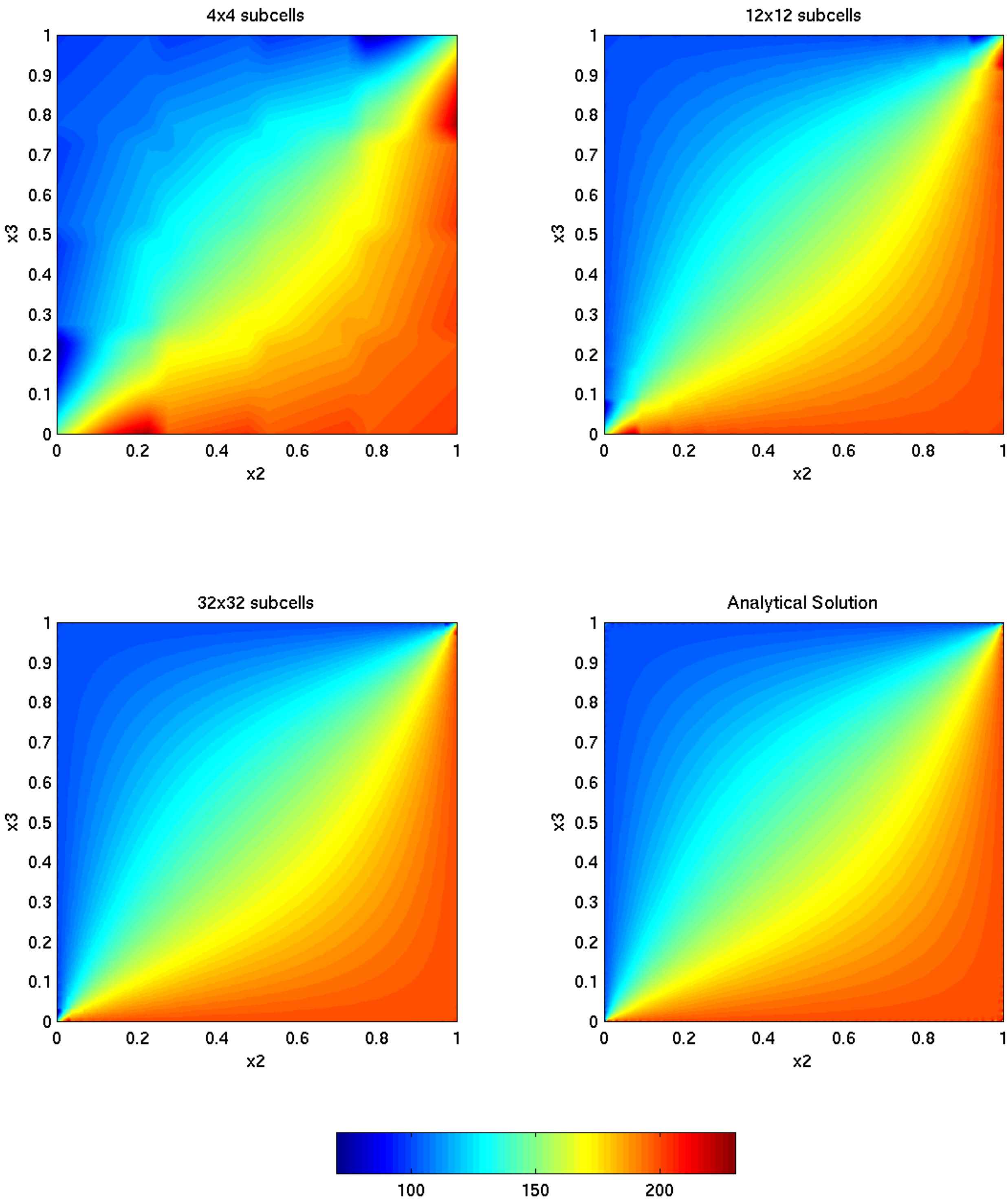

Figure 17. Temperature fields for the three mesh discretizations and second set of boundary conditions. Comparison with the analytical solution.

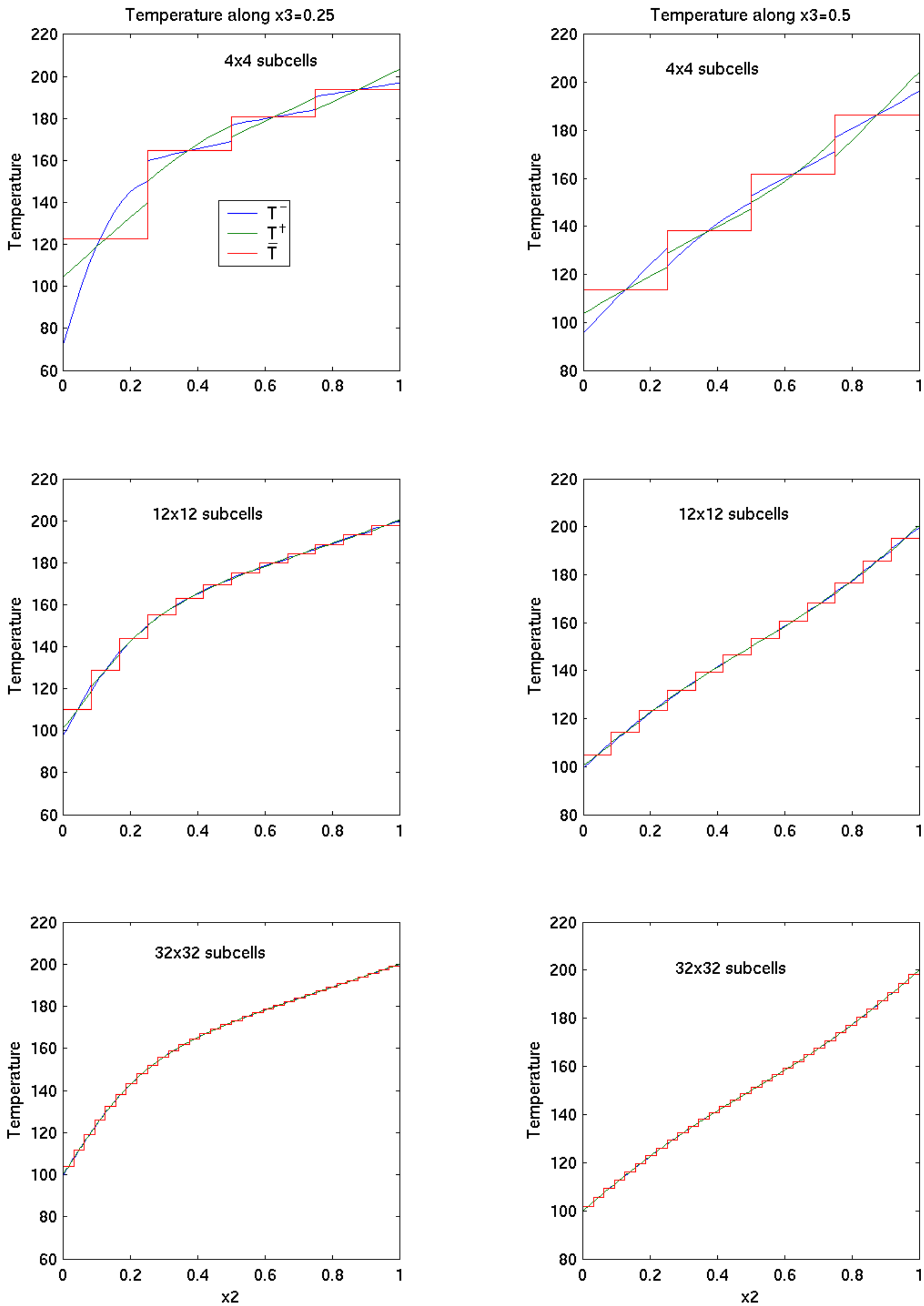

Figure 18. Convergence of the temperature distributions along the cross-sections $x_2 = 0.5, 0.75$.

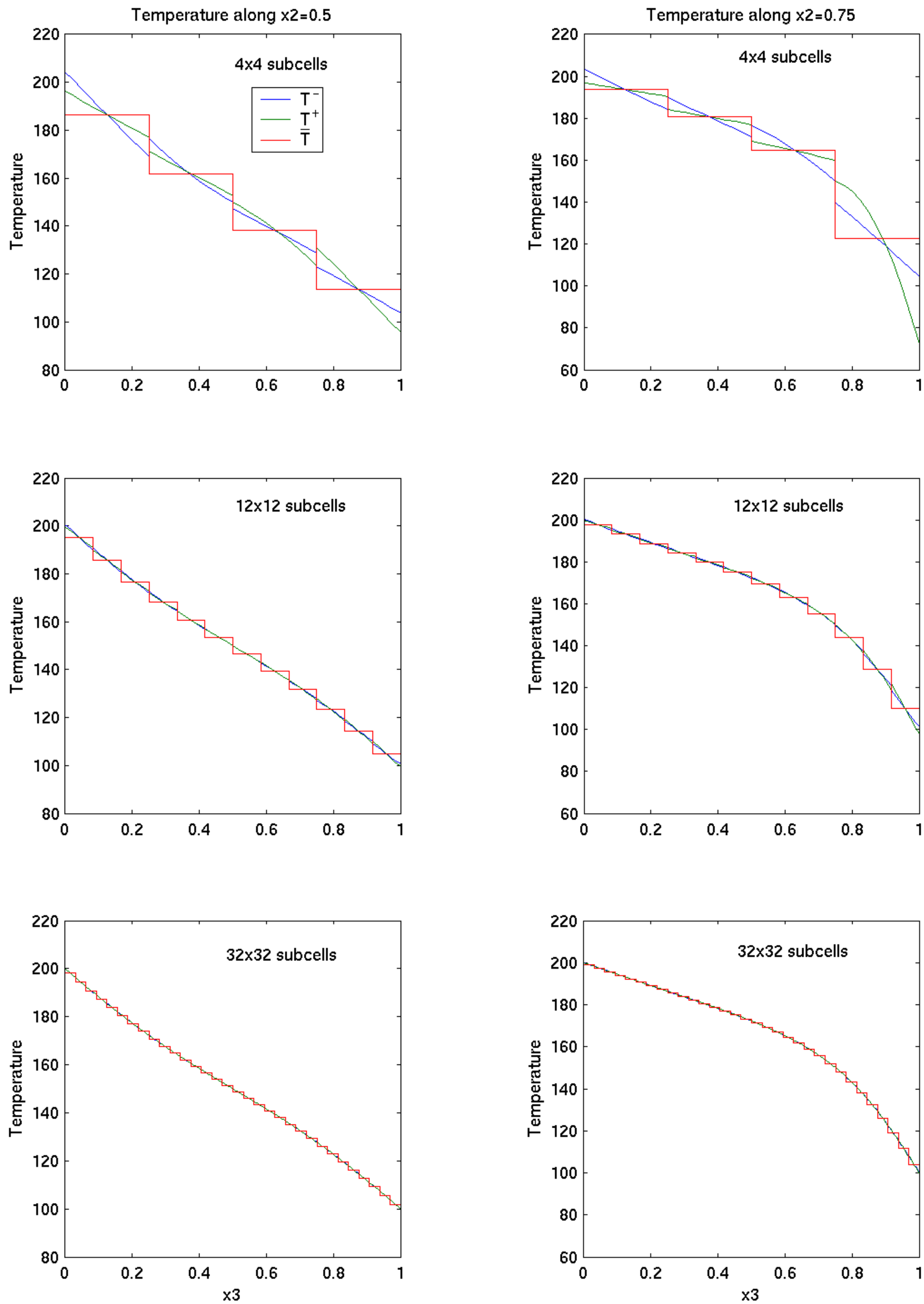

Figure 19. Convergence of the temperature distribution along the cross-sections $x_3 = 0.25, 0.5$.

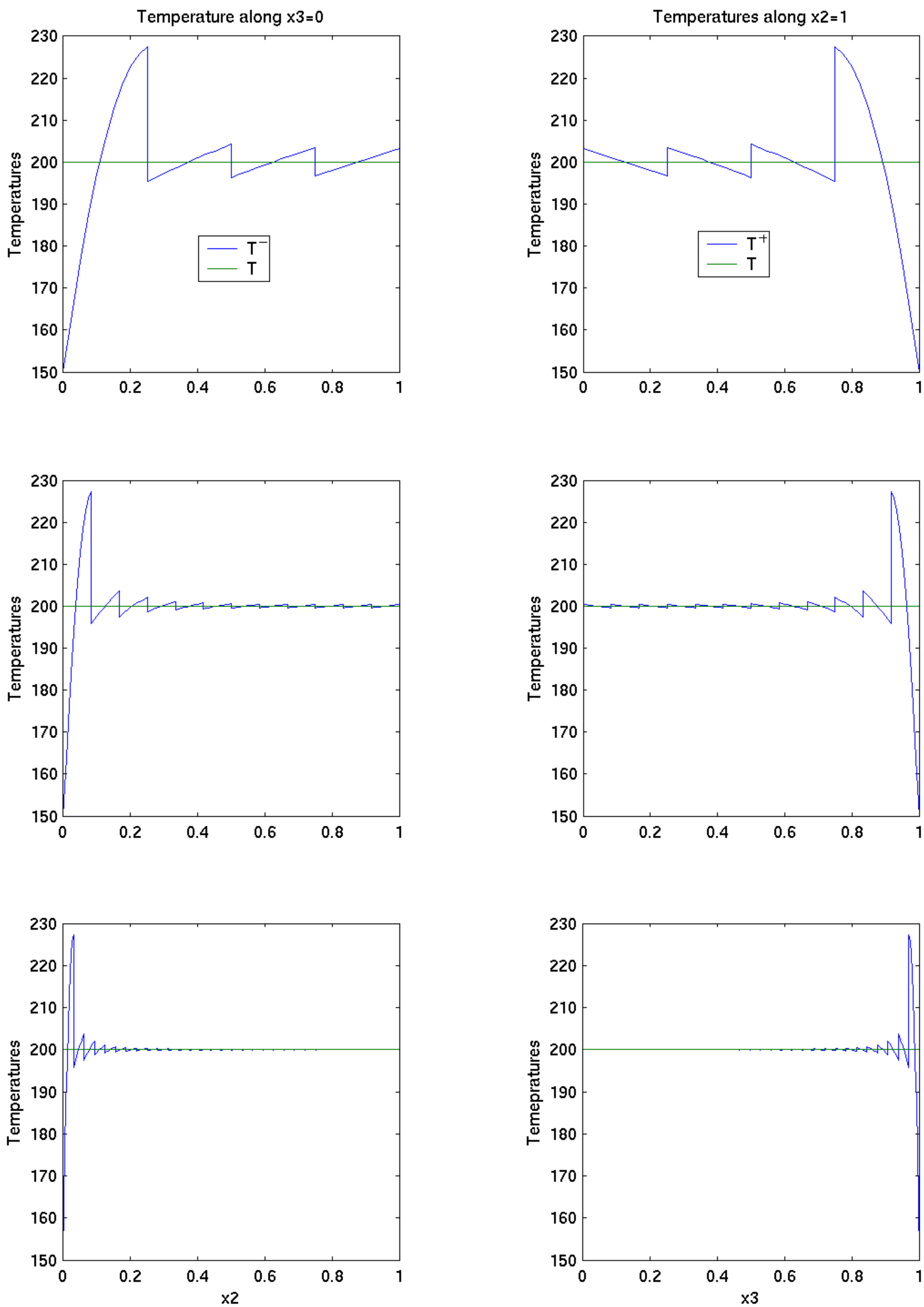

Figure 20. Convergence of the temperature distributions along the edges $x_3 = 0$ and $x_2 = 1$.

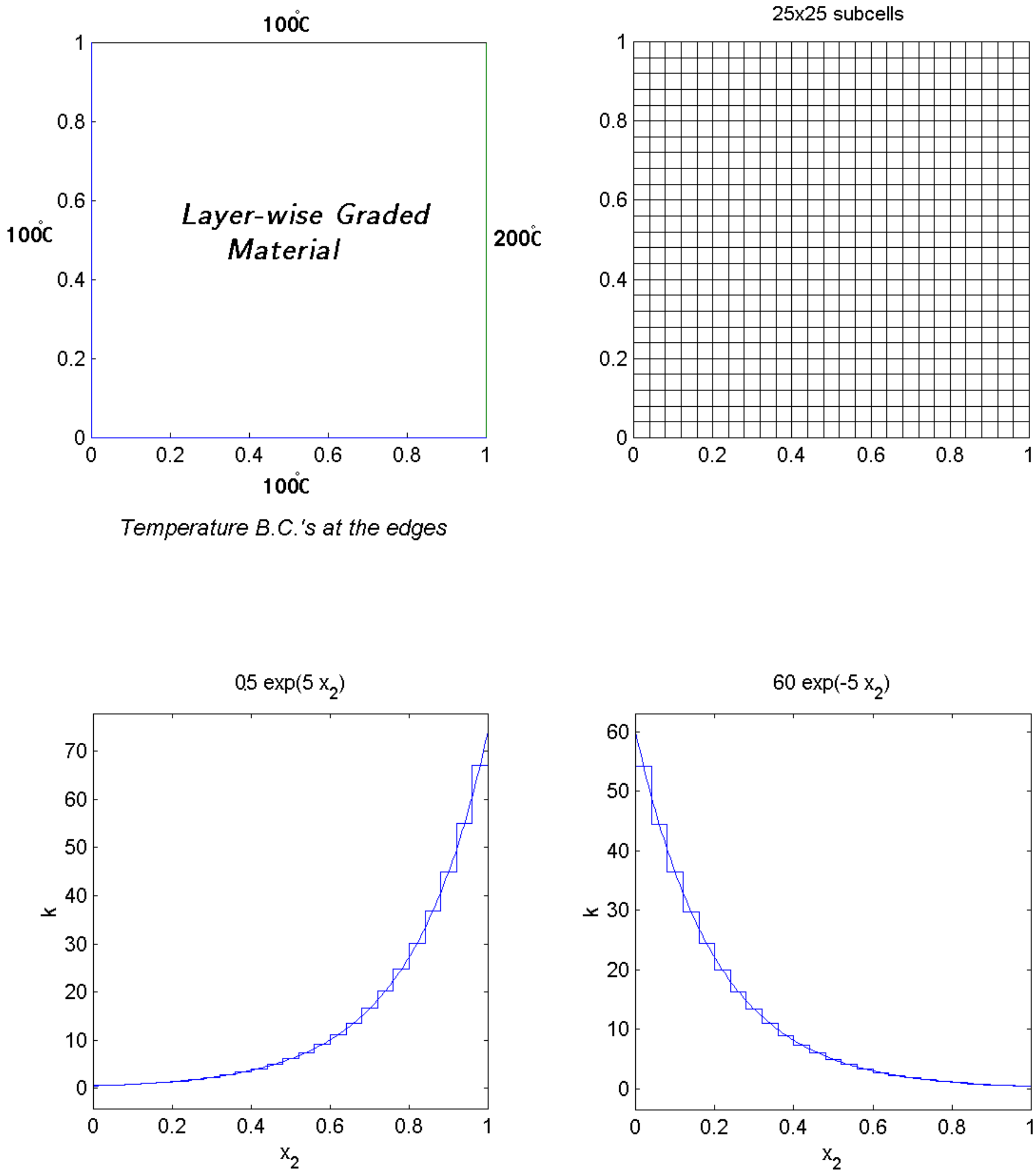

Figure 21. Problem definition and mesh discretization for a layered plate with piece-wise uniformly graded thermal conductivity.

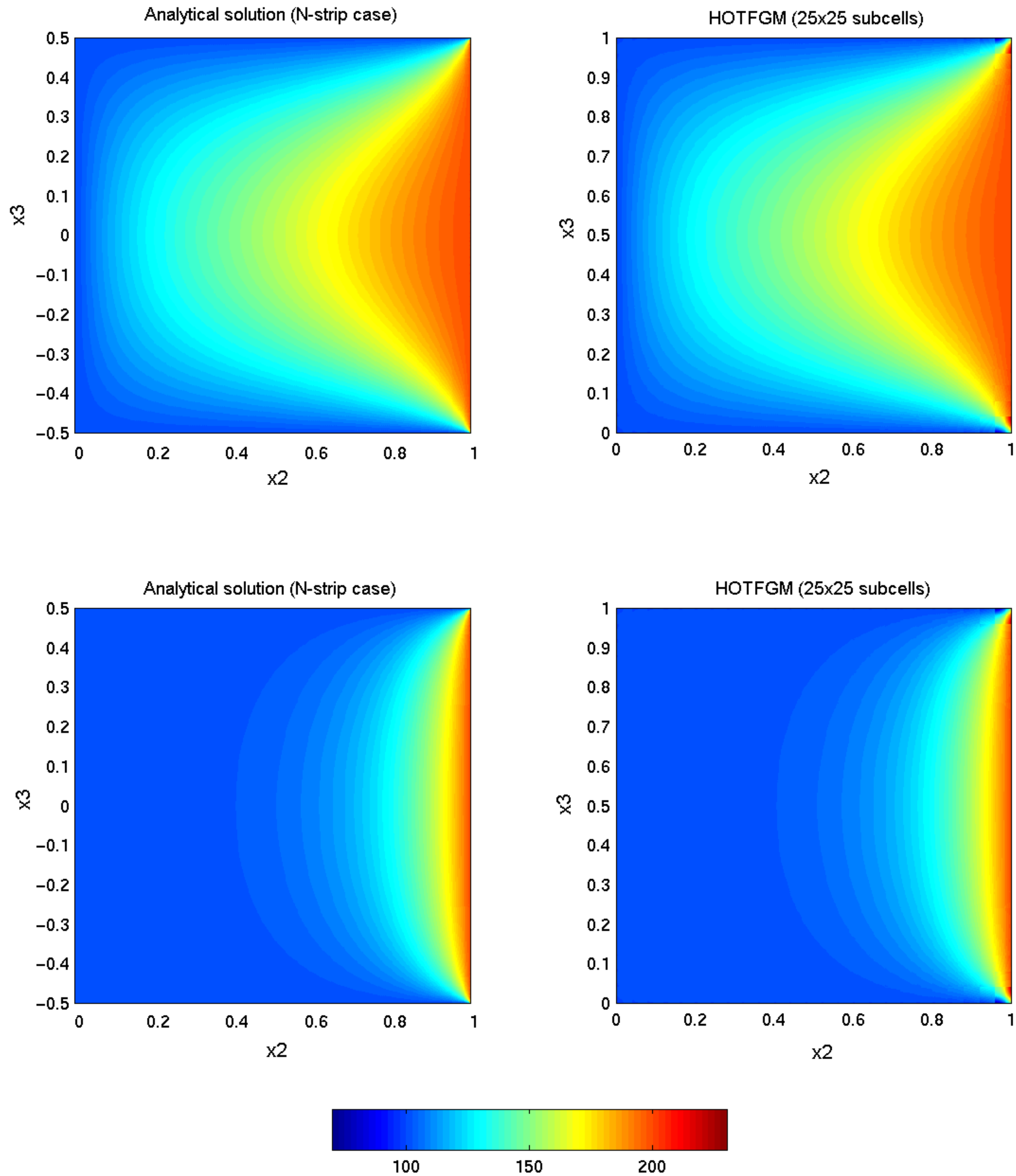

Figure 22. Temperature field comparison between HOTFGM-2D and analytical solutions for the layered plate with exponentially increasing (top) and decreasing (bottom) piece-wise uniformly graded thermal conductivity.

dimensions, shown in the upper right schematic of Figure 21, and assigning the same values of thermal conductivity in each vertical column of subcells as in the case of the analytical solution. The above boundary conditions and manner of grading will produce a temperature field which is symmetric about the horizontal cross section halfway across the plate's height.

The comparison of the full field temperature distributions obtained from the analytical and higher-order theory solutions is given in Figure 22 for the exponentially increasing (top) and decreasing (bottom) thermal conductivity variations. In both cases, excellent agreement is evident throughout almost the entire plate with the exception of isolated regions in the vicinity of the upper and lower right corners. These regions exhibit large temperature gradients caused by the temperature discontinuities at the corners themselves. Local mesh refinement is therefore needed to produce better correlation in these regions in the case of HOTFGM.

As is also observed in Figure 22, when the thermal conductivity increases in the x_2 direction according to the function $k = 0.5e^{5x_2}$, the temperature field is shifted towards the left vertical boundary with respect to the temperature field in the homogeneous plate subjected to the same boundary conditions shown in Figure 13. Alternatively, when the thermal conductivity decreases in the x_2 direction according to the function $k = 60e^{-5x_2}$, the temperature field is shifted towards the right vertical boundary. This can be explained by the Fourier's heat conduction law,

$$q_i^{(\beta\gamma)} = -k_{ij}^{(\beta\gamma)} \partial_j T^{(\beta\gamma)}$$

where the temperature field is seen to be modulated by the spatial variation in thermal conductivity.

5.2 Efficient Reformulation: Variable Thermal Conductivity

In this section, the efficient reformulation of the higher-order theory described in Section 3 is employed to generate the temperature field in a continuously graded plate whose thermal conductivity variations are described by the exponential functions of the preceding section. To mimic the exponentially varying thermal conductivity in the x_2 direction, three volumetric discretizations were employed. In all cases the plate was discretized into 25 subcells along the x_3 direction, while along the x_2 direction the plate was discretized into 10 and 12 uniformly spaced, and 12 nonuniformly spaced subcells, resulting in two uniformly spaced 10×25 and 12×25 microstructures and one nonuniformly spaced 12×25 microstructure. The thermal conductivity $k_2^{(\beta\gamma)}$ in each vertical column of $(\beta\gamma)$ subcells was varied linearly with the local subcell coordinate $\bar{x}_2^{(\beta)}$ such that continuity was preserved from one column of subcells to another along the global x_2 coordinate. The values of the thermal conductivity at the subcell boundaries were calculated using the exponential functions employed in the preceding section, and subsequently employed in the construction of linear approximation of the thermal conductivity $k_2^{(\beta\gamma)}$ in each subcell. Figure 23 illustrates the piecewise linearly varying $k_2^{(\beta\gamma)}$ in the manner that approximates the exponentially increasing thermal conductivity for the three volume discretizations. The thermal conductivity in the x_3 direction, $k_3^{(\beta\gamma)}$, was kept constant in each column of subcells, but varied from one column of subcells to the next by taking the average value of the thermal conductivities at the subcell boundaries calculated from the exponential functions. The general expressions for variable thermal conductivities in the x_2 and x_3 directions, $k_2^{(\beta\gamma)}$ and $k_3^{(\beta\gamma)}$, respectively, thus reduce to the following expressions,

$$\begin{aligned} k_2^{(\beta\gamma)} &= k_{20}^{(\beta\gamma)} + k_{22}^{(\beta\gamma)} \bar{x}_2^{(\beta)} \\ k_3^{(\beta\gamma)} &= k_{30}^{(\beta\gamma)} \end{aligned}$$

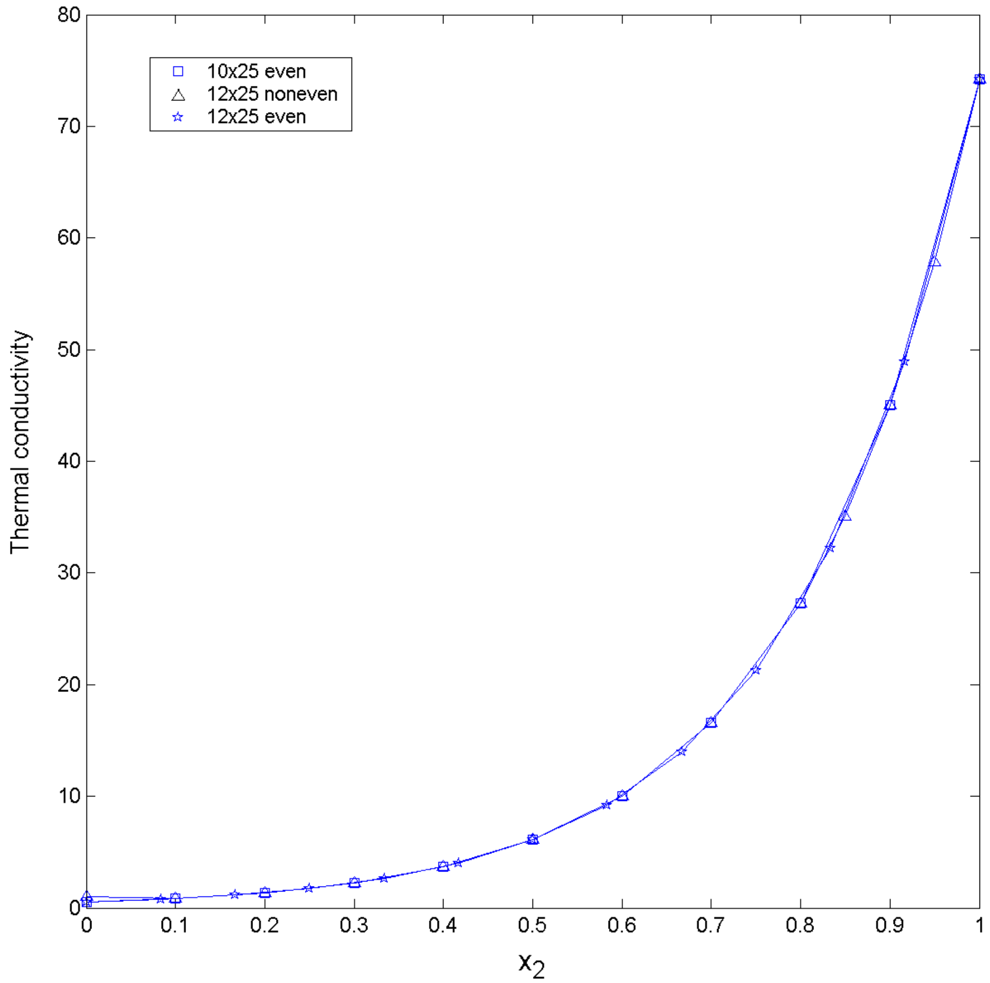

Figure 23. Thermal conductivity approximation by piece-wise linear variation.

The full field temperature distributions obtained for the 10×25 subcell mesh with the exponentially increasing (top) and decreasing (bottom) thermal conductivities, generated using the efficient reformulation with locally linearly varying conductivities, are presented in the right column of Figure 24. The corresponding predictions generated using the user-friendly formulation with 25×25 subcell mesh of the preceding section are included in the left column of Figure 24 for comparison. The agreement is very good everywhere except in the upper and lower right corner regions where the temperature jumps occur. Increasing the mesh size to uniformly spaced 12×25 subcells improves the agreement in these corner regions, as seen in the left column of Figure 25. Retaining the same mesh size but preferentially increasing the number of subcells in the corner regions where large thermal gradients occur produces essentially the same temperature distributions in the entire linearly graded plate as those in the discretely graded plate, as seen in the right column of Figure 25. This indicates that a smaller number of subcells with local linearly varying thermal conductivity is required to capture the essential character of the temperature field in a discretely graded plate with piecewise uniform thermal conductivity.

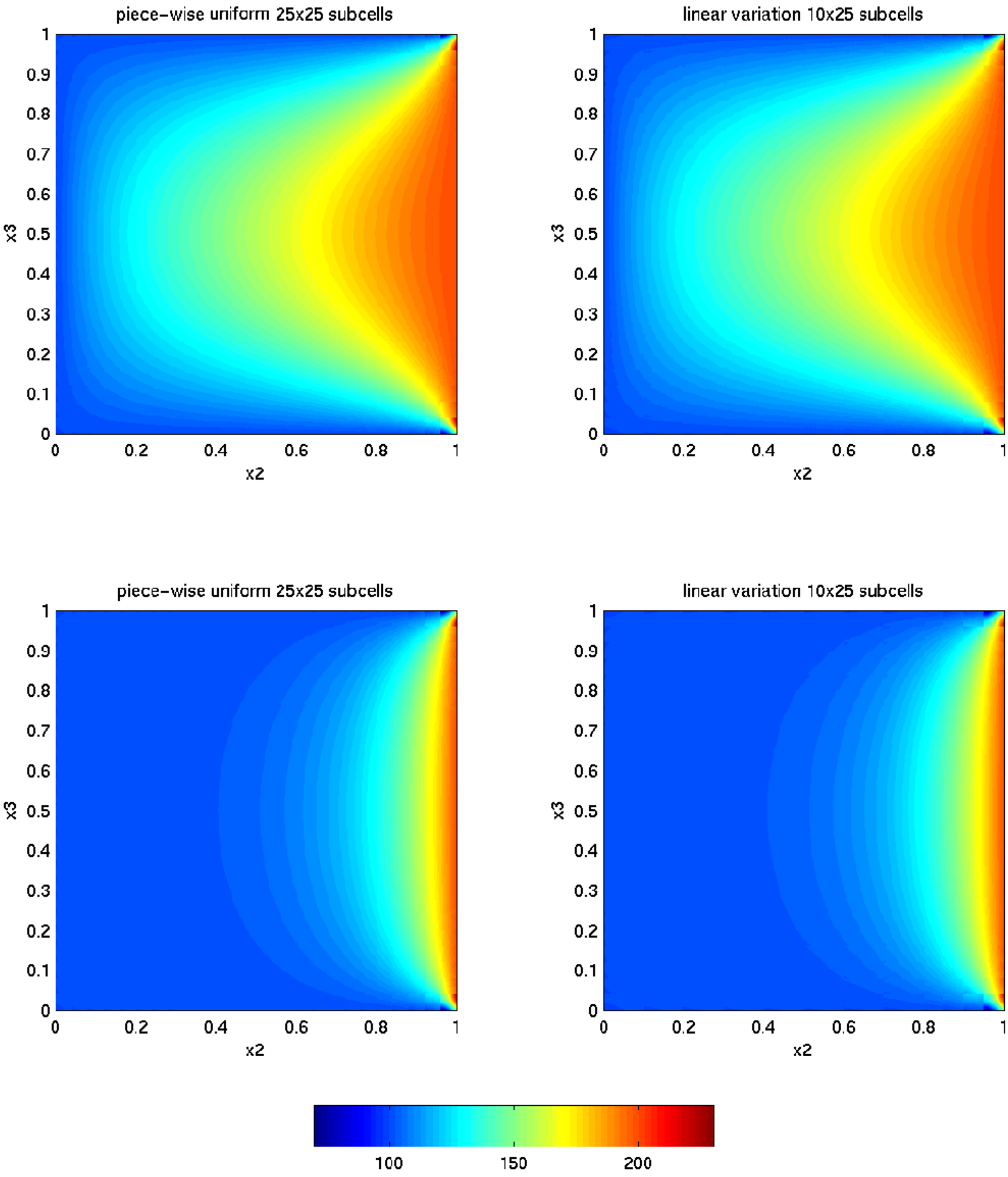

Figure 24. Temperature field comparison between user-friendly formulation and efficient reformulation of HOTFGM-2D.

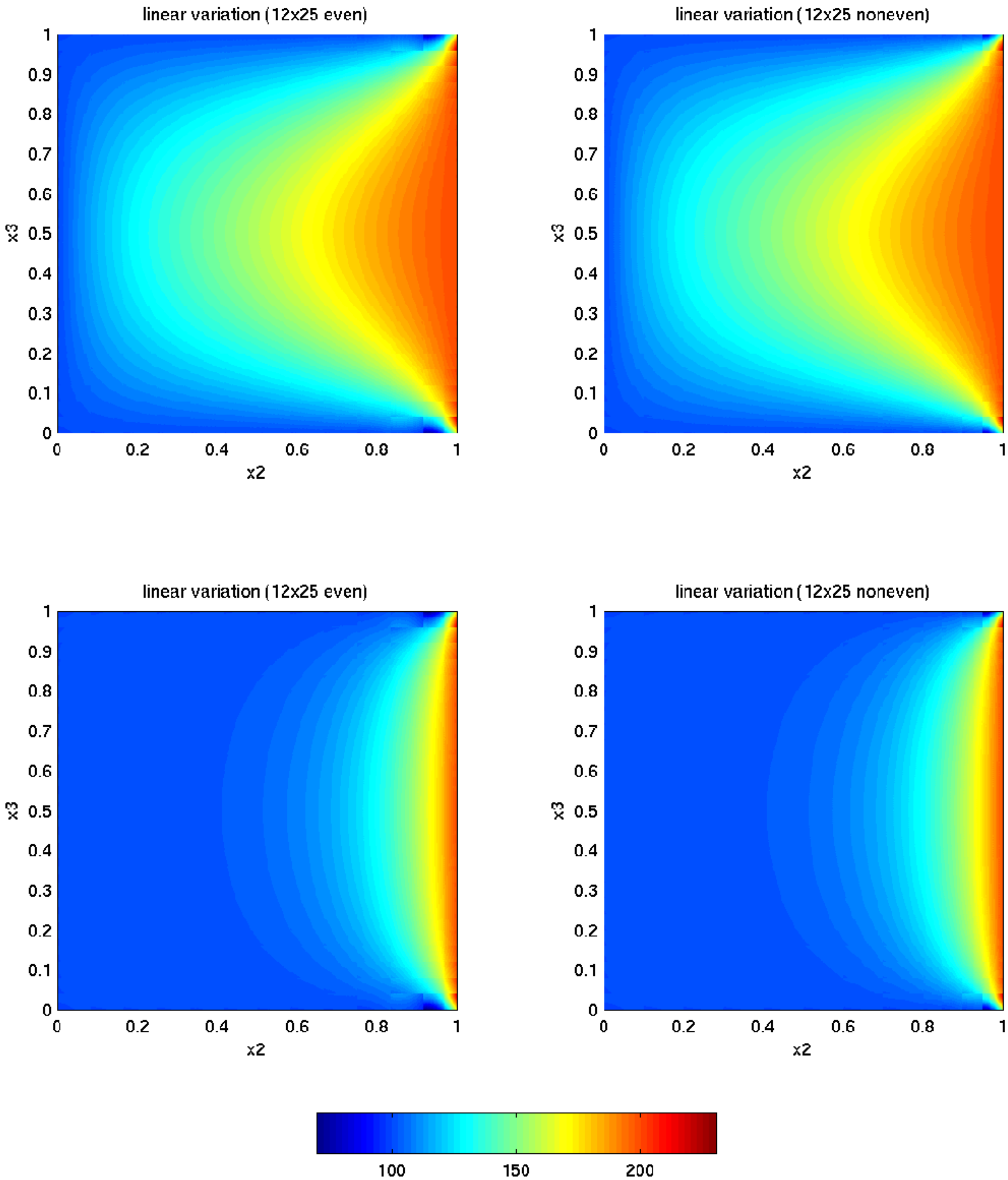

Figure 25. Temperature field comparison between evenly and nonevenly distributed thermal conductivity predicted by the efficient reformulation of HOTFGM-2D with linearly varying thermal conductivity.

5.3 A Thermal Barrier Coating Application

In this section, the temperature field in a graded thermal barrier coating subjected to a through-thickness temperature gradient is investigated using the efficient reformulation of the higher-order theory. The zirconia coating is graded with metallic inclusions such that the volume fraction of the inclusion phase increases with increasing distance from the hot surface of the coating exposed to the temperature of $200°C$, Figure 26. The cold surface where the metallic inclusion content is greatest is exposed to $100°C$. The coating's graded microstructure, which is periodic along the vertical direction, is simulated by the zero heat flux boundary conditions on the top and bottom surfaces of the coating. The thermal conductivities of the zirconia coating and the metallic inclusions were taken to be 0.5 and 100 $W/m -° C$, respectively.

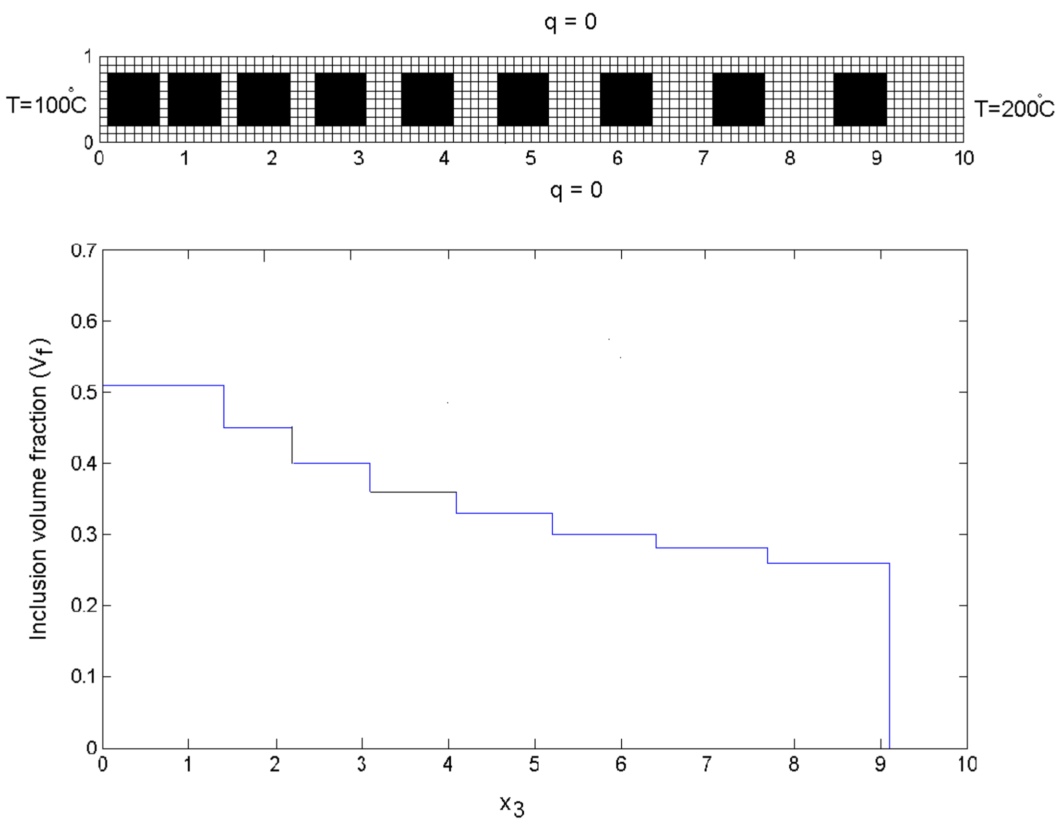

Figure 26. Actual microstructure and volume fraction distribution of the inclusion phase.

The thermal analysis is conducted using the actual graded microstructure seen in Figure 26 which has been discretized into 10×100 subcell mesh, and two additional discretely graded and linearly graded microstructures with local homogenization. The locally homogenized microstructures were obtained from the actual microstructure by first determining the local metallic inclusion content in each of the nine regions into which the actual microstructure was divided in the manner shown in Figure 26. Subsequently, each region with its local inclusion content was modeled using HOTFGM as a strip containing 16 uniformly spaced metallic inclusions subjected to a known macroscopic temperature gradient along its length and zero heat flux on the top and bottom surfaces, Figure 27.

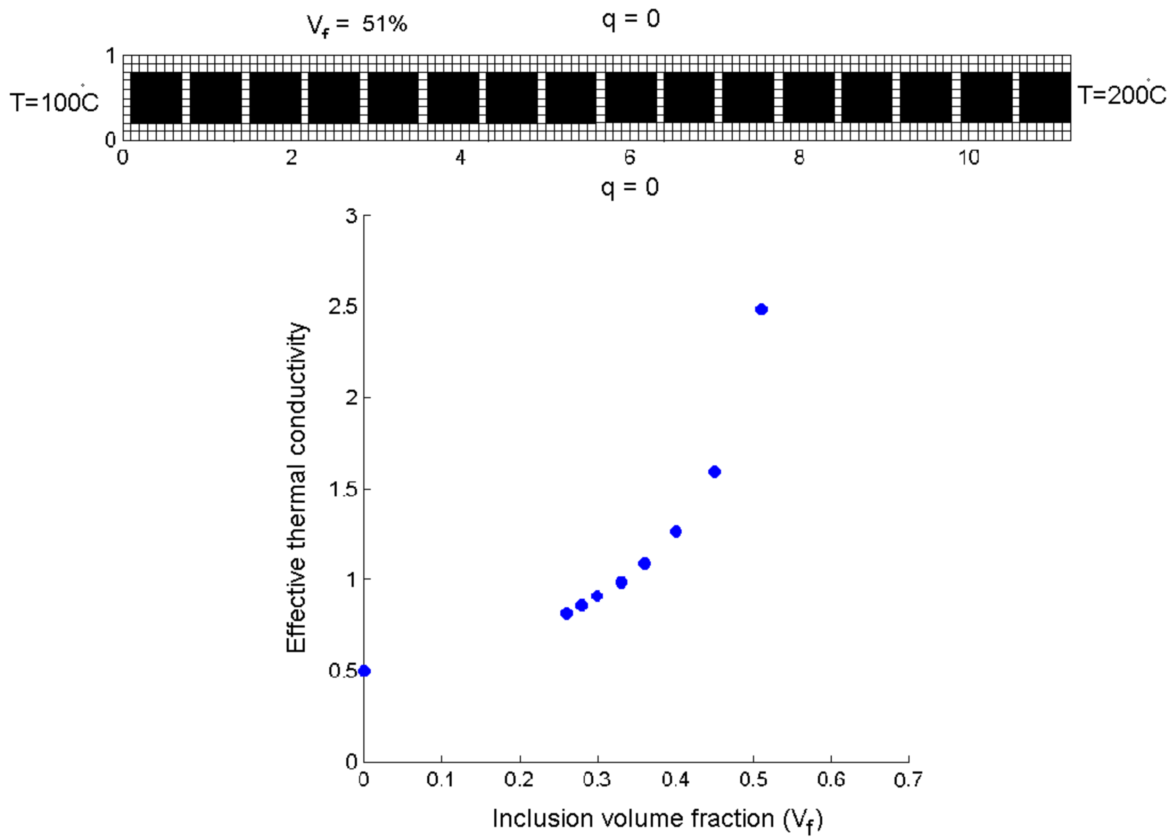

Figure 27. Homogenized thermal conductivity vs fiber volume fraction.

The effective thermal conductivity for such strip was calculated from the ratio of the average heat flux obtained from the solution of the specified boundary-value problem and the negative of the imposed average or macroscopic temperature gradient. The choice of 16 uniformly spaced metallic inclusions was dictated by the asymptotic behavior of the average thermal conductivity as a function of the inclusion number. The results of the calculations are included in Figure 27 in the form of a graph of the macroscopic thermal conductivity as a function of the metallic inclusion volume fraction which corresponds to each of the regions shown in Figure 26. The resulting discretely and linearly graded in a piecewise manner thermal conductivities along the actual coating's length are given in Figure 28. The piecewise linearly graded microstructure was obtained from the piecewise discretely graded microstructure by using the center points of adjacent subcells to define new subcells with linearly varying conductivities. Due to the homogenization of the microstructure and the applied boundary conditions which produce a one-dimensional temperature field, the homogenized microstructures were represented by 1×9 subcell meshes.

The full field temperature distributions in the actual and homogenized graded coatings are given in Figure 29. The temperature distribution in the actual coating is clearly two-dimensional, with the disturbances created by the inclusion presence more pronounced near the upper and lower boundaries than in the interior. In contrast, the temperature fields in the homogenized coatings are clearly one-dimensional, with a slight shift present between the discretely and linearly graded homogenized microstructures. A more quantitative picture of the differences in the temperature distributions among the three microstructures is obtained by comparing the cross section plots. These are presented in the top portion of Figure 30 with three cross section temperature distributions

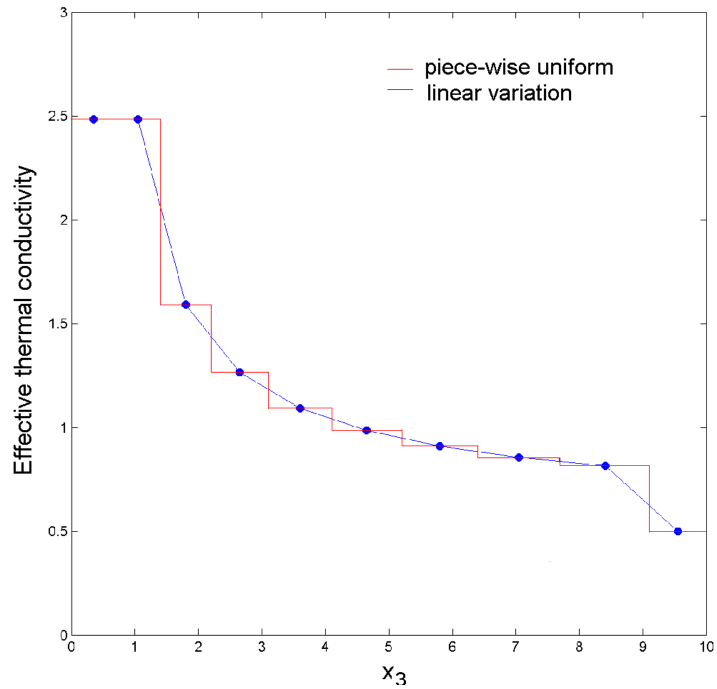

Figure 28. Homogenized thermal conductivity as a function of position.

in the actual coating and one in each of the two homogenized coatings. The staircase temperature pattern observed in the actual coating is due to the pronounced differences in the thermal conductivities of the metallic inclusion and ceramic matrix phases. In contrast, the temperature distributions in the homogenized coatings are smoothly and continuously increasing functions of the coordinate along the coating's length, with the differences between the two distributions visible near the hot surface. The bottom portion of Figure 30 compares the temperature distribution in the actual coating averaged across the coating's width with the distributions in the homogenized coatings. In both cases, the temperature distributions in the actual coating, averaged or unaveraged across the coatings width, are above the temperature distribution in the discretely graded coating. This is not true in the case of the linearly graded coating wherein the temperature distribution is actually higher in some regions near the hot surface than the temperature distribution in the actual coating.

Despite the fact that the temperature distributions in the two homogenized coatings are almost identical with the exception of the region near the hot surface, the average heat flux calculated in the homogenized coating with piecewise linear variation of the thermal conductivity is closer to the average heat flux in the actual coating than the averag flux in the discretely graded coating. These values can be used to calculate the macroscopic thermal conductivity of the coating across its thickness as shown below,

$$\begin{aligned}
\bar{q}_2^{actual} &= -9.787 \Longrightarrow \bar{k}_2^{actual} = \frac{\bar{q}_2^{actual}}{\Delta T/L} = 0.9787 \\
\bar{q}_2^{linear} &= -9.768 \Longrightarrow \bar{k}_2^{linear} = \frac{\bar{q}_2^{linear}}{\Delta T/L} = 0.9768 \\
\bar{q}_2^{discrete} &= -9.841 \Longrightarrow \bar{k}_2^{discrete} = \frac{\bar{q}_2^{discrete}}{\Delta T/L} = 0.9841
\end{aligned}$$

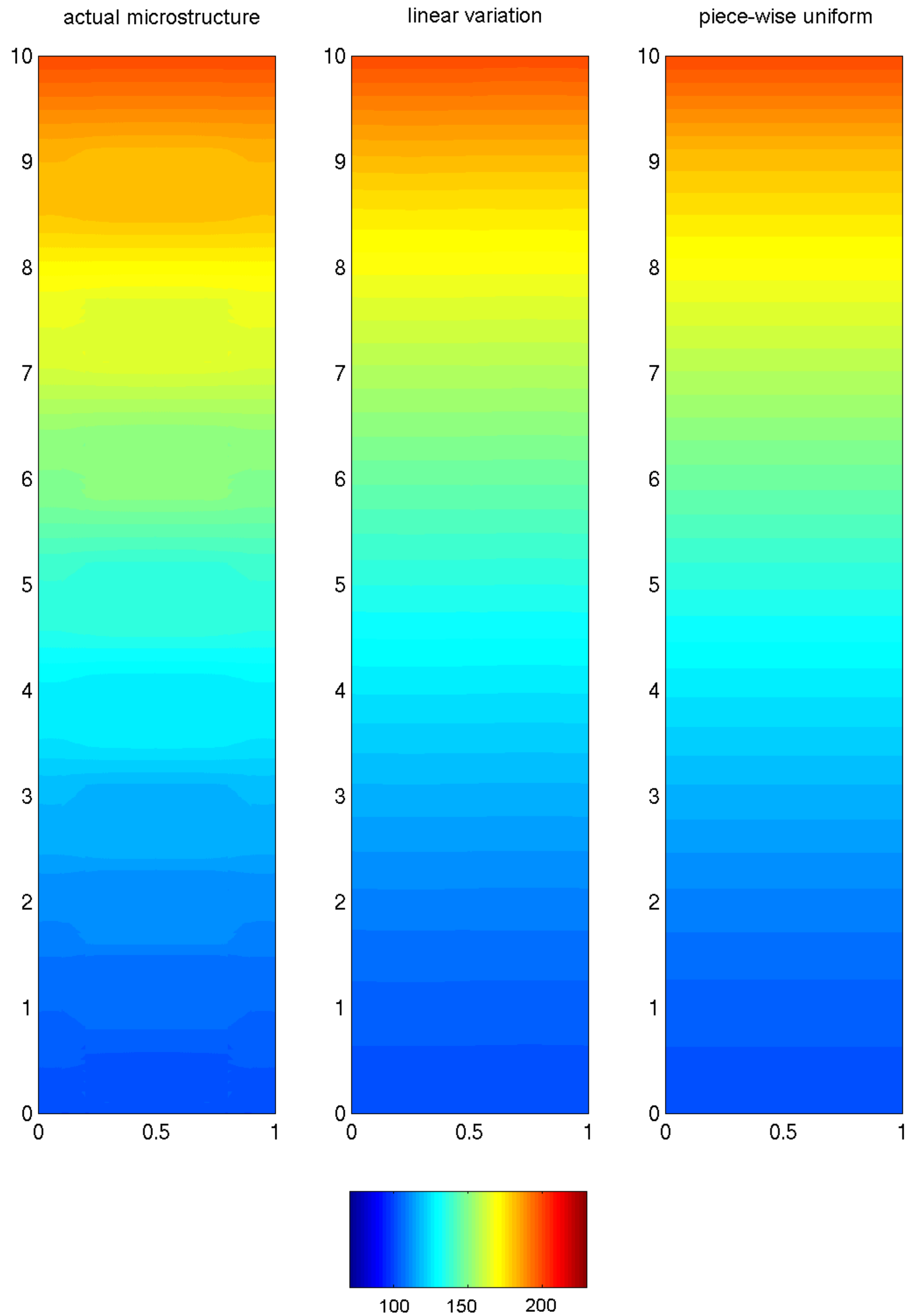

Figure 29. Temperature distributions in TBC with actual and homogenized microstructures.

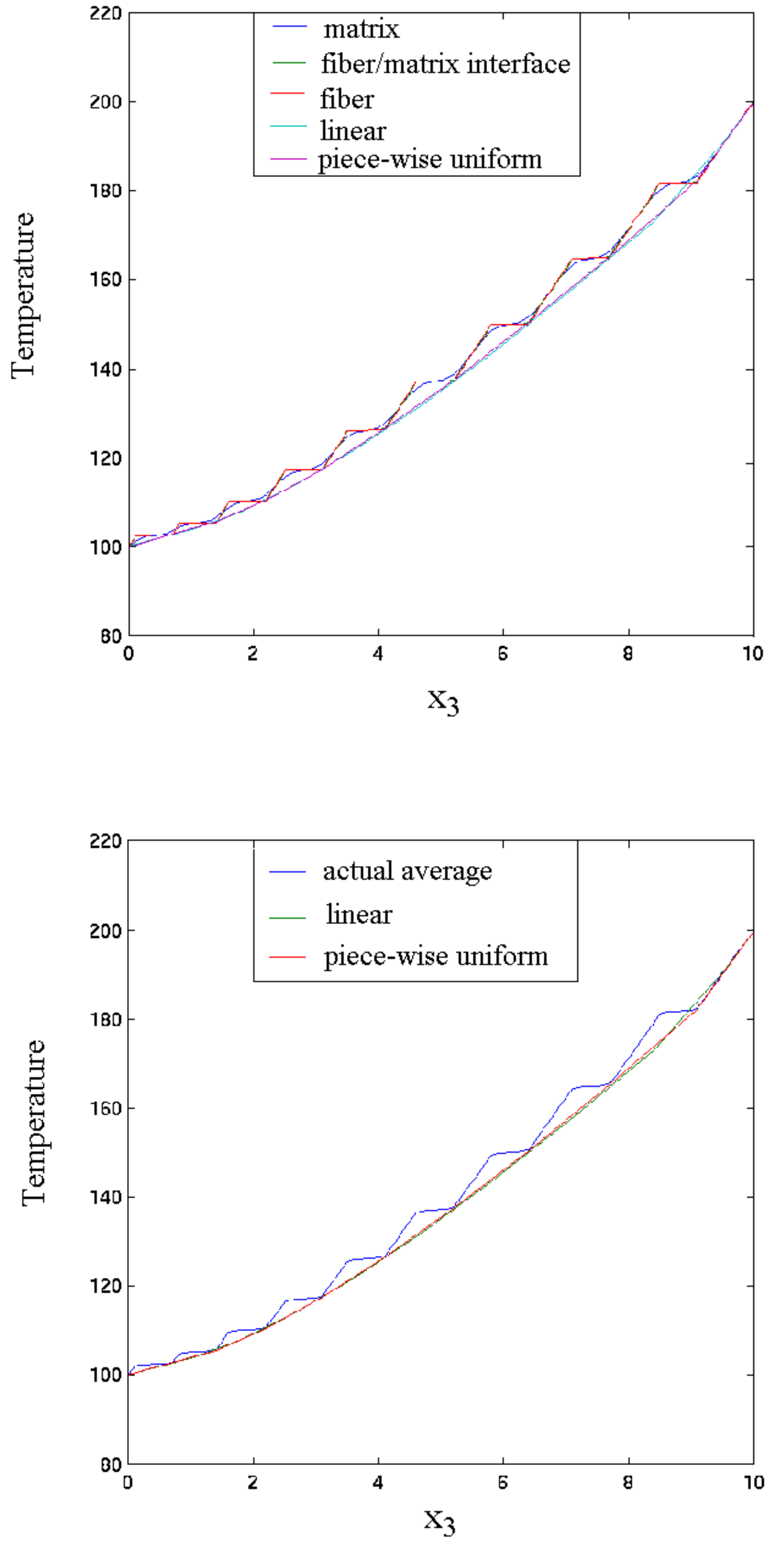

Figure 30. Cross-section temperature distributions comparison.

where $\Delta T = 100°C$ is the temperature difference between the top and bottom surfaces of the coating and $L = 100$ is the coating's thickness. Consequently, the effective thermal conductivity of the entire coating based on the linearly graded microstructure is closer to the effective thermal conductivity of the actual coating than the discretely homogenized coating. Thus it appears that the linear thermal conductivity variation is more appropriate for estimating the effective thermal conductivities of actual graded microstructures than the discrete thermal conductivity variation when the coating's microstructure is relatively coarse.

6 Conclusions and Future Work

The goal of this research was to develop a generic cell-free, subcell-based formulation of the higher-order theory for functionally graded materials developed by Aboudi et al. (1999), which would then provide a basis for a more efficient reformulation using the local/global conductivity matrix approach. In order to extend the higher-order theory's range of applicability, variable thermal conductivity capability at the subcell level was also incorporated into the efficient reformulation. This investigation was undertaken because the original formulation of HOTFGM is computationally intensive. This, in turn, limits the size of problems that can be analyzed due to the large number of equations required to mimic realistic microstructures of functionally graded materials.

In order to validate both the user-friendly formulation and the reformulation of HOTFGM with variable thermal conductivity, analytical solutions to the steady-state heat equation were developed for homogeneous and layered plates. The homogeneous plate solution was used to study the convergence behavior of the user-friendly formulation as a function of mesh discretization. The layered-plate solution was employed to investigate temperature distributions in discretely graded plates. Comparison between the results obtained from the user-friendly formulation and analytical solutions validates the simplified set of equations of the higher-order theory based on the more straightforward volume discretization which does not differentiate between generic cells and subcells. In particular, identical results were obtained for a homogeneous plate subjected to thermal boundary conditions that produced internal temperature fields with different symmetries. The solution's convergence was demonstrated to be quite rapid. A piecewise uniformly graded plate with exponentially varying thermal conductivity was also analyzed and the results obtained from the higher-order theory coincided with the analytical solution for a layered plate.

The user-friendly formulation is easy to understand and implement. More importantly, it provides a basis for the development of an efficient reformulation based on the local/global conductivity matrix approach, which was also successfully accomplished, taking the locally variable thermal conductivity at the subcell level into account. The efficient reformulation has significantly decreased the number of equations. The reduction of the number of equations by as much as 60% for some problems has enhanced the theory's capability, enabling solution of more practical and complicated problems. Comparison of temperature fields in piecewise uniformly graded and linearly graded cases, both of which approximate the same spatially varying thermal conductivity at the global scale, revealed that the same temperature distribution can be obtained with a smaller volume discretization when the thermal conductivity is allowed to vary at the subcell level. Therefore, the efficient reformulation of the higher-order theory with variable thermal conductivity made possible the solution of a wide range of problems requiring large number of subcells. Thus, after transition from the user-friendly formulation to reformulation, the temperature distribution prediction for arbitrary microstructures under many circumstances can be accurately accomplished in a more efficient manner.

However, this research was limited to steady-state heat conduction of graded materials in two dimensions. In order to further extend the theory's range of applicability to practical problems, further research is required. The next step is to extend the presented efficient reformulation to enable the analysis of mechanical problems. As the first step, the two-dimensional elastic reformulation of the higher-order theory with linearly varying material properties within each subcell will be developed and then extended to three dimensions. This will complement the efficient thermomechanical reformulation of the higher-order theory with constant subcell material properties recently completed by Bansal (2002). Further, in order to make full use of material properties and optimize structural design, it is necessary to incorporate viscoelastic, viscoplastic or plastic effects of material response into the theoretical framework. Therefore, viscoelastic, viscoplastic and plastic capabilities should be included in the reformulated higher-order theory. Fracture analysis is also an important area of FGMs. Therefore, the capability to analyze fracture mechanics problems should also be included in the reformulated higher-order theory.

References

[1] Aboudi, J. (1991). Mechanics of Composite Materials: A Unified Micromechanical Approach, Elsevier, Amsterdam.

[2] Aboudi, J., Pindera, M-J., Arnold, S. M. (1993). Thermoelastic Response of Large-Diameter Fiber Metal Matrix Composites to Thermal Gradients. *NASA TM 106344,* NASA-Lewis Research Center, Cleveland, OH.

[3] Aboudi, J., Pindera, M-J., Arnold, S. M. (1994). Elastic Response of Metal Matrix Composites with Tailored Microstructures to Thermal Gradients. *International Journal of Solids Structures*, Vol. 31, No. 10, pp 1393-1428.

[4] Aboudi, J., Pindera, M-J., and Arnold, S. M. (1996). Thermoelastic Theory for the Response of Materials Functionally Graded in Two Directions, *International Journal of Solids and Structures*, Vol. 33, No. 7, pp. 931-966.

[5] Aboudi, J., Pindera, M-J., and Arnold, S. M. (1999). Higher-Order Theory for Functionally Graded Materials, *Composites Part B: Engineering*, Vol. 30, No. 8, pp. 777-832.

[6] Amada, S. (1995). Hierarchical Functionally Graded Structures of Bamboo, Barley, and Corn, *Material Research Society Bulletin*, January 1995, Volume XX, No.1. pp. 35-36.

[7] Bansal, Y. (2002). Efficient Reformulation of the Higher-Order Theory for Functionally Graded Materials, *M. S. Thesis, School of Engineering and Applied Science, University of Virginia,* Charlottesville, Virginia.

[8] Davison, T., Wadley, H. N. G, and Pindera, M-J. (1994). Elastic Bahavior of a Layered Cylinder Subjected to Diametral Loading, *Composites Engineering,* Vol. 4, No. 10, pp. 995-1009.

[9] Delfosse, D., Cherradi, N., and IIschner, B. (1997). Numerical and Experimental Determination of Residual Stresses in Graded Materials, *Composites Part B: Engineering*, Vol. 28, No. 1-2, pp. 127-141.

[10] Drake, J. T., Williamson, R. L., and Rabin, B. H. (1993). Finite Element Analysis of Thermal Residual Stresses at Graded Ceramic-Metal Interfaces, *Journal of Applied Physics*, Vol. 74, No. 2, pp. 1321-1326.

[11] Delale, F. and Erdogan, F. (1983). The Crack Problem for a Non-Homogeneous Plane, *Journal of Applied Mechanics*, Vol. 50, pp. 609-614.

[12] Dollmeier, K., Thiele, W., and IIschner, B. (1995), Pilot Study Related to Continuous Fabrication of FGM Strip by P/M, in *FGM 94, Proceedings of the Third International Symposium on Structural and Functionally Graded Materials*, IIschner, B. and Cherradi, N. (Eds.), pp. 27-32, Presses Polytecniques et Universitares Romandes.

[13] Erdogan, F. (1985). The Crack Problem for Bonded Non-Homogeneous Materials under Anti-Plane Shear Loading, *Journal of Applied Mechanics*, Vol. 52, pp. 823-828.

[14] Erdogan, F., Kaya, A. C., and Joseph, P. F. (1991). The Crack Problem in Bonded Non-Homogeneous Materials, *Journal of Applied Mechanics*, Vol. 58, No. 2, pp. 410-418.

[15] Erdogan, F. (1995). Fracture Mechanics of Functionally Graded Materials, *Composites Engineering*, Vol. 5, No. 7, pp. 753-770.

[16] Erdogan, F. and Wu, B. H. (1996). Crack Problems in FGM Layers under Thermal Stresses, *Journal of Thermal Stresses*, Vol. 19, No. 3, pp. 237-265.

[17] Fukumoto, M., Yamasaki, T. and Okane, I. (1994). Influence of Coating Configuration on Cyclic Thermal Shock Fracture Behaviour of Plasma Sprayed Coatings, in *FGM 94, Proceedings of the Third International Symposium on Structural and Functionally Graded Materials,* IIschner, B. and Cherradi, N. (Eds.), pp. 425-429, Presses Polytecniques et Universitares Romandes.

[18] Horgan, C. O. and Chan, A. M. (1999). The Pressurized Hollow Cylinder or Disk Problem for Functionally Graded Isotropic Linearly Elastic Materials, *Journal of Elasticity*, Vol. 55, No. 1, pp. 43-59.

[19] Ichikawa K. (Ed.), (2001). Functionally Graded Materials in the 21^{st} Century (A Workshop on Trends and Forecasts), Kluwer Academic Publishers.

[20] Ilschner, B. and Cherradi, N., (1994). Proceedings of the 3^{rd} International Symposium on Structural and Functional Gradient Materials*, Presses polytechniques et Universitaires Romandes.*

[21] Ilschner, B. (1997). Lessons Learnt in 7 years of FGM Research at Lausanne in *FGM 96, Proceedings of the Fourth International Symposium on Functionally Graded Materials,* Shiota, I. and Miyamoto, Y. (Eds.), pp. 15-20, Amsterdam, Elsevier.

[22] Jian, C. Y., Hashida, T., Takahashi, H., and Saito, M. (1995). Thermal Shock and Fatigue Resistance Evaluation of Functionally Graded Coating for Gas Turbine Blades by Laser Heating Method, *Composites Engineering*, Vol. 5, No. 7, pp. 879-889.

[23] Jin, Z. H. and Paulino, G. H. (2001). Transient Thermal Stress Analysis of an Edge Crack in a Functionally Graded Material, *International Journal of Fracture*, Vol. 107, No. 1, pp. 73-98.

[24] Kaysser, W. A. and IIschner, B. (1995). FGM Research Activities in Europe, *Material Research Society Bulletin*, January 1995, Volume XX, No.1. pp. 22-26.

[25] Kawasaki, A. and Watanabe, R. (1997). Effect of Gradient Microstructure on Thermal Shock Crack Extension in Metal/Ceramic Functionally Graded Materials, in *FGM 96, Proceedings of the Fourth International Symposium on Functionally Graded Materials*, Shiota, I and Miyamoto, Y. (Eds.), pp. 143-154, Amsterdam, Elsevier.

[26] Kokini, K. and Choules, B. B. (1995). Surface Thermal Fracture of Functionally Graded Ceramic Coatings-Effect of Architecture and Materials, *Composites Engineering*, Vol. 5, No. 7, pp. 865-877.

[27] Kokini, K., Takeuchi, Y. R., and Choules, B. B. (1996). Surface Thermal Cracking of Thermal Barrier Coating Owing to Stress Relaxation: Zirconia vs Mullite, *Surface Coating Technology*, Vol. 82, pp. 72-82.

[28] Lee, Y-D. and Erdogan, F. (1998). Interface Cracking of FGM Coatings Under Steady-State Heat Flow, *Engineering Fracture Mechanics*, Vol. 59, No. 3, pp. 361-380.

[29] Needleman, A. and Suresh S. (1996). Mechanics and Physics of Layered and Graded Materials, *Journal of the Mechanics and Physics of Solids*, Vol. 44, No. 5, pp. 647-821.

[30] Nomura, S. and Sheahen D.M. (1997). Micromehanical Approach to the Thermomechanical Analysis of FGMs, in *FM 96, Proceedings of the Fourth International Symposium on Functionally Graded Materials,* Shiota, I and Miyamoto, Y. (Eds.), pp. 137-141, Amsterdam, Elsevier.

[31] Noda, N. (1999). Thermal Stresses in Functionally Graded Materials, *Journal of Thermal Stresses*, Vol. 24, No. 4-5, pp. 477-512.

[32] Paley, M. and Aboudi. J. (1992). Micromechanical Analysis of Composites by the Generalized Cells Model. *Mechanics of Materials*, Vol. 14, pp. 39-127.

[33] Pindera, M-J. (1991). Local/Global Stiffness Matrix Formulation for Composite Materials and Structures, *Composites Engineering*, Vol. 1, No. 2, pp. 69-83.

[34] Pindera, M-J. and Lane, M. S. (1993). Frictionless Contact of Layered Half Planes, Part I: Analysis, *Journal of Applied Mechanics*, Vol. 30, No. 3, pp. 633-639.

[35] Pindera, M-J., Freed, A. D., and Arnold, S. M. (1993). Effects of Fiber and Interfacial Layer Morphologies on the Thermoplastic Response of Metal Matrix Composites, *International Journal of Solids and Structures*, Vol. 30, No. 9, pp. 1213-1238.

[36] Pindera, M-J., Arnold, S. M., Aboudi, J., and Hui, D. (Eds.), (1994a). Use of Composites in Functionally Graded Materials, *Composites Engineering*, Vol. 4, No. 1. pp. 1-145.

[37] Pindera, M-J., Williams, T. O. and Arnold, S. M. (1994b). Thermoplastic Response of Metal-matrix Composites with Homogenized and Functionally Graded Interfaces, *Composites Engineering,* Vol. 4, No.1, pp 129-145.

[38] Pindera, M-J., Aboudi, J., Arnold, S. M., and Jones, W. F. (Eds.), (1995a). Use of Composites in Muti-Phased and Functionally Graded Materials, *Composites Engineering*, Vol. 5, No. 7. pp. 743-974.

[39] Pindera, M-J., Aboudi, J., and Arnold, S. M. (1995b). Limitations of the Uncoupled, RVE-based Micromechanical Approach in the Analysis of Functionally Graded Composites, *Mechanics of Materials*, Vol. 20, No. 1, pp. 77-94.

[40] Pindera, M-J., Aboudi, J., and Arnold, S. M. (1995c). Recent Advances in the Mechanics of Functionally Graded Composites, in *Aerospace Thermal Structures and Materials for a New Era*, *Progress in Astronautics and Aeronautics*, 168 . Washington, DC, Thornton, E. A. (Ed.), American Institute of Aeronautics and Astronautics Inc. pp. 181-203.

[41] Pindera, M-J., Aboudi, J., Glaeser, A. M., and Arnold, S. M. (Eds.), (1997). Use of Composites in Muti-Phased and Functionally Graded Materials, *Composites Engineering*, Vol. 28, No. 1/2, pp. 1-175.

[42] Pindera, M.-J. and Dunn, P. (1997). Evaluation of the Higher-Order Theory for Functionally Graded Materials via the Finite Element Method, *Composites: Part B: Engineering,* Vol 28, No. 1/2, pp. 109-119.

[43] Pindera, M-J., Aboudi, J., and Arnold, S. M. (1998). Higher-Order Theory for the Analysis of Functionally Graded Materials, in *Advanced Multilayered and Fiber-Reinforced Composites,* Haddad, Y. M. (Ed.), pp. 111-132, Kluwer Academic Publishers, The Netherlands.

[44] Pindera, M-J. and Aboudi, J. (2000). HOTFGM-2D: A Coupled Higher-Order Theory for Cylindrical Structural Components with Bi-Directionally Graded Microstructures, *NASA Contractor Report 2000-210350*, NASA-Glenn Research Center, Cleveland, OH.

[45] Salzar, R. S. and Barton, F. W. (1994). Residual Stress Optimization in Metal-Matrix Composites using Discretely Graded Interfaces, *Composites Engineering*, Vol. 4, No. 1, pp. 115–128.

[46] Salzar, R. S., Pindera, M-J., and Barton, F. W. (1996). Elastic/Plastic Analysis of Layered Metal Matrix Composite Cylinders. Part I: Theory, *Journal of Pressure Vessel Technology,* Vol. 118, No. 1, pp. 13-20.

[47] Shiota, I. and Miyamoto, Y., (1997). Proceedings of the 4^{th} International Symposium on Functionally Graded Materials, *Functionally Graded Materials 1996*, Elsevier.

[48] Suresh, S., Giannakopoulos, A. E., and Olsson, M. (1994). Elastoplastic Analysis of Thermal Cycling-Layered Materials with Sharp Interfaces, *Journal of the Mechanics and Physics of Solids*, Vol. 42, No. 6, pp. 979-1018.

[49] Suresh, S. and Mortensen A., (1998). Fundamentals of Functionally Graded Materials, *2^{nd} edition*, Cambridge University Press.

[50] Sutradhar, A., Paulino, G. H., and Gray, L. J. (2002). Transient Heat Conduction in Homogeneous and Non-Homogeneous Materials by the Laplace Transform Galerkin Boundary Element Method, *Engineering Analysis with Boundary Elements*, Vol. 26, No. 2, pp. 119-132.

[51] Urquhart, E. E. and Pindera, M-J. (1994). Incipient Separation Between a Frictionless Flat Punch and an Anisotropic Multilayered Half Plane, *International Journal of Solids and Structures*, Vol. 31, No. 18, pp 2445-2461.

[52] Williamson, R. L., Rabin, B. H., and Drake, J. T. (1993). Finite Element Analysis of Thermal Residual Stresses at Graded Ceramic-Metal Interfaces. Part 1. Model Description and Geometrical Effects, *Journal of Applied Physics*, Vol. 74, No. 2, pp. 1310-1320.

[53] Williams, T. O. and Pindera, M-J. (1997). An Analytical Model for the Inelastic Axial Shear Response of Unidirectional Metal Matrix Composites, *International Journal of Plasticity*, Vol. 13, No. 3, pp. 261-289.

[54] Yamanouchi, M., Koizumi, M., Hirai, T. and Shiota, I. (Eds.), (1990). *FGM 90, Proceedings of the First International Symposium on Functionally Graded Materials,* October 8-9, 1990, Sendai, Japan.

REPORT DOCUMENTATION PAGE

Form Approved
OMB No. 0704-0188

1. AGENCY USE ONLY (*Leave blank*)	2. REPORT DATE	3. REPORT TYPE AND DATES COVERED
	November 2002	Final Contractor Report

4. TITLE AND SUBTITLE

Efficient Reformulation of HOTFGM: Heat Conduction With Variable Thermal Conductivity

5. FUNDING NUMBERS

WU–708–73–35–00
NAG3–2524

6. AUTHOR(S)

Yi Zhong and Marek-Jerzy Pindera

7. PERFORMING ORGANIZATION NAME(S) AND ADDRESS(ES)

University of Virginia
0 Mccormick Road
Charlottesville, Virginia 22904–2000

8. PERFORMING ORGANIZATION REPORT NUMBER

E–13600

9. SPONSORING/MONITORING AGENCY NAME(S) AND ADDRESS(ES)

National Aeronautics and Space Administration
Washington, DC 20546–0001

10. SPONSORING/MONITORING AGENCY REPORT NUMBER

NASA CR—2002-211910

11. SUPPLEMENTARY NOTES

Project Manager, Steven M. Arnold, Structures and Acoustics Division, NASA Glenn Research Center, organization code 5920, 216–433–3334.

12a. DISTRIBUTION/AVAILABILITY STATEMENT

Unclassified - Unlimited
Subject Categories: 24 and 39 Distribution: Nonstandard

Available electronically at http://gltrs.grc.nasa.gov

This publication is available from the NASA Center for AeroSpace Information, 301–621–0390.

12b. DISTRIBUTION CODE

13. ABSTRACT ***(Maximum 200 words)***

Functionally graded materials (FGMs) have become one of the major research topics in the mechanics of materials community during the past fifteen years. FGMs are heterogeneous materials, characterized by spatially variable microstructures, and thus spatially variable macroscopic properties, introduced to enhance material or structural performance. The spatially variable material properties make FGMs challenging to analyze. Two distinct and fundamentally different computational strategies, called uncoupled macromechanical and coupled micro-macromechanical approaches by some investigators, have been pursued. The uncoupled macromechanical approaches ignore the effect of microstructural gradation by employing specific spatial variations of material properties, which are either assumed or obtained by local homogenization, thereby resulting in erroneous results under certain circumstances. In contrast, the coupled approaches explicitly account for the micro-macrostructural interaction, albeit at a significantly higher computational cost. The higher-order theory for functionally graded materials (HOTFGM) is representative of the coupled approach. However, despite its demonstrated utility in applications where micro-macrostructural coupling effects are important, the theory's full potential is yet to be realized because the original formulation of HOTFGM is computationally intensive. This, in turn, limits the size of problems that can be solved due to the large number of equations required to mimic realistic material microstructures. Therefore, a basis for an efficient reformulation of HOTFGM, referred to as user-friendly formulation, is developed herein, and subsequently employed in the construction of the efficient reformulation using the local/global conductivity matrix approach.

14. SUBJECT TERMS

Micromechanics; Elastic; Thermal; Deformation; Composites; Analysis

15. NUMBER OF PAGES

80

16. PRICE CODE

17. SECURITY CLASSIFICATION OF REPORT	18. SECURITY CLASSIFICATION OF THIS PAGE	19. SECURITY CLASSIFICATION OF ABSTRACT	20. LIMITATION OF ABSTRACT
Unclassified	Unclassified	Unclassified	